Identifying the variety of jovian X-ray auroral structures: tying the morphology of X-ray emissions to associated magnetospheric dynamics

Dale Michael Weigt[1], Caitriona M Jackman[2], Diego Moral Pombo[3], Sarah V Badman[4], Corentin Kenelm Louis[1], William Dunn[5], Seán Christopher McEntee[2], Graziella Branduardi-Raymont[5], Denis Grodent[6], Marissa F. Vogt[7], Chihiro Tao[8], Randy Gladstone[9], Ralph P. Kraft[10], William S Kurth[11], and John E. P. Connerney[12]

[1]Dublin Institute for Advanced Studies (DIAS)
[2]Dublin Institute for Advanced Studies
[3]University of Lancaster
[4]Lancaster University
[5]University College London
[6]Université de Liège
[7]Boston University
[8]National Institute of Information and Communications Technology (NICT)
[9]Southwest Research Institute
[10]Smithsonian Astrophysical Observatory (SI)
[11]University of Iowa
[12]NASA Goddard Space Flight Center

May 2, 2023

Abstract

We define the spatial clustering of X-rays within Jupiter's northern auroral regions by classifying their distributions into 'X-ray auroral structures'. Using data from Chandra during Juno's main mission observations (24 May 2016 – 8 September 2019), we define five X-ray structures based on their ionospheric location and calculate the distribution of auroral photons. The morphology and ionospheric location of these structures allow us to explore the possibility of numerous X-ray auroral magnetospheric drivers. We compare these distributions to Hubble Space Telescope (HST)and Juno (Waves and MAG) data, and a 1D solar wind propagation model to infer the state of Jupiter's magnetosphere. Our results suggest that the five sub-classes of 'X-ray structures' fall under two broad morphologies: fully polar and low latitude emissions. Visibility modelling of each structure suggests the non-uniformity of the photon distributions across the Chandra intervals are likely associated with the switching on/off of magnetospheric drivers as opposed to geometrical effects. The combination of ultraviolet (UV) and X-ray morphological structures is a powerful tool to elucidate the behaviour of both electrons and ions and their link to solar wind/magnetospheric conditions in the absence of an upstream solar monitor.

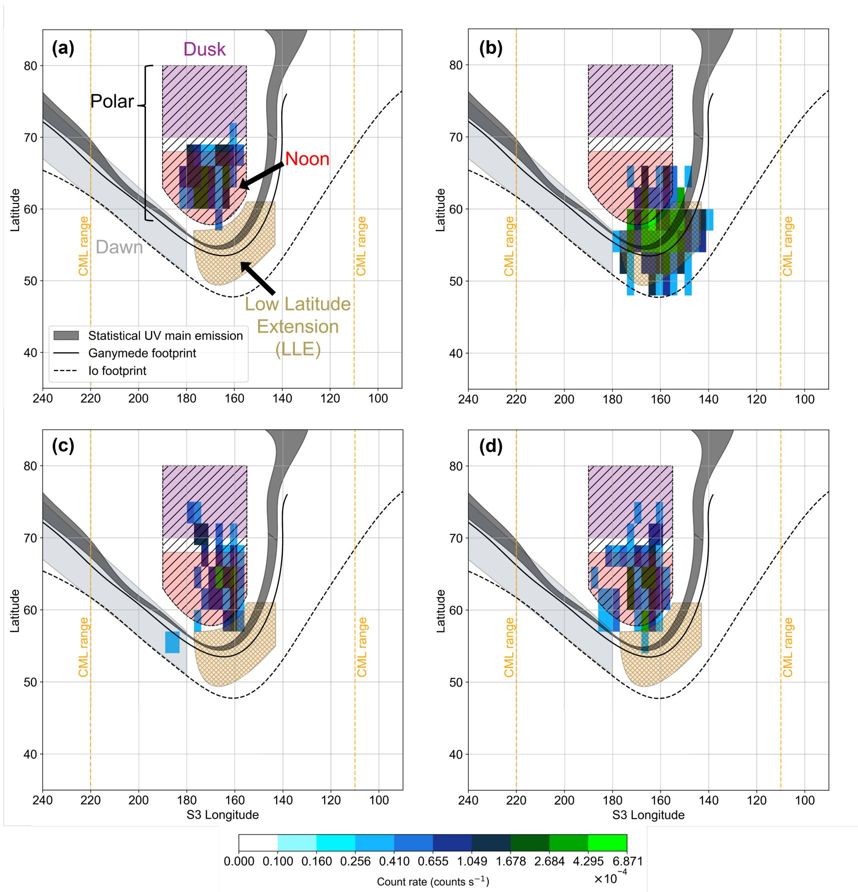
(a)
(b)
(c)
(d)
Dusk
Polar
Noon
Dawn
Low Latitude
Extension
(LLE)
CML range
Statistical UV main emission
Ganymede footprint
Io footprint
Latitude
S3 Longitude
0.000 0.100 0.160 0.256 0.410 0.655 1.049 1.678 2.684 4.295 6.871
×10^−4
Count rate (counts s^−1)

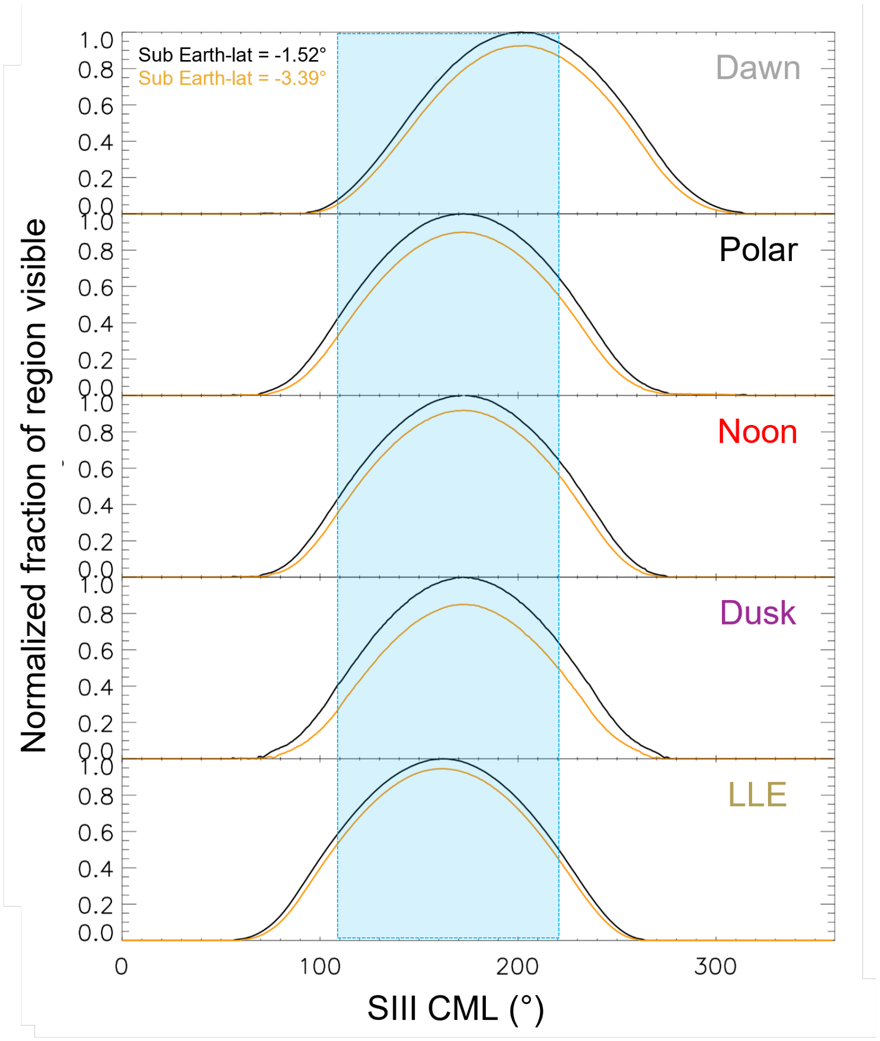
Sub Earth-lat = -1.52°
Sub Earth-lat = -3.39°
Dawn
Polar
Noon
Dusk
LLE
Normalized fraction of region visible
SIII CML (°)
0
100
200
300
1.0
0.8
0.6
0.4
0.2
0.0

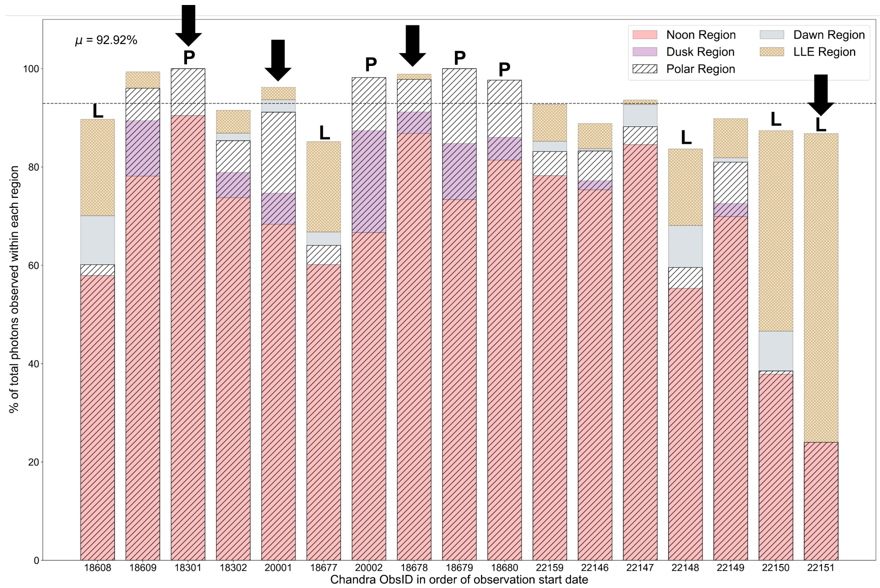

μ = 92.92%
Noon Region
Dusk Region
Polar Region
Dawn Region
LLE Region
% of total photons observed within each region
Chandra ObsID in order of observation start date
L
P
L
P
P
P
P
L
L
L
18608
18609
18301
18302
20001
18677
20002
18678
18679
18680
22159
22146
22147
22148
22149
22150
22151

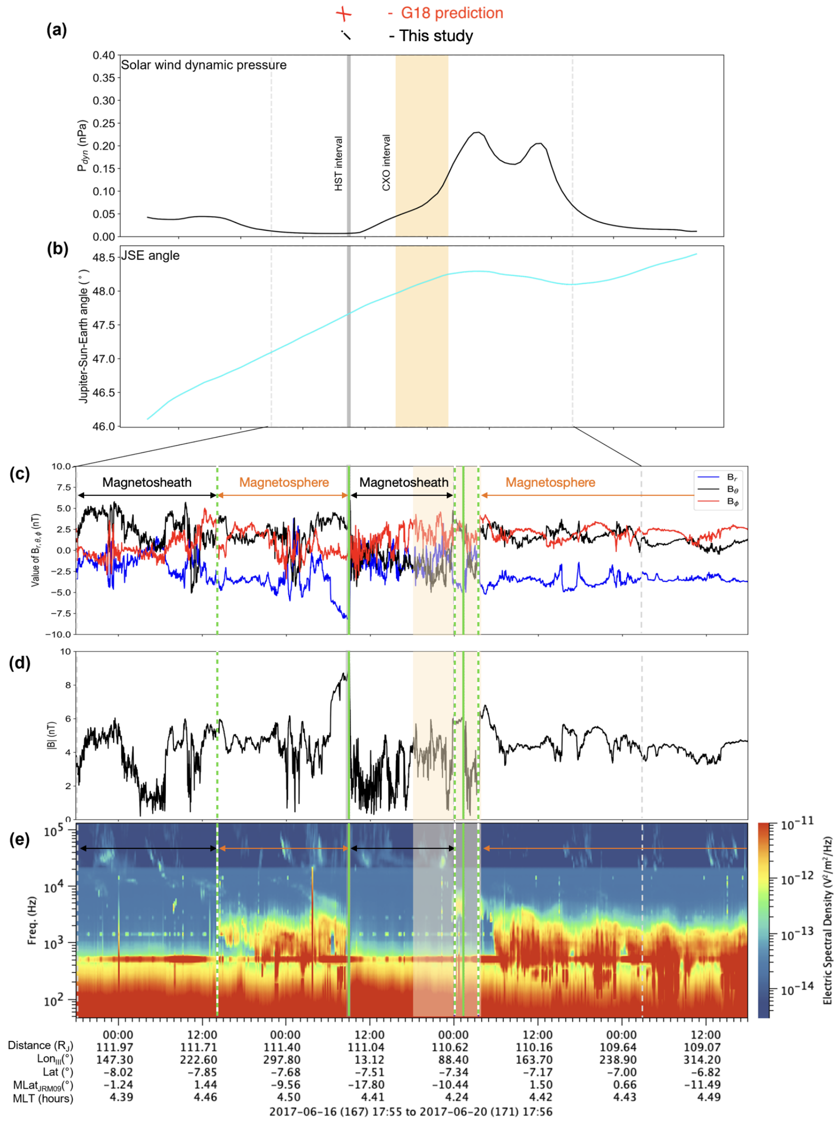

- G18 prediction
- This study
(a)
Solar wind dynamic pressure
P_dyn (nPa)
HST interval
CXO interval
(b)
JSE angle
Jupiter-Sun-Earth angle (°)
(c)
Magnetosheath
Magnetosphere
Magnetosheath
Magnetosphere
Value of B_r,θ,φ (nT)
B_r
B_θ
B_φ
(d)
|B| (nT)
(e)
Freq. (Hz)
Electric Spectral Density (V²/m²/Hz)
Distance (R_J)
Lon_III(°)
Lat (°)
MLat_JRM09(°)
MLT (hours)
2017-06-16 (167) 17:55 to 2017-06-20 (171) 17:56

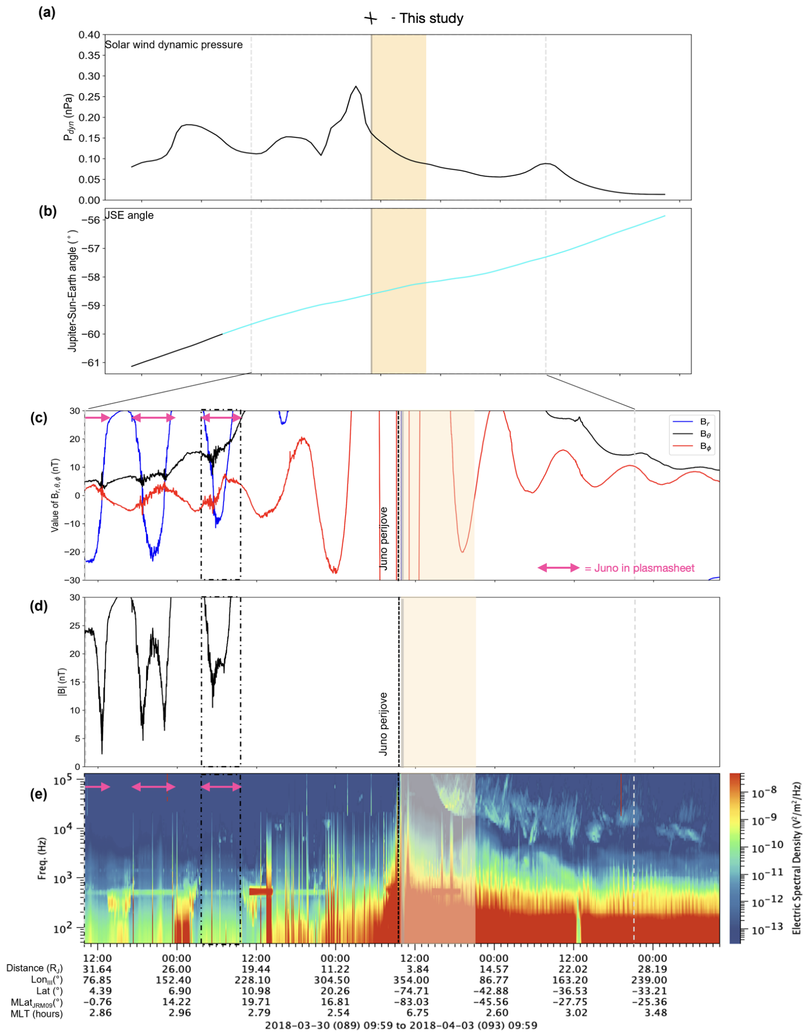

(a)
- This study
Solar wind dynamic pressure
P_dyn (nPa)
(b)
JSE angle
Jupiter-Sun-Earth angle (°)
(c)
Value of B_r,θ,φ (nT)
Juno perijove
B_r
B_θ
B_φ
= Juno in plasmasheet
(d)
|B| (nT)
Juno perijove
(e)
Freq. (Hz)
Electric Spectral Density (V²/m²/Hz)
Distance (R_J)
Lon_III (°)
Lat (°)
MLat_JRM09 (°)
MLT (hours)
12:00 31.64 76.85 4.39 −0.76 2.86
00:00 26.00 152.40 6.90 14.22 2.96
12:00 19.44 228.10 10.98 19.71 2.79
00:00 11.22 304.50 20.26 16.81 2.54
12:00 3.84 354.00 −74.71 −83.03 6.75
00:00 14.57 86.77 −42.88 −45.56 2.60
12:00 22.02 163.20 −36.53 −27.75 3.02
00:00 28.19 239.00 −33.21 −25.36 3.48
2018−03−30 (089) 09:59 to 2018−04−03 (093) 09:59

Identifying the variety of jovian X-ray auroral structures: tying the morphology of X-ray emissions to associated magnetospheric dynamics

D. M. Weigt[1,2,3], C. M. Jackman[2], D. Moral-Pombo[4], S. V. Badman[4], C. K. Louis[2], W. R. Dunn[5], S. C. McEntee[2,3], G. Branduardi-Raymont[6], D. Grodent[7], M. F. Vogt[8], C. Tao[9], G. R. Gladstone[10], R. P. Kraft[11], W. S. Kurth[12], J. E. P. Connerney[13,14]

[1]School of Physics and Astronomy, University of Southampton, Southampton, UK
[2]School of Cosmic Physics, DIAS Dunsink Observatory, Dublin Institute for Advanced Studies, Dublin, Ireland
[3]School of Physics, Trinity College Dublin, Dublin, Ireland
[4]Department of Physics, Lancaster University, Bailrigg, Lancaster, UK
[5]Department of Physics and Astronomy, University College London, London, UK
[6]Mullard Space Science Laboratory, University College London, Dorking, UK
[7]Laboratory for Planetary and Atmospheric Physics, Space Science, Technologies and Astrophysical Research Institute, University of Liège, Liège, Belgium
[8]Center for Space Physics, Boston University, Boston, MA, USA
[9]National Institute of Information and Communications Technology, Tokyo, Japan
[10]Southwest Research Institute, San Antonio, TX, USA
[11]Harvard-Smithsonian Center for Astrophysics, Smithsonian Astrophysical Observatory, Cambridge, MA, USA
[12]Department of Physics and Astronomy, University of Iowa, Iowa City, IA, USA
[13]Space Research Corporation, Annapolis, MD, 21403, USA
[14]NASA Goddard Space Flight Center, Greenbelt, MD, 20771, USA

Key Points:

- We present the morphology of new 'X-ray auroral structures', observed on Jupiter via Chandra's high spatial resolution camera.
- Our visibility modelling of these regions show that planetary tilt has very little effect on non-uniform auroral photon distributions.
- We show that combination of X-ray and UV 'auroral families' may be a useful proxy to determine the magnetospheric conditions at Jupiter.

Corresponding author: Dale Michael Weigt, `weigt@cp.dias.ie`

Abstract

We define the spatial clustering of X-rays within Jupiter's northern auroral regions by classifying their distributions into 'X-ray auroral structures'. Using data from Chandra during Juno's main mission observations (24 May 2016 – 8 September 2019), we define five X-ray structures based on their ionospheric location and calculate the distribution of auroral photons. The morphology and ionospheric location of these structures allow us to explore the possibility of numerous X-ray auroral magnetospheric drivers. We compare these distributions to Hubble Space Telescope (HST)and Juno (Waves and MAG) data, and a 1D solar wind propagation model to infer the state of Jupiter's magnetosphere. Our results suggest that the five sub-classes of 'X-ray structures' fall under two broad morphologies: fully polar and low latitude emissions. Visibility modelling of each structure suggests the non-uniformity of the photon distributions across the Chandra intervals are likely associated with the switching on/off of magnetospheric drivers as opposed to geometrical effects. The combination of ultraviolet (UV) and X-ray morphological structures is a powerful tool to elucidate the behaviour of both electrons and ions and their link to solar wind/magnetospheric conditions in the absence of an upstream solar monitor.

Plain Language Summary

The mechanism that allows precipitation of ions into Jupiter's atmosphere and generate pulsed X-ray auroral emissions is still under debate today. Previous studies have linked this driver to possible activity in Jupiter's outer magnetosphere (the interface between the solar wind and Jupiter) and have observed the emissions to exhibit variable behaviour. More recent studies have suggested a wide range of physical phenomena causing these emissions. Here we explore this idea in more detail by introducing five 'X-ray auroral structures' that map to different regions in the jovian system. Using data from the Chandra X-ray Observatory during Juno's main mission allows us to calculate the distribution of X-rays from Jupiter's northern auroral region. We compare our X-ray results with the ultraviolet emissions ('UV auroral families') observed from simultaneous Hubble Space Telescope (HST) data and infer the conditions at Jupiter using models and Juno observations. These 'X-ray structures' provide us with many ways to observe variable behaviour and provide a possible tool to monitor the solar wind conditions, when used in tandem with the HST 'UV auroral families'.

1 Introduction

The jovian auroral emissions are very complex and are highly variable in their morphological and temporal behaviour across multiple wavelengths [see full review by Badman et al. (2015) and references therein for more details]. The X-ray emissions remain the most elusive of the observable aurora with many recent studies trying to understand the highly sophisticated magnetospheric driver(s) capable of energising the ions to MeV energies that allow charge stripping and charge exchange to take place in the jovian ionosphere for soft X-ray (SXR: < 1 keV) production (e.g., Dunn, Branduardi-Raymont, et al. (2020); Dunn, Gray, et al. (2020); Houston et al. (2020)). The SXRs are produced from precipitating MeV ions originating in the outer magnetosphere and are sometimes observed to be coincident with flaring ultraviolet (UV) emissions within the UV active polar region as observed by Dunn et al. (2022) [herein refereed to as D22]. The auroral hard X-rays (HXR: > 2 keV) result from bremsstrahlung emissions from precipitating electrons, with the auroral emissions observed to sometimes coincide with the UV main emission (e.g., Branduardi-Raymont et al. (2008); Dunn et al. (2016)). This suggests that the precipitating electrons responsible for the HXR and UV main emission auroral emissions are likely to originate in the same region of the middle magnetosphere. Recent and ongoing studies are investigating how the X-rays are connected to other auroral emissions in the EM spectrum via plasma waves such as electromagnetic ion cyclotron (EMIC) waves associated with precipitating ions, which are shown to be strongly correlated with X-ray pulsations (e.g., Yao et al. (2021)). Other studies have looked at how the HXR are correlated with the more intense UV auroral emissions (Wibisono et al., 2021), such as dawn storms - major enhancements of the UV main emission along the dawn arc with a broadening in latitude (Bonfond et al., 2021; Yao et al., 2020).

Previous studies analysing the jovian UV aurorae from the Hubble Space Telescope (HST) have isolated various regions within the auroral emissions to explore the temporal and morphological variation across them. Nichols et al. (2009) used data from two 2007 Hubble Space Telescope (HST) campaigns to identify three northern UV auroral components: (1) the main oval (main emission), (2) low-latitude and (3) high-latitude auroral emissions. They calculated the auroral power, via analysis of the observations and visibility modelling of each region, and predicted solar wind conditions propagated from Earth to investigate the most likely cause of variation. Their results showed that generally the auroral power from the polar regions (low- and high- latitude auroral emissions) were uncorrelated with that of the main emission unless a dawn storm or enhancements due to a magnetospheric compression occurred. This may be a result of the polar emissions, in particular the swirl region observed to contain patchy and turbulent auroral emissions at the centre of the UV polar auroral emissions, having a strong local time dependence (Greathouse et al., 2021).

Nichols et al. (2017) followed up their previous study by segmenting the northern auroral region further, focusing on four regions of interest. These regions were applied to a larger HST dataset (around 47 orbits in total), covering May to July 2016 during Juno's (Bolton et al., 2017) final approach to Jupiter and its orbit insertion in the dawn flank of Jupiter's magnetosphere. By comparing the Juno *in situ* interplanetary data (McComas et al., 2017) and the HST UV auroral images they observed the intensity of the the main emission (at System III (SIII) longitudes $> 170°$) to increase for 1 - 3 days following compression events identified by Juno, with emissions on the polar dusk side to also brighten during these times and during shallow rarefactions of the solar wind. Auroral emissions equatorward of the main emission (at SIII longitudes $< 190°$) brightened ~ 10 days following enhanced Io plasma torus emissions observed from the EXtreme ultraviolet spetrosCope for ExosphEric Dynamics (EXCEED) on board Hisaki (Yoshioka et al., 2013). The noon active region did not show any clear correlation between intensity and interplanetary conditions, although the morphology was observed to change between periods of rarefactions and compressions. The variability of these emissions across the specific regions highlights how the auroral and magnetospheric dynamics change across different local times.

More recently, Grodent et al. (2018) [herein referred to as G18] characterised 118 HST images during Juno orbits 3 to 7 (from 30 November 2016 up to and including 18 July 2017), using six new definitions of "UV auroral families" to help provide a simplified description of the complex dynamics observed in the UV auroral emissions: (1) Q (or 'quiet') has a very low auroral power (< 1 TW) with a lower latitude main emission (ME); (2) N has a 'narrow' and expanded ME, exhibiting average power; (3) U describes more 'unsettled' conditions and is the intermediate behaviour between Q and N; (4) I is associated with strong injections with a 'corner-like' morphology, located at ionospheric dusk with (5) more moderate injections being represented by the i family. (6) The final family, X, is linked to 'eXternal' perturbations generating very strong and contracted ME with large enhancements at dawn and strong, narrow auroral arcs in the afternoon-dusk sector. Such behaviour is usually observed during solar wind compressions. These new definitions allowed different morphologies to be compared to establish logical, plausible connections to identify the responsible auroral driver and allowed a more detailed quantitative way to analyse variations of spatial behaviour. G18 observed that auroral emissions corresponding to the U family occurred most often (29.5% of 118 HST images) and were identified to be connected to the Q family due to slight changes in brightness of the ME. The connection was only interrupted by episodes of injection events (I, i) which were observed to precede or follow the N family. The moderate injections, i, were identified after auroral structures associated with compressions of the interplanetary medium (X). The disturbances from compressions can trigger episodic injections of trapped particles in the middle magnetosphere, as observed by Louarn et al. (2014) from Galileo particle and radio measurements. More details of the UV auroral families described here can be found in G18. Yao et al. (2020) found that dawn storms and injection events were correlated with intervals of tail reconnection and dipolarization.

In this study, we utilise the techniques used for the UV auroral emissions to isolate and define specific auroral structures and apply them to the concentrated northern X-ray emissions in an attempt to find a link between X-ray morphology and magnetospheric dynamics. We use concurrent HST data to help provide vital magnetospheric context to the Chandra (Weisskopf et al., 2000) observations, using the G18 auroral definitions, and model the visibility of the X-ray auroral structures we define here, similar to Nichols et al. (2009). We then compare the magnetospheric dynamics found from the X-ray-UV data and compare with the magnetospheric conditions identified from the Juno spacecraft, using radio (Kurth et al., 2017) and magnetometer (Connerney et al., 2017) data. This allows us to determine the state of the jovian magnetosphere and to compare against the solar wind predictions of the Tao et al. (2005) 1D magnetohydrodynamic (MHD) solar wind propagation model. Similar to the logic applied by G18, the goal of this study is to simplify the complex morphological variations of the X-ray aurora, allowing plausible connections to be made between the auroral emissions and magnetospheric dynamics. Linking our X-ray structures with the UV equivalent may provide additional context from which to infer the state of the jovian magnetosphere in the absence of upstream solar wind data.

Previous observations noted morphological variations in the X-ray aurora and attempted to connect this with solar wind conditions for a limited sample of observations taken in 2007 and 2011, for which interpretation was further challenged by limitations on viewing geometry (Dunn et al., 2016; Dunn, Branduardi-Raymont, et al., 2020; Dunn, Gray, et al., 2020). The work here, with a more comprehensive observation dataset supported by *in situ* insights from the Juno spacecraft, may also help to put these historic X-ray observations into context.

2 Contemporaneous remote sensing UV and X-ray observations with Juno Waves and MAG data

We use the catalogue of Chandra HRC-I (High Resolution Camera - Imaging: 30 arcmin × 30 arcmin field of view, with pixel size 0.13 arcsec and spatial resolution of 0.4 arcsec) observations defined and tabulated in Weigt, Jackman, et al. (2021), focusing on those taken during the Juno main mission (24 May 2016 up to and including 8 September 2019). The Chandra observations used here are a combination of HXRs and SXRs due to the very limited spectral resolution of HRC-I, meaning that we cannot segregate photons of these two energy regimes. However, previous work suggested that greater than 90% of the observed X-ray photons detected by Chandra ACIS (Advanced CCD Imaging Spectrometer) were soft X-ray photons Dunn, Branduardi-Raymont, et al. (2020) and the energy response of HRC is softer than ACIS, so that we expect the majority of detected X-ray photons to be produced by precipitating ions. These observations include those taken during Juno's approach to Jupiter (in the solar wind), while Juno was at apojove (near the dawn magnetopause), during several perijoves and intervals when Juno was inside and crossed the jovian plasmasheet. We then correct the Chandra observations using the updated mapping algorithm described in McEntee et al. (2022), assuming the altitude of X-ray emissions is 400 km above the 1-bar atmosphere, to ensure that we have accounted for the time-dependent degradation of the Chandra HRC-I instru-

Table 1. Table of concurrent Chandra and HST observations throughout the Juno era. Date and time of each observation, identified UV auroral families from current literature using the G18 definition and predicted solar wind dynamic pressure from the Tao et al. (2005) model with average Jupiter-Sun-Earth angle are shown. Bold entries highlight observations associated with possible eXternal perturbation (X) structures. Solar wind parameters determined over a 2 day window centered on the Chandra observation to account for propagation errors withn Tao et al. (2005) model. Each Chandra observation is labelled with a unique Observation ID (ObsID).

Observation start date (dd/mm/yyyy)	Chandra ObsID	Observation interval (Juno time; light corrected)		HST UV northern auroral family*			Mean solar wind† P_{dyn} (nPa)	Max solar wind† P_{dyn} (nPa)	Mean Jupiter-Sun-Earth angle† (°)
		Chandra	HST	G18[a]	This study	D22[b]			
24/05/2016	18608	09:39 - 20:41	17:03 - 17:47 20:14 - 20:58	- -	U U	Q/N U	0.006	0.007	∼ 57.7
01/06/2016	18609	10:47 - 21:49	14:13 - 14:57 17:24 - 18:08	- -	U U	Q/N Q/N	0.138	0.309	∼ 64.6
02/02/2017	18301	09:14 - 18:19	16:17 - 16:57	-	i	i	0.009	0.015	∼ -79.9
28/02 (Chandra); 01/03/2017 (HST)[c]	20000[c]	11:58 - 07:34	14:37 - 15:16	i	i	-	0.019	0.024	∼ -53.3
18/05 - 19/05/2017	18302	23:48 - 10:10	04:27 - 05:07 06:03 - 06:43	N N	N N	N N	0.052	0.148	∼ 19.2
18/06/2017[c]	**20001**[c]	**17:55 - 04:06**	**08:31 - 09:13**	**X**	**i**	**-**	**0.090**	**0.230**	**∼ 47.9**
06/08/2017[d]	20002[d]	01:07 - 10:50	-	-	-	-	0.015	0.024	∼ 99.0
01/04/2018	**18678**	**09:59 - 21:06**	**09:59 - 10:17**	-	**X**	**-**	**0.116**	**0.275**	**∼ - 58.4**
23/05 - 24/05/2018	18679	23:22 - 10:21	09:02 - 09:32	-	U	Q	0.049	0.115	∼ -3.6
06/09/2018	**18680**	**19:50 - 06:56**	**04:22 - 05:02**	-	**i**	**X**	**0.056**	**0.086**	**∼ 97.0**
29/05/2019	22159	02:50 - 12:34	12:18 - 12:56	-	i	-	0.014	0.019	∼ -32.5
15/07/2019	22148	12:21 - 19:13	14:06 - 14:44 15:41 - 16:17	- -	U U	N Q	0.068	0.115	∼ 10.5
16/07/2019	22149	08:07 - 15:00	10:43 - 11:21	-	N/i	N	0.057	0.096	∼ 11.3
18/07/2019[c]	22150[c]	19:40 - 01:32	14:10 - 14:49	-	i	-	0.012	0.018	∼ 13.9
08/09/2019	**22151**	**08:01 - 14:46**	**14:24 - 15:02**	-	**X/i**	**-**	**0.262**	**0.879**	**∼ 64.0**

* UV families as described in Grodent et al. (2018)
† Predicted values from Tao et al. (2005) model over 2 day window centered on Chandra observation
[a] UV families identified from Grodent et al. (2018) (G18)
[b] UV families identified from Dunn et al. (2022) (D22).
[c] observations not concurrent but occurred ± 1 day from Chandra interval.
[d] inferred compression from Juno data, no HST data.

ment while removing any contaminant background (Weigt et al., 2022). Here our focus is on the brightest and most concentrated X-ray northern auroral emissions, located using the Weigt et al. (2020) numerical criterion of >7 photons per 5° SIII longitude × 5° latitude over ∼ 10 hours (the average duration of the observations of the catalogue, around a jovian rotation). We note using this more updated mapping method provides minimal change in X-ray count rates from the Weigt, Jackman, et al. (2021) study and therefore does not change the interpretation of these results. We highlight here that accounting for the instrument's increasing degradation (and particle background) is crucial for future studies during the Juno extended mission (especially when mapping X-ray emissions to the jovian disk). The degradation of HRC-I has also been observed when analysing time-tagged photon data in a low-count regime from Saturn (Weigt, Dunn, et al., 2021).

To help provide essential magnetospheric context to the X-ray auroral emissions, we use HST observations concurrent with Chandra data. We analyse 17 Chandra observations during the Juno-era, 14 of which have HST Space Telescope Imaging Spectrograph (STIS: 24.7 arcsec × 24.7 arcsec field of view, spatial resolution of 0.0025 arcsec) data ± 1 day from the Chandra window, to allow the magnetospheric conditions to be analysed in detail. STIS detects far ultraviolet (FUV) auroral emissions of wavelengths ∼ 130 - 180 nm (photon energies ∼ 7 - 10 eV) using the F25SRF2 filter to eliminate geocoronal Ly-α contamination and to reduce the reflected sunlight from the jovian disk (e.g., Grodent (2015)). These 14 HST observations focus on the northern auroral emissions of which components within the UV aurora have been identified using the G18 definitions. We note that we add to this catalogue with three newly identified HST observations coinciding with Observation ID (ObsID) 22159 (29 May 2019), 22150 (18 June 2019) and 22151 (8 September 2019). All observations used in this research are shown in Table 1. To compare with contemporaneous Juno data, both the Chandra and HST intervals have been corrected for the Juno-Earth light-travel time, taken from ephemeris data obtained via the JPL Horizons database (data available at `https://ssd.jpl.nasa.gov/horizons/app.html#`). The mean and max dynamic pressure (P_{dyn}) estimated from the Tao et al. (2005) 1D MHD model over a 2 day window centered on the Chandra interval with the corresponding average Jupiter-Sun-Earth (JSE) angle are also given in Table 1. This 2-day window is used for all observations irrespective of JSE angle to account for propagation and interpolation errors. We note that Chandra observations taken beyond 8 September 2019 (and after the creation of the Weigt, Jackman, et al. (2021) catalogue) have no direct overlap with any HST campaigns and are therefore not included in this study.

We then compare these observations to remote sensing radio data (spectrograms) from Juno Waves and *in situ* data (time series) from the magnetometer, Juno MAG to confirm the magnetospheric state during these intervals and potentially identify any internal magnetospheric drivers (e.g. such as particle injection signatures). Juno's eccentric polar orbit allows it to sample the inner, middle and outer magnetosphere during its 53-day orbit, providing us the opportunity to analyse the different internal auroral drivers, hence the auroral emissions, located throughout the jovian magnetosphere. We take this into account when interpreting these data.

3 Results

Following studies that have identified different regions within the UV emissions associated with different potential drivers (e.g., Grodent et al. (2018)), we apply similar logic to the X-ray northern auroral emissions from the Weigt, Jackman, et al. (2021) Chandra catalogue during the Juno-era. Here we use the families defined from UV emissions from concurrent HST observations to provide vital context to the concentrated northern X-ray emissions and use the superior spatial resolution of HST-STIS to model the visibility of each X-ray auroral region.

3.1 Identifying X-ray auroral structures

As analyzed in the statistical study by Weigt, Jackman, et al. (2021), it is clear that the northern X-ray emissions exhibit large variations in morphological and temporal behaviours with only a very small region of X-rays appearing across the entire $\sim$ 20 year Chandra HRC-I dataset: the averaged hot spot nucleus (AHSNuc), mapping to the noon magnetopause boundary. We show examples of 2D histograms of mapped concentrated X-rays, using the Weigt et al. (2020) numerical criterion, in Figure 1 within the *X-ray noon* region (red), where the colour bar shows the photon flux of the X-rays (counts s^{-1}) and the 1D histograms show the latitude (lat) and System III longitude (SIII lon) distribution of the X-ray emissions. Similar to the 'Region X' defined in D22, the X-ray noon region contains both the UV swirl and active regions (Grodent et al., 2003) and therefore the X-ray emissions they may generate. The remaining X-ray auroral structures we define here are *X-ray dusk* (purple), *X-ray dawn* (gray), the *Low Latitude Extension region* (LLE; gold), equatorward of X-ray noon and the *X-ray polar region* (striped region) which envelopes both the noon and dusk structures. The statistical UV main emission (accounting for a compressed and expanded magnetosphere) and Io and Ganymede magnetic footprints taken from Bonfond et al. (2017) are also plotted to provide context of the location of these regions within the magnetosphere. The coordinates of each region (in SIII lon, lat) are given in the Supplementary Information (SI: see Data Set S1).

In Figure 1 (covering a central meridian longitude (CML) of 110° - 220°), we show four examples of different auroral morphologies each under different conditions: (a) where all auroral emissions are within the polar region (ObsID 18301: 2 February 2017); (b) where the most intense auroral emissions are observed to be shifted equatorward (ObsID 22151: 8 September 2019); (c) auroral morphology during a compressed magnetosphere (ObsID 20001: 18 June 2017) and (d) an observation during Juno a apojove (ObsID 18678: 1 April 2018). Three out of the four cases show the majority of the concentrated, and most intense, X-ray emissions are located in the X-ray polar region, dominated by X-ray noon. These emissions are therefore likely to be co-located (and possibly linked) with the UV activity in the polar and swirl regions and possibly coincide with flaring UV emissions (e.g., Elsner et al. (2005); Dunn (2022)). Previous studies (e.g., Grodent et al. (2003); Grodent (2015); Greathouse et al. (2021) and references therein) have also identified the polar active region as the most dynamic of the UV polar emissions, producing flares and bright arc sub-structures of a few hundred kilo-Rayleigh (kR) lasting in the order of a few minutes. The examples shown in Figure 1 are discussed further in the remainder of Section 3.

The X-ray dawn region is found to coincide with a portion of the main emission and the Io footprint suggesting an association between dawn storms, injections of hot plasma from the middle magnetosphere (e.g., Gerard et al. (1994); Kimura et al. (2017)) and bright X-ray populations. Recent work by Wibisono et al. (2021) found the intensity of the HXRs to increase during the presence of a dawn storm with reduced activity from the more poleward SXRs, utilising the energy resolution of XMM-Newton. Regions of X-ray dawn at higher latitudes are likely to overlap with the UV dark polar region (DPR) which contains very little UV emissions and is observed to contract and expand as Jupiter rotates, mapping to the outer magnetosphere (e.g., Pallier and Prangé (2001); Grodent et al. (2003); Swithenbank-Harris et al. (2019)). The DPR has been found to be the likely location of empty flux tubes, emptied via Vasyliūnas-like reconnection in the tail which then rotate to the dayside magnetosphere (Vasyliūnas, 1983), resulting in very little UV emissions here. Recent work by D22 found that the DPR is also present within the X-ray northern auroral emissions. D22 deduced from Chandra and HST observations (and simulated data) that very few or no X-ray photons are to be located in the DPR. They confirm this conclusion from their Monte Carlo simulations which state that the likelihood of X-rays being emitted from the DPR is very small, including

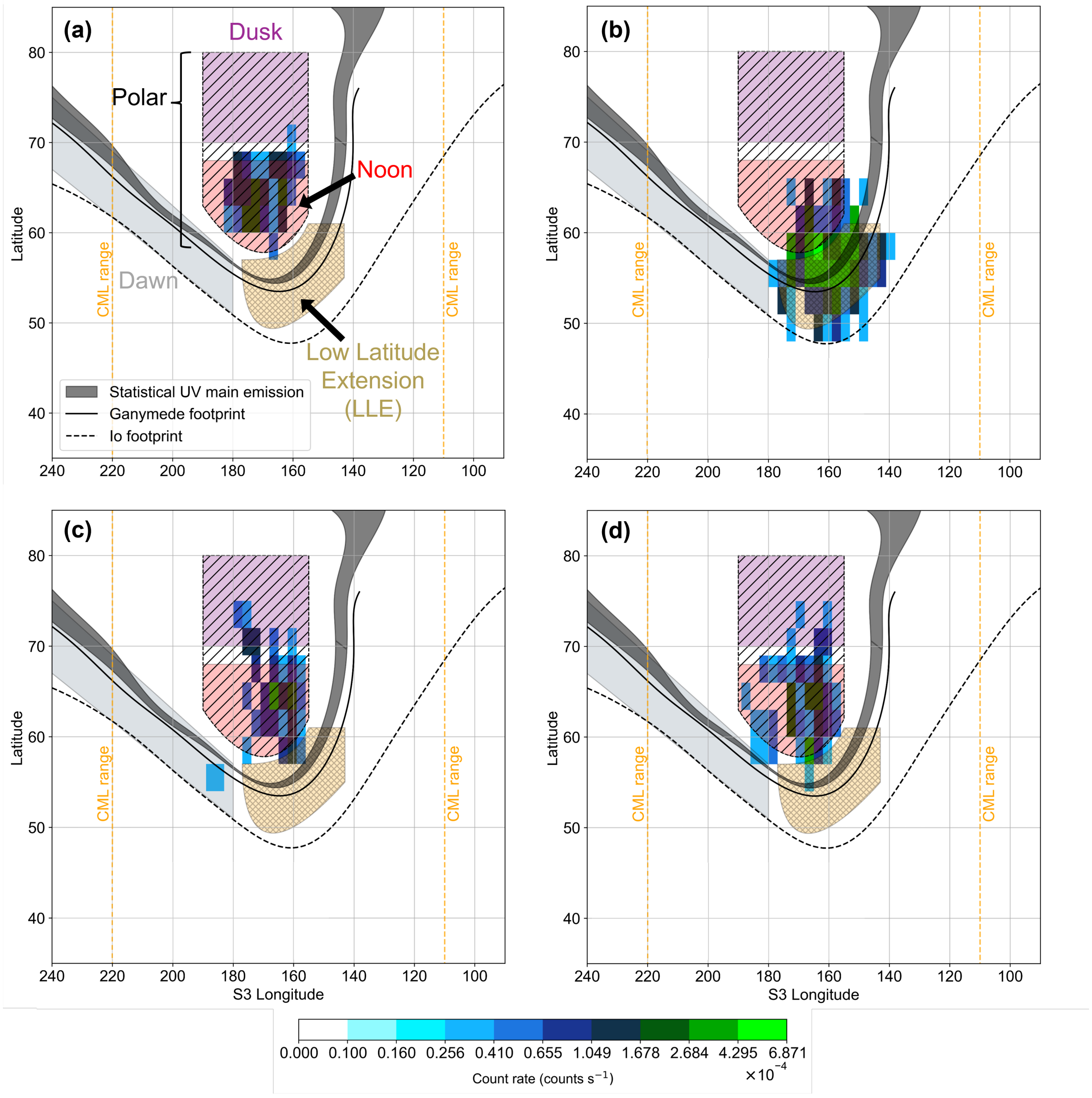

Figure 1. A Cartesian plot of the X-ray mapping for four example Chandra observations analysed in this research, each under different conditions: (a) ObsID 18301 (2 February 2017), where all auroral emissions are within the polar region; (b) ObsID 22151 (8 September 2019), where the auroral emissions are shifted equatorward; (c) ObsID 20001 (18 June 2017), auroral morphology during a compressed magnetosphere and (d) ObsID 18678 (1 April 2018), CXO observation during Juno apojove. Each case is expanded upon in the remainder of Section 3. The location of the X-ray auroral structures as described in the text (red: noon; purple: dusk; gray: dawn; gold: LLE; striped: polar) are shown in each panel and are labelled in (a). The count rates (counts s^{-1}) of the concentrated X-ray auroral emissions (2D histogram: binned by 3° SIII lon × 3° lat) are given by the colour bar. The statistical UV main emission accounting for compressed and expanded states (dark gray shading), and the footprints of Io (black-dashed line) and Ganymede (solid black line) are overplotted (Bonfond et al., 2017). The X-ray emissions mapped and analysed for this research are selected from a 9000 ± 1080 s interval, covering a central meridian longitude (CML) range of 110° - 220° (i.e. optimum visibility for each region as shown in Figure 2). This CML range is overplotted with orange dashed lines.

possible scattering of solar X-ray photons in the jovian upper atmosphere as an explanation for the sporadic and very dim X-ray emissions in the Dark region.

The regions likely to contain more extreme cases of auroral activity are the X-ray dusk (see Figures 1 (c) and (d)) and LLE regions (Figure 1 (b)) where the brightest emissions may span poleward or equatorward of the nominal position as found by Weigt, Jackman, et al. (2021), where it was observed that concentrated X-ray photons are occasionally (30 - 70% occurence) found at latitudes between 54° and 75°. Therefore these regions will likely contain rare auroral morphologies linked to more unusual or extreme magnetospheric dynamics. The LLE region covers an area of UV auroral emissions possibly associated with active particle injections from the middle magnetosphere driven by reconnection events and dipolarizations of the jovian magnetic field (e.g., Dumont et al. (2014, 2018); Yao et al. (2020)). Such injection events are found to occur alongside dawn storms, suggesting disturbances of the middle magnetosphere at a range of local times (e.g., Gray et al. (2016)). The 2-D histograms for all observations analysed and corresponding plots highlighting the filtering performed on the concentrated X-ray lightcurves photons using our CML criterion can be found in the SI (Figures S1 and S2).

3.2 Visibility and distribution of auroral photons across the X-ray auroral structures

The tilt of Jupiter, as viewed from the observer, can lead to issues of viewing geometry of the planet when using remote sensing data (e.g., Dunn et al. (2017); Dunn, Branduardi-Raymont, et al. (2020); Weigt, Jackman, et al. (2021)). As the magnetic field at the South pole is more dipolar, this tilt of the planet affects these emissions the most when viewed from Earth. However we cannot completely neglect such effects when viewing the northern emissions as the longitude of the observer (or CML) can change what parts of the emissions are observed. To resolve such issues, we utilise the higher spatial resolution of the HST-STIS instrument compared to Chandra to model the visibility of each X-ray auroral structure, using the area of the region defined in SIII lon and lat as they rotate into view of HST-STIS. We use the number of visible pixels of each X-ray region as it rotates into view as a proxy to gauge the visibility of our X-ray structures as viewed by an observer at Earth. In other words, we analyse how much of an effect the tilt of the planet has when observing fixed regions (in SIII lon and lat) on Jupiter from any Earth-based instrument. We define the visibility here as the number of visible STIS pixels associated with each X-ray region during one jovian rotation. We assume that the emissions across the area of the defined X-ray structures used in the model were uniform.

We adopt the method of Nichols et al. (2009) used to measure the visibility (as a function of normalized power) of different isolated components of UV auroral emissions during two HST campaigns in 2007, using the Advanced Camera for Surveys (ACS) Solar Blind Channel (SBC). Here we apply this algorithm to the X-ray structures, using the ionospheric position and size of each region as viewed by HST-STIS (with greater resolution than Chandra). Figure 2 shows the results of our visibility modelling over a full jovian rotation (e.g. full CML coverage) for the highest (orange: -3.39°) and lowest (black: = -1.52°) sub-Earth latitude during the Juno main mission for all X-ray auroral structures. The sub-Earth latitude relates to how tilted Jupiter is away from the observer, resulting in the peak for both cases being different. Here, we define the visibility as the number of pixels visible for each of the X-ray regions normalized to the maximum for the lowest planetary tilt case. The CML range (110° to 220°) used throughout this study is also overplotted in light-blue.

The location of peak visibility in all panels is associated with the optimum CML of which the full region is in view and is therefore related to the ionospheric position of the X-ray structure. The width of the peak gives an indication of the size of the region of interest. As shown in Figure 2, the location and width of the modelled peak visibil-

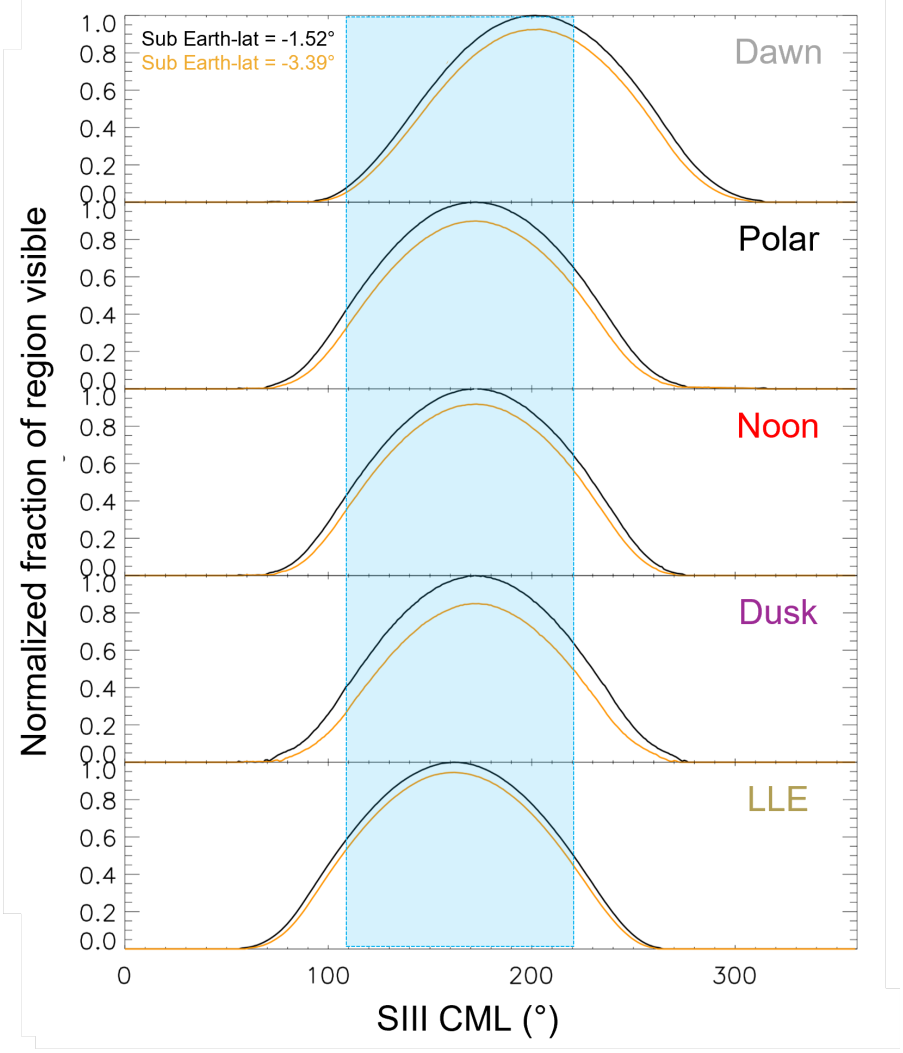

Figure 2. Plot showing the modelled normalized visibility for a full jovian rotation of each northern auroral region as observed from STIS on board HST. We model the visibility during the smallest (black: = -1.52°) and largest (orange: -3.39°) planetary tilt as viewed from Earth (sub-Earth latitude) during the Juno main science mission. The CML range used to analyse the concentrated X-ray emissions is overplotted with the light-blue shaded area. The number of pixels visible for each region is normalised to the maximum for the sub-Earth latitude = -1.52° case.

ity for the polar, noon and dusk regions (labelled with the same colours corresponding to the regions in Figure 1) are very similar as expected as all regions span the same SIII lon range. The main discrepancies are associated with the amplitude of the peak with the dusk region having the fewest number of visible pixels resulting from the region being more poleward and more difficult to view with HST-STIS [see Grodent (2015) for more details] and therefore more sensitive to sub-Earth latitude. The peak visibility of all the X-ray auroral structures lie within our CML range and therefore likely associated with the peak of the X-ray light curve of the northern emissions. We note X-ray noon is also affected by sub-Earth latitude to an extent, but the normalized fractional visibility still remains above 0.8 (i.e. $> 80\%$ of all pixels visible to noon) during the more restricted viewing geometry. Since the polar region is the accumulation of visible pixels from both X-ray noon and dusk, the modelled visibility curve is, as expected, a combination of both regions. The dawn region spans greater longitudes and surrounds the polar emissions, following a portion of the dawn main emission leading to the peak visibility shifting to higher CMLs. As the shape of X-ray dawn region is longer in size (i.e. spans a greater range of longitudes) the peak of the visibility curve is broader, as it is less sensitive to the tilt of the planet. This region is more equatorward than the X-ray polar region. This is similar for the LLE region, although this auroral structure spans the smallest range of longitudes out of the X-ray structures which is reflected by the width of the visibility curve. Although none of these results are particularly surprising, this is the first time the visibility of the X-ray auroral emissions has been modelled in this way.

The distributions of auroral X-ray photons within each of the auroral structures for each Chandra observation are shown as a stacked bar chart in Figure 3, with the ObsIDs in order of observation start date (as shown in Table 1) throughout the duration of Juno's main mission. Each region is represented by the same colours and labels used in Figure 1 with all four examples indicated by a black arrow. The mean number of total auroral photons populating the X-ray structures, μ, is given by a horizontal dashed line with a value 92.92%. In other words, $\sim 93\%$ of northern X-ray auroral emissions are likely to be located within the described X-ray regions. Observations where the sum of the components are $< 100\%$, as shown in Figure 3, indicate that concentrated emissions were also mapped to regions outside the X-ray auroral structures. The X-ray emissions used in the stacked bar chart, and mapped using the 2D histogram in Figure 1, span the same CML interval ($110°$ - $220°$) including the peak visibility of all regions. As many of the X-ray observations have different exposure times, this ensures we are removing any observation bias as the same portion of all northern auroral emissions is observed in each of the Chandra campaigns.

As shown by the highlighted example [introduced in Figure 1 (a): ObsID 18301] in Figure 3 and three other observations (ObsID 20002 (no HST intervals during this time), 18679 and 18680; details of the observations in Table 1), $\geq 95\%$ of concentrated northern auroral emissions are located within the X-ray polar region, and are dominated by X-ray noon photons. During these intervals there were no dawn or LLE region photons detected despite these regions being in view of Chandra at the time. However, many other observations have auroral photons located in this range within the same viewing and timing restraints. This therefore suggests that the potential drivers that cause emissions in these regions may be "switched off". Further evidence of this is shown by the observations that had a higher population of LLE photons ($> 10\%$ of total photons) with no X-ray dusk emissions (ObsID 18608, 18677, 22148, 22150 and 22151). This suggests that during these intervals, the concentrated X-ray emissions were located equatorward of the main emission and displaying more extreme morphological behaviour when compared to the averaged map of northern auroral emissions (Weigt, Jackman, et al., 2021). This is shown by the low occurrence rate of the X-ray emissions (using the same SIII lon/lat binning). The most extreme example, ObsID 22151 (8 September 2019: Figure 1b)), is a very rare case of the majority of the auroral emissions mapping to beyond the polar region. Examples where the auroral emissions span the LLE and X-ray dusk regions (e.g.,

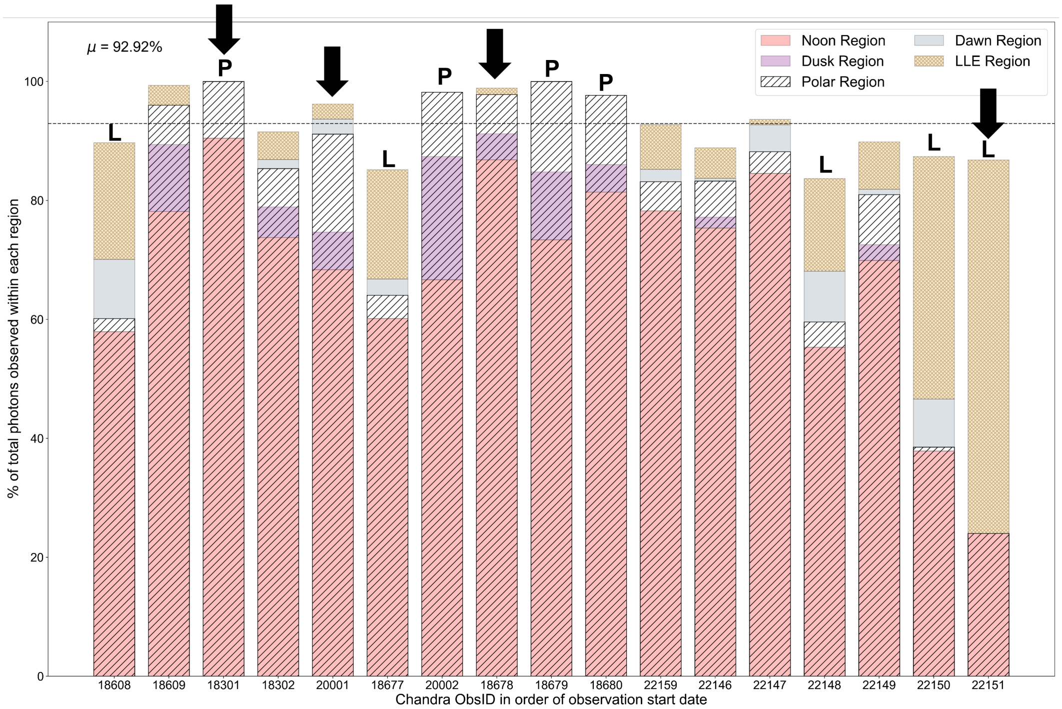

Figure 3. Stacked bar chart showing the distribution of all concentrated X-ray auroral emissions in each structure across the Juno-era Chandra observations (in order of date: Table 1), within the CML range. Each structure in both panels are labelled with identical colouring used in Figure 1. The mean, μ, is given and indicated by the horizontal line. The letters 'P' and 'L' above the bars indicate auroral morphologies that fall into either the 'fully polar emissions' or 'low latitude emissions' categories respectively, as defined in the text. The examples shown in Figure 1 are highlighted by black arrows.

18609, 18678, 22149) and an additional smaller population at X-ray dawn (20001, 18302, 22159) highlight possible elongation of the auroral emissions in both poleward and equatorward directions and/or possible X-ray emissions associated with UV injections.

From Figure 3, we can pick out two categories: (1) fully polar emissions (i.e. X-ray polar population $\geq 95\%$ of all auroral emissions) and (2) low latitude emissions (i.e. LLE photon population $> 10\%$). These observations are labelled with 'P' and 'L' for both categories respectively. The observations that exhibit intermediate behaviour between both categories (i.e. no 'P' or 'L' label) may imply a time-dependent relationship and therefore a link between the two. We do however need to compare the mapping of these morphologies with HST and Juno data to verify such a state. The key result we present here is the lack of uniformity across Figure 3 which shows that different regions can dominate when observing the northern concentrated X-ray auroral emissions. Adding a magnetospheric context this may suggest either that: (i) the switching on/off of potential magnetospheric drivers is likely to dominate or (ii) the regions where conditions are right for wave growth (i.e. standing Alfvén waves and/or EMIC waves on the magnetopause boundary) is changing. This is emphasized in Figure S3 (in SI) which shows scatter plots of photons observed in the polar region versus the LLE region and both regions plotted against inferred solar wind conditions from the Tao et al. (2005) model. As reflected in Figure 3, we observe an anticorrelation between photons population the polar and LLE regions. There is no clear link between solar wind dynamic pressure and these populations. This may indicate that either disturbances from the solar wind are observed in multiple regions and/or the LLE region 'switching on' is not directly linked to the compression and may lag ahead/behind the disturbance (i.e. similar to i/I-family). Further exploration into this is beyond the scope of this work although we hope our results will highlight key examples to use in future case studies.

3.3 Using *in situ* and remote sensing diagnostics to infer magnetospheric state

In order to understand the state of the jovian magnetosphere during the Chandra interval and constrain the driver(s) responsible for variable X-ray aurora, we combine predicted solar wind conditions from the 1D MHD propagation model by Tao et al. (2005) with data from the Juno fluxgate magnetometer (Juno MAG) and the radio and plasma wave instrument (Juno Waves). The purpose of the model is to infer how solar wind conditions can cause the jovian magnetosphere to contract and/or expand. We can therefore infer the state of the jovian magnetosphere, within an error of 2 days centred on the Chandra observation based on the alignment of the Sun, Earth and Jupiter. We also compare the predicted UV auroral families during the interval to the Juno data to verify the auroral behaviour and morphology. The aim here is to combine the UV and X-ray predicted morphologies with observed solar wind conditions as a possible proxy for magnetospheric conditions when there is no upstream *in situ* data.

Figure 4 shows the results of the Tao et al. (2005) 1D MHD solar wind propagation model combined with Juno MAG and Waves data, covering 4 days centred on the Chandra (CXO) observation (shaded in orange) taken on 16 June 2017 (ObsID 20001 - see Table 1 and Figure 1c)). The propagation model predicted many intervals where the solar wind dynamic pressure ($P_{\rm dyn}$) was increased when acting on the jovian magnetosphere within model error, during a relatively reasonable Jupiter-Sun-Earth (JSE) alignment (panels (a) and (b)). We only consider JSE angles $< |60°|$ (highlighted in cyan) to ensure that the errors of the model are within the 2 day window, centered on the CXO interval. This conservative angle range allows us to explore of the Chandra catalogue, and compare how the model performs with real *in situ* data. The HST observation is shown by the gray interval. Both CXO and HST observations lie within the 2 day window accounting for errors in the Tao et al. (2005) model (gray dashed lines). This example was selected as this Chandra interval and Juno particle data were previously anal-

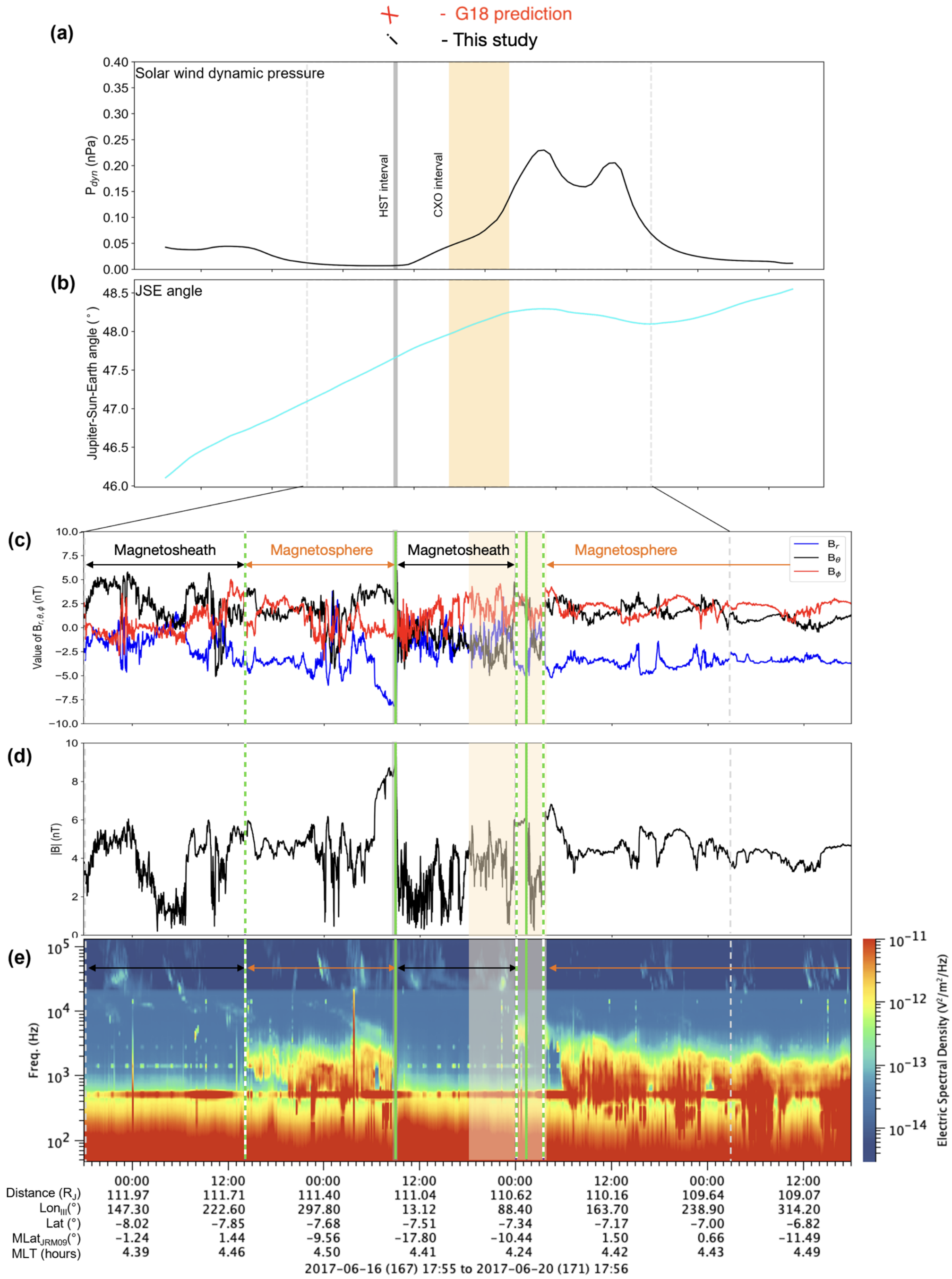

(Caption on next page)

Figure 4. Multi-panelled plot combining the results from the Tao et al. (2005) 1D MHD solar wind propagation model with Juno MAG and Waves, covering 4 days centring the Chandra observation (orange area) taken on 16 June 2017 (ObsID 20001 - see Table 1 for more details). Panels (a) and (b) show the predicted solar wind dynamic pressure (P_{dyn}) and associated JSE angle respectively, evolving over time with the Chandra (CXO) and HST observing intervals (gray area) shown in all panels. The angle represented in cyan shows periods of time when the value is $< |60°|$. Panels (c) and (d) show the Juno MAG in spherical components (B_r: blue, B_θ: black, B_ϕ: red) and the total field strength ($|B|$) measured by the Juno MAG data, in units of nanotesla (nT), within the Tao uncertainty window used in our analysis. (dashed gray vertical lines: shown in all panels). Panel (e) shows the concurrent Juno Waves data, measuring the electric spectral density of the radio and plasma wave emissions. The Juno ephemeris data during this interval is displayed at the bottom, showing its position in Jupiter's System III frame (in radial distance from Jupiter, R_{J}, and magnetic local time (MLT; hours)) and its position projected onto Jupiter's surface (SIII lon (Lon$_{III}$; degrees), SIII lat (Lat; degrees) and magnetic latitude found from the JRM09 field model (MLat$_{\mathrm{JRM09}}$; degrees)). The green-white dashed and solid green vertical lines represent Juno making inbound and outbound crossings of the magnetopause boundary respectively, as identified from Juno JADE data as described in Weigt et al. (2020). Juno's known position in the magnetosheath (black arrows) and magnetosphere (orange arrows) are also labelled. The identified UV auroral family using the Grodent et al. (2018) definitions from G18 (red) and this study (black), as shown in Table 1, are at the top of panel (a).

ysed by Weigt et al. (2020) to identify magnetopause crossings to infer a dynamic pressure from the Joy et al. (2002) model. When compared to the distributions of solar wind dynamic pressure (P_{dyn}) identified by Jackman and Arridge (2011) from upstream solar wind data at Jupiter spanning 1973 to 2004, both the Tao model and Juno data find the jovian magnetosphere to be compressed during this time ($P_{\mathrm{dyn}} = \sim 0.23$ - 0.39 nPa). These values lie at the upper tail of the distribution where the typical P_{dyn} observed from spacecraft data was 0.04 nPa.

The magnetopause crossings identified by Weigt et al. (2020) from Juno JADE data (green-white dashed and green solid vertical lines represent Juno making inbound and outbound respectively) are confirmed in the other Juno datasets (as shown in panels (c) - (e)) with a sharp change in the total magnetic field strength ($|B|$), in units of nanotesla (nT), and its spherical components (B_r: blue, B_θ: black, B_ϕ: red). The character of the magnetic field also changes during a crossing as it is noisier in the magnetosheath than in the magnetosphere. To locate the magnetopause boundary crossings (labelled with orange and black arrows), one can look at the Waves data (panel (e); colour bar showing the electric spectral density of the radio emissions), and in particular the appearance/disappearance of the non-thermal trapped continuum emissions (as conducted by Hospodarsky et al. (2017)). These emissions, observed between the electron plasma frequency and ~ 10 kHz, located in the jovian magnetospheric cavity where the emission frequency exceeds that of the surrounding plasma frequency (e.g., Gurnett and Scarf (1983)). When in the magnetosheath, the trapped continuum emissions are blocked by the denser sheath plasma. These emissions appear again when Juno enters the more rarefied magnetospheric plasma. These transitions in electric spectral density also align with the identified Juno crossings.

Finally, during the series of compressions Grodent et al. (2018) found that the UV auroral emissions exhibited features associated with the X-family (red label above panel (a)), suggesting that the magnetosphere was being affected by a solar wind compression

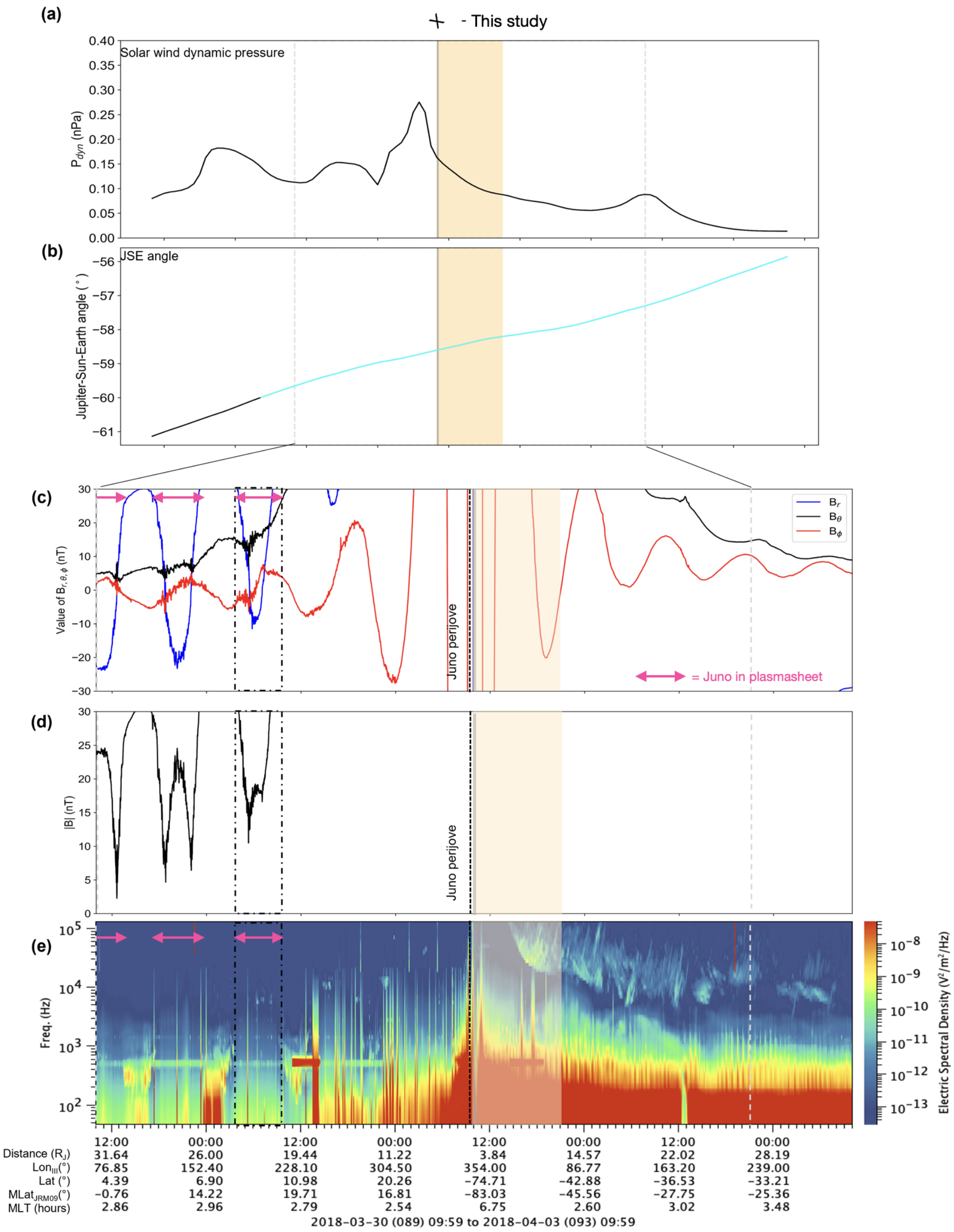

Figure 5. Multi-panelled plot for ObsID 18678 (1 April 2018) in identical format to Figure 4. The interval of the Juno perijove is shown by the black dashed line. Dotted black box highlights interval of potential dipolarization of the magnetic field (mainly in B_θ) associated with possible injection events in the UV aurora. The Grodent et al. (2018) UV family identified in this study is shown at the top of panel (a). Intervals when Juno is in the plasmasheet, identified from Juno Waves, prior to perijove are shown with pink arrows.

region. When comparing these results to Figure 3, the X-ray auroral emissions spans across multiple regions and are dominated by X-ray noon. We identify this morphology to likely be associated with the i-family (black label) or moderate injections which often occur after an external perturbation [see G18]. The X-ray morphology is observed to be between our defined categories and agree with Weigt et al. (2020) who observe the northern auroral emissions to be more extended and map to the dayside magnetopause boundary, along the noon-dusk sector using the Vogt et al. (2011, 2015) flux equivalence model. This may therefore suggest that, in this case, the auroral morphology reflects a magnetosphere disturbed in multiple regions and the the emissions likely remain poleward and more concentrated during intervals of compressions. This example was used as a "proof of concept" of compression identification as the location of Juno was near its apojove position. This allows analysis of the magnetospheric response to changing solar wind conditions in the *in situ* data.

Figure 5 shows an example when Juno is near perijove during the Chandra interval on 1 April 2018 (ObsID 18678 - see Table 1 and Figure 1d)), making it difficult to infer the state of the magnetosphere due to the very strong field strength as you approach Jupiter (panels (c) and (d)). Juno made several plasmasheet crossings prior to the CXO interval as shown by the sharp transition in electric spectral density, where the denser plasmasheet blocks the continuum emissions via refraction effects (analogous to the case of magnetopause crossings). Intervals when Juno is inside the plasmasheet are indicated by pink arrows. From this position we have limited ability from the *in situ* measurements to infer the upstream conditions, unlike at apojove when magnetopause boundary crossings can give us snapshots of magnetospheric size and inferred upstream dynamic pressure.

As shown in panels (a) and (b), the Tao et al. (2005) model suggests that there is a series of solar wind compressions during the Juno perijove interval, with maximum pressure of 0.275 nPa. In our analysis we identify that the UV auroral morphology was associated with the X-family, agreeing with the predicted model results, coinciding with the start of the CXO interval. As shown in panel (e), the spectrogram contains a variety of identifiable features including: periodic emissions (up to $\sim$ 1 - 100 kHz as bursts of high electric spectral density); broadband kilometric (bKOM) emissions in highest frequency channels, notably after perijove and the aforementioned continuum emissions, used as indicator of plasmasheet crossings. Therefore it is difficult to disentangle sources associated with the state of the jovian magnetosphere and verify the model results. We do however highlight a region of potential activity, as the dotted black box in Figure 5, in the magnetic field associated with a possible dipolarization of the field when Juno is inside the plasmasheet. A dipolarization occurs when the magnetic field line which Juno travels across changes from a stretched to a more dipolar configuration after a tail reconnection event, producing an anomalous feature in the B_θ component. Such dipolarizations of the field have been found to be associated with injection events found from HST UV observations and can be accompanied by bright dawn storm emissions (Yao et al., 2020). These bright dawn storm emissions have been found to be correlated with a brightening of HXR intensity in the jovian aurora (Wibisono et al., 2021), likely linked to similar regions of electron bremsstrahlung activity (e.g., Branduardi-Raymont et al. (2008). We do note that as the CXO interval was 2-3 jovian rotations after the potential injection event, it is unlikley that the X-ray morphology will reflect this behaviour. However, with the identified X-family (and its links to moderate injections) in the UV emissions the magnetosphere, across many sectors during this interval, is likely to be in a disturbed state.

When comparing Figure 5 to Figure 3, the auroral emissions found in ObsID 18678 exhibited morphology in between our defined categories. Like majority of emissions located in the X-ray polar region with a small portion of the emissions located in the LLE region ($<$ 10%). The small population of X-ray dusk photons indicate that the morphology extended polewards similar to ObsID 20001. Comparing Figures 1c) and (d), the auroral morphology is very similar with the exception of the dawn region. Therefore this distribution of X-ray auroral photons and UV auroral behaviour may be an indicator of a disturbed magnetosphere due to a potential compression event. Identifying such disturbances may be associated with a possible injection event which may precede or follow a compression event as observed by G18. We do note that further in depth analysis of the magnetic field and particle data is needed to confirm this, however the results provided here will likely highlight this observation (and many others associated with possible disturbances) as one of interest for further study.

4 Summary and Discussion

We present X-ray 'auroral structures' mapping to various regions in the magnetosphere linking X-ray auroral morphology to magnetospheric dynamics in the jovian system. Using CXO, HST and Juno data spanning the majority of Juno's main mission (24 May 2016 to 8 September 2019), we are able to compare observed magnetospheric dynamics to UV and X-ray remote sensing data. The results of our auroral distributions can be summarised as follows:

1. The X-ray auroral emissions show two clear categories of auroral morphological distributions: (1) fully polar aurora (2) low latitude emissions.
2. Non-uniformity of auroral distributions suggest there are likely numerous drivers responsible for the X-ray northern auroral emissions or conditions in the magnetosphere that permit the growth of drivers (i.e. EMIC waves) change.
3. Using UV and X-ray morphologies together may be a useful proxy for solar wind conditions (particularly during compressions) to identify magnetospheric disturbances.
4. Visibility (or planetary tilt) has very little effect when observing the auroral photon distributions.
5. X-ray auroral distributions may highlight potential magnetospheric phenomena (i.e., prior injection events) for future study.

We note that only CXO observations which had a HST observation ± 1 day from the Chandra window were considered for this study. For example, ObsID 20002 (6 August 2017; see full catalogue in Weigt, Jackman, et al. (2021)) does not appear in our study, however initial analysis of magnetopause crossings made by Juno suggest that the magnetosphere was compressed during this time using the Joy et al. (2002) model.

From the non-uniformity across the northern auroral distributions (Figure 3) and our visibility modelling of the regions, the lack of emissions we observe in a given region is more likely associated with the switching on/off of drivers. The X-ray noon population dominates the majority of observations suggesting that the likely driver from these emissions lies on the noon magnetopause boundary, as observed by Weigt, Jackman, et al. (2021). Here, X-ray noon coincides with the location of the UV polar and swirl region and therefore linked to a very dynamic region of the dayside magnetosphere. Dayside drivers such as magnetic reconnection would occur more frequently on the noon magnetosphere compared to other regions, especially during periods of high P_{dyn}. In these situations the solar wind is likely to reconnect with the jovian outer magnetosphere either at high latitudes in the cusps (Bunce et al., 2004) or compressions may induce reconnection inside the jovian system (i.e., at multiple smaller sites in the plasmasheet with more drizzle-like reconnection (Guo et al., 2018)). We note that previous analysis of three intervals during compression events (ObsID 20001, 20002, 18678) were found to exhibit very significant quasi-periodic oscillations (QPOs) within a region located in the center of X-ray noon (the averaged hot spot nucleus (AHSNuc)). These QPOs were observed to be between 2- and 4- minutes suggesting very dynamic activity on the noon boundary and timescales linked to magnetic reconnection on the boundary (Weigt, Jackman, et al., 2021). However, Weigt, Jackman, et al. (2021) observed that time QPOs were likely to be spatial dependent and therefore the period and statistical significance changes with where you observe in the aurora. They also stated that any activity may be initiated at the noon magnetopause boundary and be advected along the magnetopause boundary towards the flanks. This may explain the non-uniformity of auroral distributions we discuss here and how wave growth is promoted in other regions of the magnetosphere such as the strong correlations between X-ray emissions and EMIC waves found in the outer dawn and midnight magnetosphere (Yao et al., 2021). Therefore, assuming the auroral emissions are generated from wave activity, the changing auroral morphology may reveal the propensity for wave activity in different components in the jovian magnetosphere.

The peak visibility of each X-ray auroral structure was within our CML threshold throughout the Juno era during with changing sub-Earth latitudes mainly affecting those regions nearest to the pole (i.e., X-ray dusk). We do note however that the changing sub-Earth latitudes will have the greatest effect in the southern auroral region. Therefore future studies will need to develop a new set of X-ray auroral structures to combat this effect. The techniques discussed in this study can be extended to the southern auroral region and will allow detailed exploration and comparisons between both auroral regions (i.e., North-South asymmetry and non-conjugacy observed in the auroral X-ray emissions Branduardi-Raymont et al. (2004); Jackman et al. (2018); Weigt, Jackman, et al. (2021); Mori et al. (2022) and other wavelengths). This has already been shown by Mori et al. (2022) for HXRs, where non-thermal bremsstrahlung X-rays were $\sim$ twice as bright in the southern auroral region than the North, consistent with more persistent and stronger electron currents than those observed in the North (Kotsiaros et al., 2019).

In order to fully categorise the jovian X-ray auroral emissions and the extent of the solar wind influence at both poles, current X-ray technology needs to be expanded upon. Future potential missions such as Lynx (Falcone et al., 2019) and Line Emission Mapper (LEM; Kraft et al. (2022)) will allow us to explore in detail the various drivers generating X-ray emissions in the jovian magnetosphere. Utilising the enhanced spectral resolution i.e., 1-2 eV spectral resolution in the 0.2-2 keV range for LEM) and greater effective area at lower energies, we will be able to delve into the softer X-ray spectrum and evaluate the ion populations dominating various X-ray processes (e.g., charge exchange) and eventually inclduing the southern hemisphere. Coupling these remote sensing instruments with data from an *in situ* X-ray probe (Dunn et al., 2023) will be the key to fully understanding the magnetospheric drivers responsible for the jovian auroral X-ray emissions.

Data Availability Statement

This research has made use of data obtained from the *Chandra Data Archive* and *Chandra Source Catalogue* (`https://cda.harvard.edu/chaser/`); Juno Waves and MAG from the *the NASA Planetary Data System* and solar wind data obtained via AMDA (`http://amda.cdpp.eu/`). Waves survey data are at `https://doi.org/10.17189/1520498` . The catalogue of Chandra data required to reproduce the results shown in this study are stored in the Zenodo repository at `http://doi.org/10.5281/zenodo.4275744.`

Acknowledgments

DMW is supported by the Science and Technology Facilities Council (STFC) studentship ST/S505705/1 and long term attachment grant to work at the Dublin Institute for Advanced Studies (DIAS). DMW's work at DIAS is funded by European Union's Horizon 2020 research and innovation programme under grant agreement No. 952439 and project number AO 2-1927/22/NL/GLC/ov as part of the ESA OSIP Nanosats for Spaceweather Campaign. DMW's work at Trinity College Dublin is supported by Air Force Office of

Scientific Research award FA9550-19-1-7010. DMP is supported by a LUFST studentship. SVB is supported by STFC projects ST/M005534/1 and ST/V000748/1. CMJ, CKL and SCMcE work at DIAS is supported by the Science Foundation Ireland (SFI) Grant 18/FRL/6199. WRD was supported by Ernest Rutherford Fellowship: ST/W003449/1. CT acknowledges support by JSPS KAKENHI 20KK0074. The research at the University of Iowa is supported by NASA through Contract 699041X with Southwest Research Institute.

References

Badman, S. V., Branduardi-Raymont, G., Galand, M., Hess, S. L. G., Krupp, N., Lamy, L., … Tao, C. (2015). Auroral Processes at the Giant Planets: Energy Deposition, Emission Mechanisms, Morphology and Spectra. *Space Science Reviews*, *187*(1-4), 99–179. Retrieved from http://dx.doi.org/10.1007/s11214-014-0042-xhttp://link.springer.com/10.1007/s11214-014-0042-x doi: 10.1007/s11214-014-0042-x

Bolton, S. J., Lunine, J., Stevenson, D., Connerney, J. E. P., Levin, S., Owen, T. C., … Thorpe, R. (2017). The Juno Mission. *Space Science Reviews*, *213*(1-4), 5–37. Retrieved from http://dx.doi.org/10.1007/s11214-017-0429-6http://link.springer.com/10.1007/s11214-017-0429-6 doi: 10.1007/s11214-017-0429-6

Bonfond, B., Saur, J., Grodent, D., Badman, S. V., Bisikalo, D., Shematovich, V., … Radioti, A. (2017). The tails of the satellite auroral footprints at Jupiter. *Journal of Geophysical Research (Space Physics)*, *122*(8), 7985-7996. doi: 10.1002/2017JA024370

Bonfond, B., Yao, Z. H., Gladstone, G. R., Grodent, D., Gérard, J., Matar, J., … Bolton, S. J. (2021). Are Dawn Storms Jupiter's Auroral Substorms? *AGU Advances*, *2*(1), 1–14. doi: 10.1029/2020av000275

Branduardi-Raymont, G., Elsner, R. F., Galand, M., Grodent, D., Cravens, T. E., Ford, P., … Waite, J. H. (2008). Spectral morphology of the X-ray emission from Jupiter's aurorae. *Journal of Geophysical Research: Space Physics*, *113*(2), 1–11. doi: 10.1029/2007JA012600

Branduardi-Raymont, G., Elsner, R. F., Gladstone, G. R., Ramsay, G., Rodriguez, P., Soria, R., & Waite, J. H. (2004). First observation of Jupiter by XMM-Newton. *Astronomy*, *337*(1149), 331–337. doi: 10.1051/0004-6361

Bunce, E. J., Cowley, S. W., & Yeoman, T. K. (2004). Jovian cusp processes: Implications for the polar aurora. *Journal of Geophysical Research: Space Physics*, *109*(A9), 1–26. doi: 10.1029/2003JA010280

Connerney, J. E. P., Benn, M., Bjarno, J. B., Denver, T., Espley, J., Jorgensen, J. L., … Smith, E. J. (2017). The Juno Magnetic Field Investigation. *Space Science Reviews*, *213*(1-4), 39–138. Retrieved from http://dx.doi.org/10.1007/s11214-017-0334-z doi: 10.1007/s11214-017-0334-z

Dumont, M., Grodent, D., Radioti, A., Bonfond, B., & Gérard, J. (2014). Jupiter's equatorward auroral features: Possible signatures of magnetospheric injections. *Journal of Geophysical Research: Space Physics*, *119*(12), A07000. Retrieved from http://doi.wiley.com/10.1029/2006JA011892https://onlinelibrary.wiley.com/doi/abs/10.1002/2014JA020527 doi: 10.1002/2014JA020527

Dumont, M., Grodent, D., Radioti, A., Bonfond, B., Roussos, E., & Paranicas, C. (2018). Evolution of the Auroral Signatures of Jupiter's Magnetospheric Injections. *Journal of Geophysical Research: Space Physics*, *123*(2015), 1–13. Retrieved from http://doi.wiley.com/10.1029/2018JA025708 doi: 10.1029/2018JA025708

Dunn, W., Berland, G., Roussos, E., Clark, G., Kollmann, P., Turner, D., … Kraft, R. P. (2023, March). Exploring Fundamental Particle Acceleration and Loss Processes in Heliophysics through an Orbiting X-ray Instrument in the Jovian

System. *arXiv e-prints*, arXiv:2303.02161. doi: 10.48550/arXiv.2303.02161

Dunn, W. R. (2022). X-Ray Emissions from the Jovian System. In *Handbook of x-ray and gamma-ray astrophysics. edited by cosimo bambi and andrea santangelo* (p. 110). doi: 10.1007/978-981-16-4544-0_73-1

Dunn, W. R., Branduardi-Raymont, G., Elsner, R. F., Vogt, M. F., Lamy, L., Ford, P. G., ... Jasinski, J. M. (2016). The impact of an ICME on the Jovian X-ray aurora. *Journal of Geophysical Research A: Space Physics*, *121*(3), 2274–2307. doi: 10.1002/2015JA021888

Dunn, W. R., Branduardi-Raymont, G., Ray, L. C., Jackman, C. M., Kraft, R. P., Elsner, R. F., ... Coates, A. J. (2017). The independent pulsations of Jupiter's northern and southern X-ray auroras. *Nature Astronomy*, *1*(11), 758–764. Retrieved from `http://dx.doi.org/10.1038/s41550-017-0262-6` doi: 10.1038/s41550-017-0262-6

Dunn, W. R., Branduardi-Raymont, G., Carter-Cortez, V., Campbell, A., Elsner, R., Ness, J.-U., ... Achilleos, N. (2020). Jupiter's X-ray Emission During the 2007 Solar Minimum. *Journal of Geophysical Research: Space Physics*, *125*(6), e2019JA027219. Retrieved from `https://onlinelibrary.wiley.com/doi/abs/10.1029/2019JA027219` doi: 10.1029/2019JA027219

Dunn, W. R., Gray, R., Wibisono, A. D., Lamy, L., Louis, C., Badman, S. V., ... Kraft, R. (2020). Comparisons Between Jupiter's X-ray, UV and Radio Emissions and In-Situ Solar Wind Measurements During 2007. *Journal of Geophysical Research: Space Physics*, *125*(6), e2019JA027222. Retrieved from `https://onlinelibrary.wiley.com/doi/abs/10.1029/2019JA027222` doi: 10.1029/2019JA027222

Dunn, W. R., Weigt, D. M., Grodent, D., Yao, Z. H., May, D., Feigelman, K., ... Ray, L. C. (2022). Jupiter's X-ray and UV Dark Polar Region. *Geophysical Research Letters*, *4*. Retrieved from `https://onlinelibrary.wiley.com/doi/10.1029/2021GL097390` doi: 10.1029/2021GL097390

Elsner, R. F., Lugaz, N., Waite, J. H., Cravens, T. E., Gladstone, G. R., Ford, P., ... Majeed, T. (2005). Simultaneous Chandra X ray Hubble Space Telescope ultraviolet, and Ulysses radio observations of Jupiter's aurora. *Journal of Geophysical Research: Space Physics*, *110*(A1), 1–16. doi: 10.1029/2004JA010717

Falcone, A. D., Kraft, R. P., Bautz, M. W., Gaskin, J. A., Mulqueen, J. A., & Swartz, D. A. (2019). Overview of the high-definition x-ray imager instrument on the Lynx x-ray surveyor. *Journal of Astronomical Telescopes, Instruments, and Systems*, *5*(2). doi: 10.1117/1.JATIS.5.2.021019

Gerard, J. C., Grodent, D., Prange, R., Waite, J. H., Gladstone, G. R., Dols, V., ... Franke, K. A. (1994). A Remarkable Auroral Event on Jupiter Observed in the Ultraviolet with the Hubble Space Telescope. *Science*, *266*(5191), 1675-1678. doi: 10.1126/science.266.5191.1675

Gray, R. L., Badman, S. V., Bonfond, B., Kimura, T., Misawa, H., Nichols, J. D., ... Ray, L. C. (2016). Auroral evidence of radial transport at Jupiter during January 2014. *Journal of Geophysical Research: Space Physics*, *121*(10), 9972–9984. Retrieved from `https://onlinelibrary.wiley.com/doi/abs/10.1002/2016JA023007` doi: 10.1002/2016JA023007

Greathouse, T., Gladstone, R., Versteeg, M., Hue, V., Kammer, J., Giles, R., ... Vogt, M. F. (2021). Local Time Dependence of Jupiter's Polar Auroral Emissions Observed by Juno UVS. *Journal of Geophysical Research: Planets*, *126*(12), 1–13. doi: 10.1029/2021JE006954

Grodent, D. (2015). A Brief Review of Ultraviolet Auroral Emissions on Giant Planets. *Space Science Reviews*, *187*(1-4), 23–50. Retrieved from `http://dx.doi.org/10.1007/s11214-014-0052-8` doi: 10.1007/s11214-014-0052-8

Grodent, D., Bonfond, B., Yao, Z., Gérard, J. C., Radioti, A., Dumont, M., ... Valek, P. (2018). Jupiter's Aurora Observed With HST During Juno Orbits 3 to 7. *Journal of Geophysical Research: Space Physics*, *123*(5), 3299–3319. doi:

10.1002/2017JA025046
Grodent, D., Clarke, J. T., Kim, J., Waite, J. H., & Cowley, S. W. H. (2003). Jupiter's main auroral oval observed with HST-STIS. *Journal of Geophysical Research (Space Physics)*, *108*(A11), 1389. doi: 10.1029/2003JA009921
Grodent, D., Clarke, J. T., Waite, J. H., Cowley, S. W., Gérard, J. C., & Kim, J. (2003). Jupiter's polar auroral emissions. *Journal of Geophysical Research: Space Physics*, *108*(A10), 1–9. doi: 10.1029/2003JA010017
Guo, R. L., Yao, Z. H., Sergis, N., Wei, Y., Mitchell, D., Roussos, E., … Wan, W. X. (2018). Reconnection Acceleration in Saturn's Dayside Magnetodisk: A Multicase Study with Cassini . *The Astrophysical Journal*, *868*(2), L23. Retrieved from http://dx.doi.org/10.3847/2041-8213/aaedab doi: 10.3847/2041-8213/aaedab
Gurnett, D. A., & Scarf, F. L. (1983). Plasma waves in the jovian magnetosphere. In A. J. Dessler (Ed.), *Physics of the jovian magnetosphere* (p. 285–316). Cambridge University Press. doi: 10.1017/CBO9780511564574.010
Hospodarsky, G. B., Kurth, W. S., Bolton, S. J., Allegrini, F., Clark, G. B., Connerney, J. E., … Valek, P. W. (2017). Jovian bow shock and magnetopause encounters by the Juno spacecraft. *Geophysical Research Letters*, *44*(10), 4506–4512. doi: 10.1002/2017GL073177
Houston, S. J., Cravens, T. E., Schultz, D. R., Gharibnejad, H., Dunn, W. R., Haggerty, D. K., … Ozak, N. (2020). Jovian Auroral Ion Precipitation: X-Ray Production From Oxygen and Sulfur Precipitation. *Journal of Geophysical Research: Space Physics*, *125*(2), 2019JA027007. Retrieved from https://onlinelibrary.wiley.com/doi/10.1029/2019JA027007 doi: 10.1029/2019JA027007
Jackman, C. M., & Arridge, C. S. (2011). Solar Cycle Effects on the Dynamics of Jupiter's and Saturn's Magnetospheres. *Solar Physics*, *274*(1-2), 481–502. doi: 10.1007/s11207-011-9748-z
Jackman, C. M., Knigge, C., Altamirano, D., Gladstone, R., Dunn, W., Elsner, R., … Ford, P. (2018). Assessing Quasi-Periodicities in Jovian X-Ray Emissions: Techniques and Heritage Survey. *Journal of Geophysical Research: Space Physics*, *123*(11), 9204–9221. doi: 10.1029/2018JA025490
Joy, S. P., Kivelson, M. G., Walker, R. J., Khurana, K. K., Russell, C. T., & Ogino, T. (2002). Probabilistic models of the Jovian magnetopause and bow shock locations. *Journal of Geophysical Research: Space Physics*, *107*(A10), 1–17. doi: 10.1029/2001JA009146
Kimura, T., Nichols, J. D., Gray, R. L., Tao, C., Murakami, G., Yamazaki, A., … Fujimoto, M. (2017). Transient brightening of Jupiter's aurora observed by the Hisaki satellite and Hubble Space Telescope during approach phase of the Juno spacecraft. *Geophysical Research Letters*, *44*(10), 4523–4531. doi: 10.1002/2017GL072912
Kotsiaros, S., Connerney, J. E., Clark, G., Allegrini, F., Gladstone, G. R., Kurth, W. S., … Levin, S. M. (2019). Birkeland currents in Jupiter's magnetosphere observed by the polar-orbiting Juno spacecraft. *Nature Astronomy*, *3*(10), 904–909. Retrieved from http://dx.doi.org/10.1038/s41550-019-0819-7 doi: 10.1038/s41550-019-0819-7
Kraft, R., Markevitch, M., Kilbourne, C., Adams, J. S., Akamatsu, H., Ayromlou, M., … ZuHone, J. (2022, November). Line Emission Mapper (LEM): Probing the physics of cosmic ecosystems. *arXiv e-prints*, arXiv:2211.09827. doi: 10.48550/arXiv.2211.09827
Kurth, W. S., Hospodarsky, G. B., Kirchner, D. L., Mokrzycki, B. T., Averkamp, T. F., Robison, W. T., … Zarka, P. (2017). The Juno Waves Investigation. *Space Science Reviews*, *213*(1-4), 347–392. Retrieved from http://dx.doi.org/10.1007/s11214-017-0396-y doi: 10.1007/s11214-017-0396-y
Louarn, P., Paranicas, C. P., & Kurth, W. S. (2014). Global magnetodisk distur-

bances and energetic particle injections at Jupiter. *Journal of Geophysical Research: Space Physics*, *119*(6), 4495-4511. doi: 10.1002/2014JA019846

McComas, D. J., Szalay, J. R., Allegrini, F., Bagenal, F., Connerney, J., Ebert, R. W., ... Bolton, S. (2017). Plasma environment at the dawn flank of Jupiter's magnetosphere: Juno arrives at Jupiter. *Geophysical Research Letters*, *44*(10), 4432–4438. doi: 10.1002/2017GL072831

McEntee, S. C., Jackman, C. M., Weigt, D. M., Dunn, W. R., Kashyap, V., Kraft, R., ... Gallagher, P. T. (2022). Comparing jupiter's equatorial x-ray emissions with solar x-ray flux over 19 years of the chandra mission. *Journal of Geophysical Research: Space Physics*, *127*. Retrieved from `https://onlinelibrary.wiley.com/doi/10.1029/2022JA030971` doi: 10.1029/2022JA030971

Mori, K., Hailey, C., Bridges, G., Mandel, S., Garvin, A., Grefenstette, B., ... Ray, L. (2022). Observation and origin of non-thermal hard X-rays from Jupiter. *Nature Astronomy*. Retrieved from `https://www.nature.com/articles/s41550-021-01594-8` doi: 10.1038/s41550-021-01594-8

Nichols, J. D., Badman, S. V., Bagenal, F., Bolton, S. J., Bonfond, B., Bunce, E. J., ... Yoshikawa, I. (2017). Response of Jupiter's auroras to conditions in the interplanetary medium as measured by the Hubble Space Telescope and Juno. *Geophysical Research Letters*, *44*(15), 7643–7652. Retrieved from `http://doi.wiley.com/10.1002/2017GL073029` doi: 10.1002/2017GL073029

Nichols, J. D., Clarke, J. T., Gérard, J. C., Grodent, D., & Hansen, K. C. (2009). Variation of different components of jupiter's auroral emission. *Journal of Geophysical Research: Space Physics*, *114*(6), 1–18. doi: 10.1029/2009JA014051

Pallier, L., & Prangé, R. (2001). More about the structure of the high latitude Jovian aurorae. *Planetary and Space Science*, *49*(10-11), 1159-1173. doi: 10.1016/S0032-0633(01)00023-X

Swithenbank-Harris, B. G., Nichols, J. D., & Bunce, E. J. (2019). Jupiter's Dark Polar Region as Observed by the Hubble Space Telescope During the Juno Approach Phase. *Journal of Geophysical Research: Space Physics*, *124*(11), 9094–9105. doi: 10.1029/2019JA027306

Tao, C., Kataoka, R., Fukunishi, H., Takahashi, Y., & Yokoyama, T. (2005). Magnetic field variations in the Jovian magnetotail induced by solar wind dynamic pressure enhancements. *Journal of Geophysical Research: Space Physics*, *110*(A11), 1–9. doi: 10.1029/2004JA010959

Vasyliūnas, V. M. (1983). Plasma distribution and flow. In A. J. Dessler (Ed.), *Physics of the jovian magnetosphere* (pp. 395–453). Cambridge: Cambridge University Press. Retrieved from `https://www.cambridge.org/core/product/identifier/CBO9780511564574A082/type/book{\_}part` doi: 10.1017/CBO9780511564574.013

Vogt, M. F., Bunce, E. J., Kivelson, M. G., Khurana, K. K., Walker, R. J., Radioti, A., ... Grodent, D. (2015). Magnetosphere-ionosphere mapping at Jupiter: Quantifying the effects of using different internal field models. *Journal of Geophysical Research: Space Physics*, *120*(4), 2584–2599. doi: 10.1002/2014JA020729

Vogt, M. F., Kivelson, M. G., Khurana, K. K., Walker, R. J., Bonfond, B., Grodent, D., & Radioti, A. (2011). Improved mapping of Jupiter's auroral features to magnetospheric sources. *Journal of Geophysical Research: Space Physics*, *116*(3). doi: 10.1029/2010JA016148

Weigt, D. M., Dunn, W. R., Jackman, C. M., Kraft, R., Branduardi-Raymont, G., Nichols, J. D., ... Gladstone, G. R. (2021). Searching for Saturn's X-rays during a rare Jupiter Magnetotail crossing using Chandra. *Monthly Notices of the Royal Astronomical Society*, *506*(1), 298–305. Retrieved from `https://academic.oup.com/mnras/article/506/1/298/6298248` doi:

10.1093/mnras/stab1680
Weigt, D. M., Gladstone, G. R., McEntee, S. C., Dunn, W. R., Kashyap, V. L., Jackman, C. M., ... Branduardi-Raymont, G. (2022). *Chandra_x-ray_data_processing_pipeline version 1.0.2 (v1.0.2) [computer software].* Zenodo. doi: 10.5281/ZENODO.7380282

Weigt, D. M., Jackman, C. M., Dunn, W. R., Gladstone, G. R., Vogt, M. F., Wibisono, A. D., ... Kraft, R. P. (2020). Chandra Observations of Jupiter's X-ray Auroral Emission During Juno Apojove 2017. *Journal of Geophysical Research: Planets*, *125*(4), e2019JE006262. Retrieved from `https://onlinelibrary.wiley.com/doi/abs/10.1029/2019JE006262` doi: 10.1029/2019JE006262

Weigt, D. M., Jackman, C. M., Vogt, M. F., Manners, H., Dunn, W. R., Gladstone, G. R., ... McEntee, S. C. (2021). Characteristics of Jupiter's X-Ray Auroral Hot Spot Emissions Using Chandra. *Journal of Geophysical Research: Space Physics*, *126*(9). Retrieved from `https://onlinelibrary.wiley.com/doi/10.1029/2021JA029243` doi: 10.1029/2021JA029243

Weisskopf, M. C., Tananbaum, H. D., Van Speybroeck, L. P., & O'Dell, S. L. (2000). Chandra X-ray Observatory (CXO): overview. *X-Ray Optics, Instruments, and Missions III*, *4012*(July 2000), 2–16. doi: 10.1117/12.391545

Wibisono, A. D., Branduardi-Raymont, G., Dunn, W. R., Kimura, T., Coates, A. J., Grodent, D., ... Haythornthwaite, R. P. (2021). Jupiter's X-ray aurora during UV dawn storms and injections as observed by XMM-Newton, Hubble, and Hisaki. *Monthly Notices of the Royal Astronomical Society*, *507*(1), 1216-1228. doi: 10.1093/mnras/stab2218

Yao, Z., Bonfond, B., Clark, G., Grodent, D., Dunn, W., Vogt, M., ... Bolton, S. (2020). Reconnection- and Dipolarization-Driven Auroral Dawn Storms and Injections. *Journal of Geophysical Research: Space Physics*, *125*(8). doi: 10.1029/2019JA027663

Yao, Z., Dunn, W., Woodfield, E., Clark, G., Mauk, B., Ebert, R., ... Bolton, S. (2021). Revealing the source of jupiter's x-ray auroral flares. *Science Advances*, *7*(28), eabf0851. Retrieved from `https://www.science.org/doi/abs/10.1126/sciadv.abf0851` doi: 10.1126/sciadv.abf0851

Yoshioka, K., Murakami, G., Yamazaki, A., Tsuchiya, F., Kagitani, M., Sakanoi, T., ... Yoshikawa, I. (2013). The extreme ultraviolet spectroscope for planetary science, EXCEED. *Planetary and Space Science*, *85*, 250-260. doi: 10.1016/j.pss.2013.06.021

Figure 1.

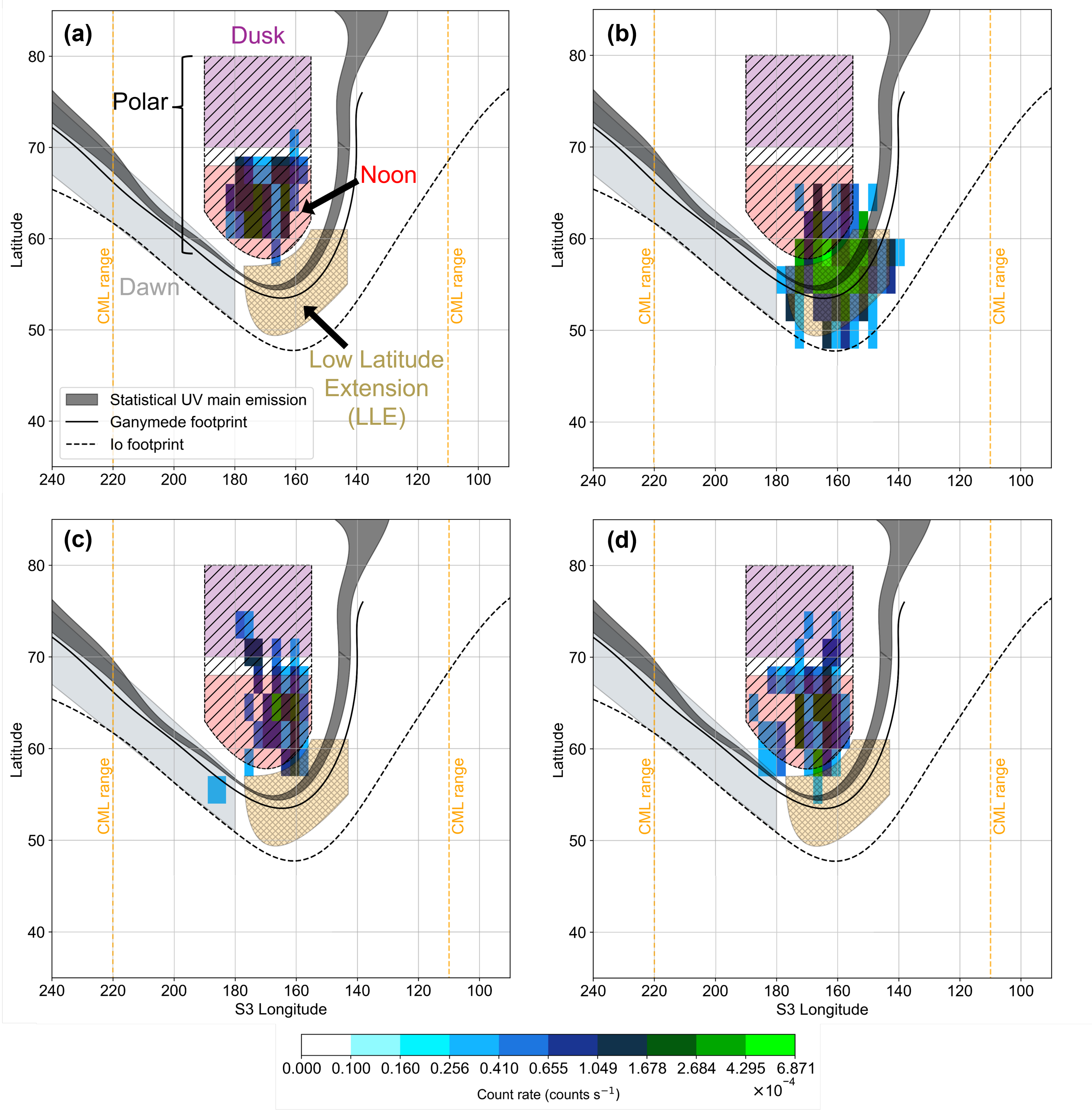

(a)
(b)
(c)
(d)
Dusk
Polar
Noon
Dawn
Low Latitude Extension (LLE)
CML range
Statistical UV main emission
Ganymede footprint
Io footprint
Latitude
S3 Longitude
240 220 200 180 160 140 120 100
40 50 60 70 80
0.000 0.100 0.160 0.256 0.410 0.655 1.049 1.678 2.684 4.295 6.871
$\times 10^{-4}$
Count rate (counts s^{-1})

Figure 2.

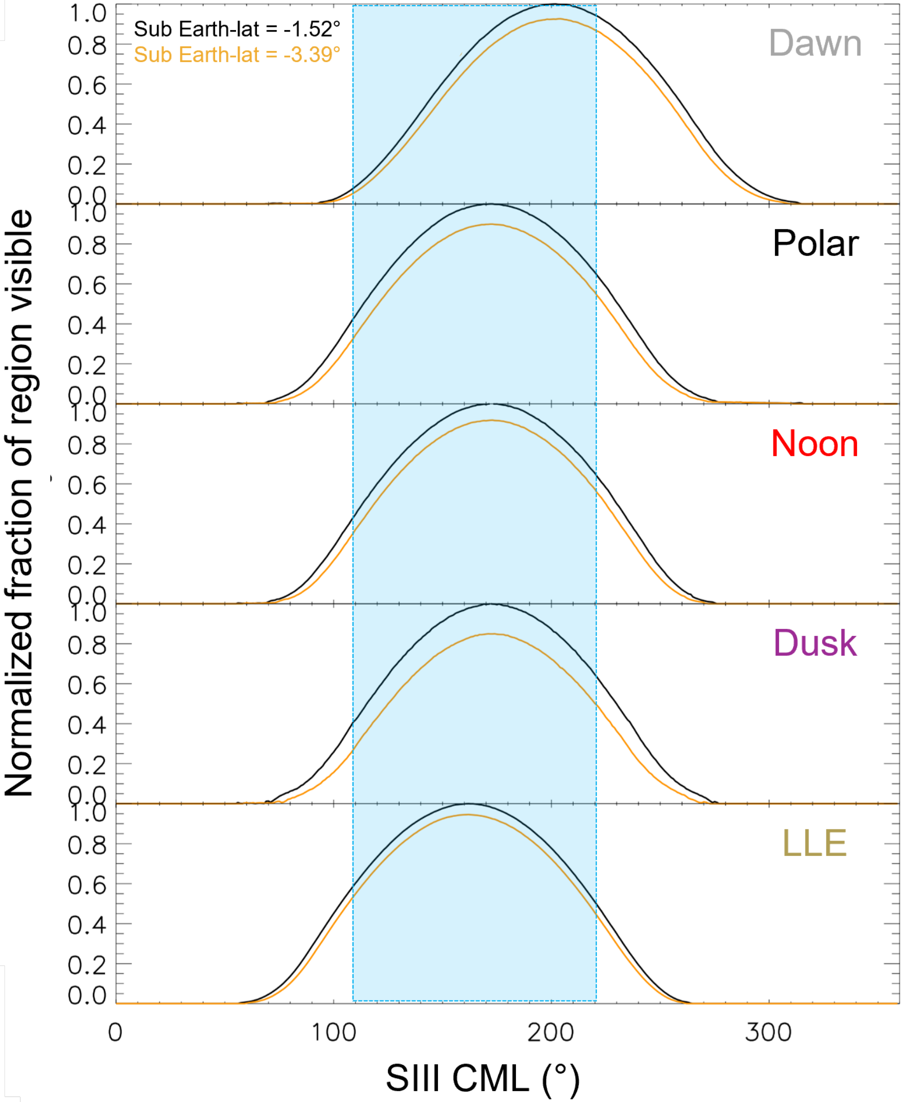
Sub Earth-lat = -1.52°
Sub Earth-lat = -3.39°
Dawn
Polar
Noon
Dusk
LLE
Normalized fraction of region visible
SIII CML (°)
0
100
200
300
0.0
0.2
0.4
0.6
0.8
1.0

Figure 3.

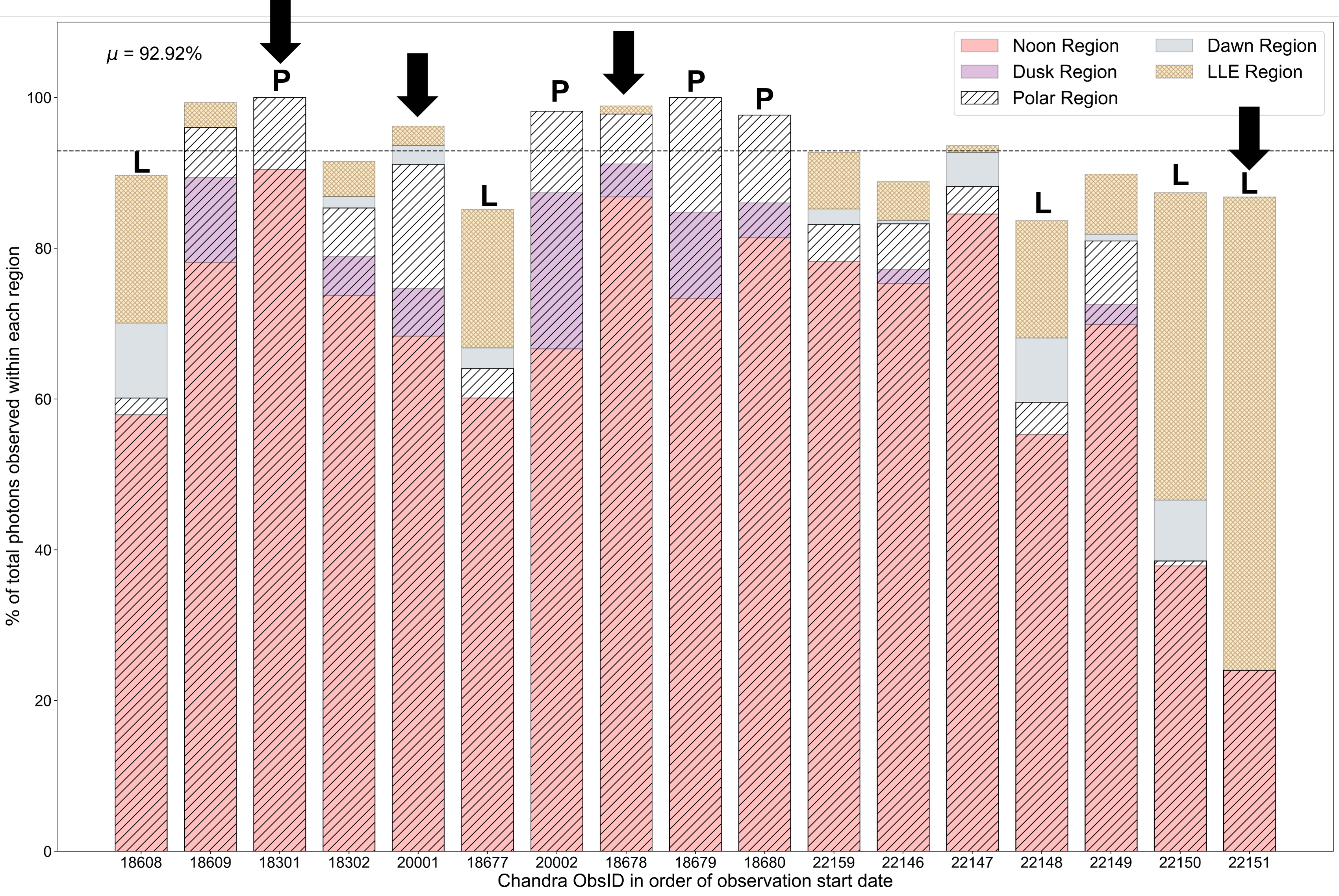

μ = 92.92%
Noon Region
Dawn Region
Dusk Region
LLE Region
Polar Region
% of total photons observed within each region
Chandra ObsID in order of observation start date
0
20
40
60
80
100
18608
18609
18301
18302
20001
18677
20002
18678
18679
18680
22159
22146
22147
22148
22149
22150
22151
L
P

Figure 4.

(a)
- G18 prediction
- This study
Solar wind dynamic pressure
P_{dyn} (nPa)
HST interval
CXO interval
(b)
JSE angle
Jupiter-Sun-Earth angle (°)
(c)
Magnetosheath
Magnetosphere
Magnetosheath
Magnetosphere
B_r
B_θ
B_ϕ
Value of $B_{r,\theta,\phi}$ (nT)
(d)
|B| (nT)
(e)
Freq. (Hz)
Electric Spectral Density ($V^2/m^2/Hz$)
Distance (R_J)
Lon_{III}(°)
Lat (°)
$MLat_{JRM09}$(°)
MLT (hours)
2017-06-16 (167) 17:55 to 2017-06-20 (171) 17:56

Figure 5.

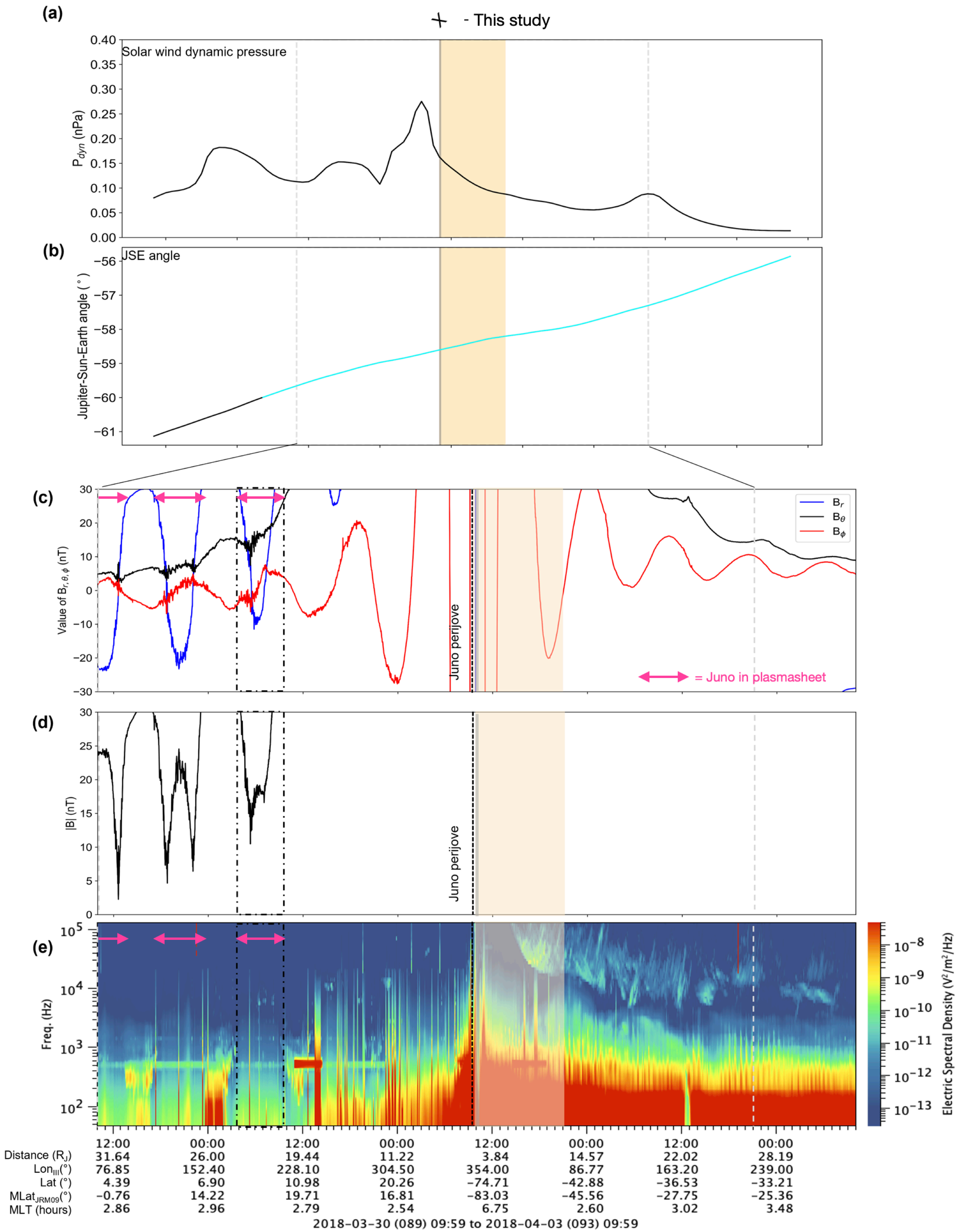

(a)
- This study
Solar wind dynamic pressure
P_{dyn} (nPa)
(b)
JSE angle
Jupiter-Sun-Earth angle (°)
(c)
B_r
B_θ
B_ϕ
Value of $B_{r,\theta,\phi}$ (nT)
Juno perijove
= Juno in plasmasheet
(d)
|B| (nT)
Juno perijove
(e)
Freq. (Hz)
Electric Spectral Density ($V^2/m^2/Hz$)
12:00 00:00 12:00 00:00 12:00 00:00 12:00 00:00
Distance (R_J) 31.64 26.00 19.44 11.22 3.84 14.57 22.02 28.19
Lon_{III}(°) 76.85 152.40 228.10 304.50 354.00 86.77 163.20 239.00
Lat (°) 4.39 6.90 10.98 20.26 -74.71 -42.88 -36.53 -33.21
$MLat_{JRM09}$(°) -0.76 14.22 19.71 16.81 -83.03 -45.56 -27.75 -25.36
MLT (hours) 2.86 2.96 2.79 2.54 6.75 2.60 3.02 3.48
2018-03-30 (089) 09:59 to 2018-04-03 (093) 09:59

Identifying the variety of jovian X-ray auroral structures: tying the morphology of X-ray emissions to associated magnetospheric dynamics

D. M. Weigt[1,2,3], C. M. Jackman[2], D. Moral-Pombo[4], S. V. Badman[4], C. K. Louis[2], W. R. Dunn[5], S. C. McEntee[2,3], G. Branduardi-Raymont[6], D. Grodent[7], M. F. Vogt[8], C. Tao[9], G. R. Gladstone[10], R. P. Kraft[11], W. S. Kurth[12], J. E. P. Connerney[13,14]

[1]School of Physics and Astronomy, University of Southampton, Southampton, UK
[2]School of Cosmic Physics, DIAS Dunsink Observatory, Dublin Institute for Advanced Studies, Dublin, Ireland
[3]School of Physics, Trinity College Dublin, Dublin, Ireland
[4]Department of Physics, Lancaster University, Bailrigg, Lancaster, UK
[5]Department of Physics and Astronomy, University College London, London, UK
[6]Mullard Space Science Laboratory, University College London, Dorking, UK
[7]Laboratory for Planetary and Atmospheric Physics, Space Science, Technologies and Astrophysical Research Institute, University of Liège, Liège, Belgium
[8]Center for Space Physics, Boston University, Boston, MA, USA
[9]National Institute of Information and Communications Technology, Tokyo, Japan
[10]Southwest Research Institute, San Antonio, TX, USA
[11]Harvard-Smithsonian Center for Astrophysics, Smithsonian Astrophysical Observatory, Cambridge, MA, USA
[12]Department of Physics and Astronomy, University of Iowa, Iowa City, IA, USA
[13]Space Research Corporation, Annapolis, MD, 21403, USA
[14]NASA Goddard Space Flight Center, Greenbelt, MD, 20771, USA

Key Points:

- We present the morphology of new 'X-ray auroral structures', observed on Jupiter via Chandra's high spatial resolution camera.
- Our visibility modelling of these regions show that planetary tilt has very little effect on non-uniform auroral photon distributions.
- We show that combination of X-ray and UV 'auroral families' may be a useful proxy to determine the magnetospheric conditions at Jupiter.

Corresponding author: Dale Michael Weigt, `weigt@cp.dias.ie`

Abstract

We define the spatial clustering of X-rays within Jupiter's northern auroral regions by classifying their distributions into 'X-ray auroral structures'. Using data from Chandra during Juno's main mission observations (24 May 2016 – 8 September 2019), we define five X-ray structures based on their ionospheric location and calculate the distribution of auroral photons. The morphology and ionospheric location of these structures allow us to explore the possibility of numerous X-ray auroral magnetospheric drivers. We compare these distributions to Hubble Space Telescope (HST)and Juno (Waves and MAG) data, and a 1D solar wind propagation model to infer the state of Jupiter's magnetosphere. Our results suggest that the five sub-classes of 'X-ray structures' fall under two broad morphologies: fully polar and low latitude emissions. Visibility modelling of each structure suggests the non-uniformity of the photon distributions across the Chandra intervals are likely associated with the switching on/off of magnetospheric drivers as opposed to geometrical effects. The combination of ultraviolet (UV) and X-ray morphological structures is a powerful tool to elucidate the behaviour of both electrons and ions and their link to solar wind/magnetospheric conditions in the absence of an upstream solar monitor.

Plain Language Summary

The mechanism that allows precipitation of ions into Jupiter's atmosphere and generate pulsed X-ray auroral emissions is still under debate today. Previous studies have linked this driver to possible activity in Jupiter's outer magnetosphere (the interface between the solar wind and Jupiter) and have observed the emissions to exhibit variable behaviour. More recent studies have suggested a wide range of physical phenomena causing these emissions. Here we explore this idea in more detail by introducing five 'X-ray auroral structures' that map to different regions in the jovian system. Using data from the Chandra X-ray Observatory during Juno's main mission allows us to calculate the distribution of X-rays from Jupiter's northern auroral region. We compare our X-ray results with the ultraviolet emissions ('UV auroral families') observed from simultaneous Hubble Space Telescope (HST) data and infer the conditions at Jupiter using models and Juno observations. These 'X-ray structures' provide us with many ways to observe variable behaviour and provide a possible tool to monitor the solar wind conditions, when used in tandem with the HST 'UV auroral families'.

1 Introduction

The jovian auroral emissions are very complex and are highly variable in their morphological and temporal behaviour across multiple wavelengths [see full review by Badman et al. (2015) and references therein for more details]. The X-ray emissions remain the most elusive of the observable aurora with many recent studies trying to understand the highly sophisticated magnetospheric driver(s) capable of energising the ions to MeV energies that allow charge stripping and charge exchange to take place in the jovian ionosphere for soft X-ray (SXR: < 1 keV) production (e.g., Dunn, Branduardi-Raymont, et al. (2020); Dunn, Gray, et al. (2020); Houston et al. (2020)). The SXRs are produced from precipitating MeV ions originating in the outer magnetosphere and are sometimes observed to be coincident with flaring ultraviolet (UV) emissions within the UV active polar region as observed by Dunn et al. (2022) [herein refereed to as D22]. The auroral hard X-rays (HXR: > 2 keV) result from bremsstrahlung emissions from precipitating electrons, with the auroral emissions observed to sometimes coincide with the UV main emission (e.g., Branduardi-Raymont et al. (2008); Dunn et al. (2016)). This suggests that the precipitating electrons responsible for the HXR and UV main emission auroral emissions are likely to originate in the same region of the middle magnetosphere. Recent and ongoing studies are investigating how the X-rays are connected to other auroral emissions in the EM spectrum via plasma waves such as electromagnetic ion cyclotron (EMIC) waves associated with precipitating ions, which are shown to be strongly correlated with X-ray pulsations (e.g., Yao et al. (2021)). Other studies have looked at how the HXR are correlated with the more intense UV auroral emissions (Wibisono et al., 2021), such as dawn storms - major enhancements of the UV main emission along the dawn arc with a broadening in latitude (Bonfond et al., 2021; Yao et al., 2020).

Previous studies analysing the jovian UV aurorae from the Hubble Space Telescope (HST) have isolated various regions within the auroral emissions to explore the temporal and morphological variation across them. Nichols et al. (2009) used data from two 2007 Hubble Space Telescope (HST) campaigns to identify three northern UV auroral components: (1) the main oval (main emission), (2) low-latitude and (3) high-latitude auroral emissions. They calculated the auroral power, via analysis of the observations and visibility modelling of each region, and predicted solar wind conditions propagated from Earth to investigate the most likely cause of variation. Their results showed that generally the auroral power from the polar regions (low- and high- latitude auroral emissions) were uncorrelated with that of the main emission unless a dawn storm or enhancements due to a magnetospheric compression occurred. This may be a result of the polar emissions, in particular the swirl region observed to contain patchy and turbulent auroral emissions at the centre of the UV polar auroral emissions, having a strong local time dependence (Greathouse et al., 2021).

Nichols et al. (2017) followed up their previous study by segmenting the northern auroral region further, focusing on four regions of interest. These regions were applied to a larger HST dataset (around 47 orbits in total), covering May to July 2016 during Juno's (Bolton et al., 2017) final approach to Jupiter and its orbit insertion in the dawn flank of Jupiter's magnetosphere. By comparing the Juno *in situ* interplanetary data (McComas et al., 2017) and the HST UV auroral images they observed the intensity of the the main emission (at System III (SIII) longitudes $> 170°$) to increase for 1 - 3 days following compression events identified by Juno, with emissions on the polar dusk side to also brighten during these times and during shallow rarefactions of the solar wind. Auroral emissions equatorward of the main emission (at SIII longitudes $< 190°$) brightened ~ 10 days following enhanced Io plasma torus emissions observed from the EXtreme ultraviolet spetrosCope for ExosphEric Dynamics (EXCEED) on board Hisaki (Yoshioka et al., 2013). The noon active region did not show any clear correlation between intensity and interplanetary conditions, although the morphology was observed to change between periods of rarefactions and compressions. The variability of these emissions across the specific regions highlights how the auroral and magnetospheric dynamics change across different local times.

More recently, Grodent et al. (2018) [herein referred to as G18] characterised 118 HST images during Juno orbits 3 to 7 (from 30 November 2016 up to and including 18 July 2017), using six new definitions of “UV auroral families” to help provide a simplified description of the complex dynamics observed in the UV auroral emissions: (1) Q (or ‘quiet’) has a very low auroral power (< 1 TW) with a lower latitude main emission (ME); (2) N has a ‘narrow’ and expanded ME, exhibiting average power; (3) U describes more ‘unsettled’ conditions and is the intermediate behaviour between Q and N; (4) I is associated with strong injections with a ‘corner-like’ morphology, located at ionospheric dusk with (5) more moderate injections being represented by the i family. (6) The final family, X, is linked to ‘eXternal’ perturbations generating very strong and contracted ME with large enhancements at dawn and strong, narrow auroral arcs in the afternoon-dusk sector. Such behaviour is usually observed during solar wind compressions. These new definitions allowed different morphologies to be compared to establish logical, plausible connections to identify the responsible auroral driver and allowed a more detailed quantitative way to analyse variations of spatial behaviour. G18 observed that auroral emissions corresponding to the U family occurred most often (29.5% of 118 HST images) and were identified to be connected to the Q family due to slight changes in brightness of the ME. The connection was only interrupted by episodes of injection events (I, i) which were observed to precede or follow the N family. The moderate injections, i, were identified after auroral structures associated with compressions of the interplanetary medium (X). The disturbances from compressions can trigger episodic injections of trapped particles in the middle magnetosphere, as observed by Louarn et al. (2014) from Galileo particle and radio measurements. More details of the UV auroral families described here can be found in G18. Yao et al. (2020) found that dawn storms and injection events were correlated with intervals of tail reconnection and dipolarization.

In this study, we utilise the techniques used for the UV auroral emissions to isolate and define specific auroral structures and apply them to the concentrated northern X-ray emissions in an attempt to find a link between X-ray morphology and magnetospheric dynamics. We use concurrent HST data to help provide vital magnetospheric context to the Chandra (Weisskopf et al., 2000) observations, using the G18 auroral definitions, and model the visibility of the X-ray auroral structures we define here, similar to Nichols et al. (2009). We then compare the magnetospheric dynamics found from the X-ray-UV data and compare with the magnetospheric conditions identified from the Juno spacecraft, using radio (Kurth et al., 2017) and magnetometer (Connerney et al., 2017) data. This allows us to determine the state of the jovian magnetosphere and to compare against the solar wind predictions of the Tao et al. (2005) 1D magnetohydrodynamic (MHD) solar wind propagation model. Similar to the logic applied by G18, the goal of this study is to simplify the complex morphological variations of the X-ray aurora, allowing plausible connections to be made between the auroral emissions and magnetospheric dynamics. Linking our X-ray structures with the UV equivalent may provide additional context from which to infer the state of the jovian magnetosphere in the absence of upstream solar wind data.

Previous observations noted morphological variations in the X-ray aurora and attempted to connect this with solar wind conditions for a limited sample of observations taken in 2007 and 2011, for which interpretation was further challenged by limitations on viewing geometry (Dunn et al., 2016; Dunn, Branduardi-Raymont, et al., 2020; Dunn, Gray, et al., 2020). The work here, with a more comprehensive observation dataset supported by *in situ* insights from the Juno spacecraft, may also help to put these historic X-ray observations into context.

2 Contemporaneous remote sensing UV and X-ray observations with Juno Waves and MAG data

We use the catalogue of Chandra HRC-I (High Resolution Camera - Imaging: 30 arcmin $\times$ 30 arcmin field of view, with pixel size 0.13 arcsec and spatial resolution of 0.4 arcsec) observations defined and tabulated in Weigt, Jackman, et al. (2021), focusing on those taken during the Juno main mission (24 May 2016 up to and including 8 September 2019). The Chandra observations used here are a combination of HXRs and SXRs due to the very limited spectral resolution of HRC-I, meaning that we cannot segregate photons of these two energy regimes. However, previous work suggested that greater than 90% of the observed X-ray photons detected by Chandra ACIS (Advanced CCD Imaging Spectrometer) were soft X-ray photons Dunn, Branduardi-Raymont, et al. (2020) and the energy response of HRC is softer than ACIS, so that we expect the majority of detected X-ray photons to be produced by precipitating ions. These observations include those taken during Juno's approach to Jupiter (in the solar wind), while Juno was at apojove (near the dawn magnetopause), during several perijoves and intervals when Juno was inside and crossed the jovian plasmasheet. We then correct the Chandra observations using the updated mapping algorithm described in McEntee et al. (2022), assuming the altitude of X-ray emissions is 400 km above the 1-bar atmosphere, to ensure that we have accounted for the time-dependent degradation of the Chandra HRC-I instru-

Table 1. Table of concurrent Chandra and HST observations throughout the Juno era. Date and time of each observation, identified UV auroral families from current literature using the G18 definition and predicted solar wind dynamic pressure from the Tao et al. (2005) model with average Jupiter-Sun-Earth angle are shown. Bold entries highlight observations associated with possible eXternal perturbation (X) structures. Solar wind parameters determined over a 2 day window centered on the Chandra observation to account for propagation errors withn Tao et al. (2005) model. Each Chandra observation is labelled with a unique Observation ID (ObsID).

Observation start date (dd/mm/yyyy)	Chandra ObsID	Observation interval (Juno time; light corrected)		HST UV northern auroral family*			Mean solar wind† P_{dyn} (nPa)	Max solar wind† P_{dyn} (nPa)	Mean Jupiter-Sun-Earth angle† (°)
		Chandra	HST	G18[a]	This study	D22[b]			
24/05/2016	18608	09:39 - 20:41	17:03 - 17:47 20:14 - 20:58	- -	U U	Q/N U	0.006	0.007	~ 57.7
01/06/2016	18609	10:47 - 21:49	14:13 - 14:57 17:24 - 18:08	- -	U U	Q/N Q/N	0.138	0.309	~ 64.6
02/02/2017	18301	09:14 - 18:19	16:17 - 16:57	-	i	i	0.009	0.015	~ -79.9
28/02 (Chandra); 01/03/2017 (HST)[c]	20000[c]	11:58 - 07:34	14:37 - 15:16	i	i	-	0.019	0.024	~ -53.3
18/05 - 19/05/2017	18302	23:48 - 10:10	04:27 - 05:07 06:03 - 06:43	N N	N N	N N	0.052	0.148	~ 19.2
18/06/2017[c]	**20001[c]**	**17:55 - 04:06**	**08:31 - 09:13**	**X**	**i**	**-**	**0.090**	**0.230**	**~ 47.9**
06/08/2017[d]	20002[d]	01:07 - 10:50	-	-	-	-	0.015	0.024	~ 99.0
01/04/2018	**18678**	**09:59 - 21:06**	**09:59 - 10:17**	**-**	**X**	**-**	**0.116**	**0.275**	**~ - 58.4**
23/05 - 24/05/2018	18679	23:22 - 10:21	09:02 - 09:32	-	U	Q	0.049	0.115	~ -3.6
06/09/2018	**18680**	**19:50 - 06:56**	**04:22 - 05:02**	**-**	**i**	**X**	**0.056**	**0.086**	**~ 97.0**
29/05/2019	22159	02:50 - 12:34	12:18 - 12:56	-	i	-	0.014	0.019	~ -32.5
15/07/2019	22148	12:21 - 19:13	14:06 - 14:44 15:41 - 16:17	- -	U U	N Q	0.068	0.115	~ 10.5
16/07/2019	22149	08:07 - 15:00	10:43 - 11:21	-	N/i	N	0.057	0.096	~ 11.3
18/07/2019[c]	22150[c]	19:40 - 01:32	14:10 - 14:49	-	i	-	0.012	0.018	~ 13.9
08/09/2019	**22151**	**08:01 - 14:46**	**14:24 - 15:02**	**-**	**X/i**	**-**	**0.262**	**0.879**	**~ 64.0**

* UV families as described in Grodent et al. (2018)

† Predicted values from Tao et al. (2005) model over 2 day window centered on Chandra observation

[a] UV families identified from Grodent et al. (2018) (G18)

[b] UV families identified from Dunn et al. (2022) (D22).

[c] observations not concurrent but occurred ± 1 day from Chandra interval.

[d] inferred compression from Juno data, no HST data.

ment while removing any contaminant background (Weigt et al., 2022). Here our focus is on the brightest and most concentrated X-ray northern auroral emissions, located using the Weigt et al. (2020) numerical criterion of >7 photons per 5° SIII longitude × 5° latitude over ∼ 10 hours (the average duration of the observations of the catalogue, around a jovian rotation). We note using this more updated mapping method provides minimal change in X-ray count rates from the Weigt, Jackman, et al. (2021) study and therefore does not change the interpretation of these results. We highlight here that accounting for the instrument's increasing degradation (and particle background) is crucial for future studies during the Juno extended mission (especially when mapping X-ray emissions to the jovian disk). The degradation of HRC-I has also been observed when analysing time-tagged photon data in a low-count regime from Saturn (Weigt, Dunn, et al., 2021).

To help provide essential magnetospheric context to the X-ray auroral emissions, we use HST observations concurrent with Chandra data. We analyse 17 Chandra observations during the Juno-era, 14 of which have HST Space Telescope Imaging Spectrograph (STIS: 24.7 arcsec × 24.7 arcsec field of view, spatial resolution of 0.0025 arcsec) data ± 1 day from the Chandra window, to allow the magnetospheric conditions to be analysed in detail. STIS detects far ultraviolet (FUV) auroral emissions of wavelengths ∼ 130 - 180 nm (photon energies ∼ 7 - 10 eV) using the F25SRF2 filter to eliminate geocoronal Ly-α contamination and to reduce the reflected sunlight from the jovian disk (e.g., Grodent (2015)). These 14 HST observations focus on the northern auroral emissions of which components within the UV aurora have been identified using the G18 definitions. We note that we add to this catalogue with three newly identified HST observations coinciding with Observation ID (ObsID) 22159 (29 May 2019), 22150 (18 June 2019) and 22151 (8 September 2019). All observations used in this research are shown in Table 1. To compare with contemporaneous Juno data, both the Chandra and HST intervals have been corrected for the Juno-Earth light-travel time, taken from ephemeris data obtained via the JPL Horizons database (data available at `https://ssd.jpl.nasa.gov/horizons/app.html#`). The mean and max dynamic pressure (P_{dyn}) estimated from the Tao et al. (2005) 1D MHD model over a 2 day window centered on the Chandra interval with the corresponding average Jupiter-Sun-Earth (JSE) angle are also given in Table 1. This 2-day window is used for all observations irrespective of JSE angle to account for propagation and interpolation errors. We note that Chandra observations taken beyond 8 September 2019 (and after the creation of the Weigt, Jackman, et al. (2021) catalogue) have no direct overlap with any HST campaigns and are therefore not included in this study.

We then compare these observations to remote sensing radio data (spectrograms) from Juno Waves and *in situ* data (time series) from the magnetometer, Juno MAG to confirm the magnetospheric state during these intervals and potentially identify any internal magnetospheric drivers (e.g. such as particle injection signatures). Juno's eccentric polar orbit allows it to sample the inner, middle and outer magnetosphere during its 53-day orbit, providing us the opportunity to analyse the different internal auroral drivers, hence the auroral emissions, located throughout the jovian magnetosphere. We take this into account when interpreting these data.

3 Results

Following studies that have identified different regions within the UV emissions associated with different potential drivers (e.g., Grodent et al. (2018)), we apply similar logic to the X-ray northern auroral emissions from the Weigt, Jackman, et al. (2021) Chandra catalogue during the Juno-era. Here we use the families defined from UV emissions from concurrent HST observations to provide vital context to the concentrated northern X-ray emissions and use the superior spatial resolution of HST-STIS to model the visibility of each X-ray auroral region.

3.1 Identifying X-ray auroral structures

As analyzed in the statistical study by Weigt, Jackman, et al. (2021), it is clear that the northern X-ray emissions exhibit large variations in morphological and temporal behaviours with only a very small region of X-rays appearing across the entire $\sim$ 20 year Chandra HRC-I dataset: the averaged hot spot nucleus (AHSNuc), mapping to the noon magnetopause boundary. We show examples of 2D histograms of mapped concentrated X-rays, using the Weigt et al. (2020) numerical criterion, in Figure 1 within the *X-ray noon* region (red), where the colour bar shows the photon flux of the X-rays (counts s^{-1}) and the 1D histograms show the latitude (lat) and System III longitude (SIII lon) distribution of the X-ray emissions. Similar to the 'Region X' defined in D22, the X-ray noon region contains both the UV swirl and active regions (Grodent et al., 2003) and therefore the X-ray emissions they may generate. The remaining X-ray auroral structures we define here are *X-ray dusk* (purple), *X-ray dawn* (gray), the *Low Latitude Extension region* (LLE; gold), equatorward of X-ray noon and the *X-ray polar region* (striped region) which envelopes both the noon and dusk structures. The statistical UV main emission (accounting for a compressed and expanded magnetosphere) and Io and Ganymede magnetic footprints taken from Bonfond et al. (2017) are also plotted to provide context of the location of these regions within the magnetosphere. The coordinates of each region (in SIII lon, lat) are given in the Supplementary Information (SI: see Data Set S1).

In Figure 1 (covering a central meridian longitude (CML) of 110° - 220°), we show four examples of different auroral morphologies each under different conditions: (a) where all auroral emissions are within the polar region (ObsID 18301: 2 February 2017); (b) where the most intense auroral emissions are observed to be shifted equatorward (ObsID 22151: 8 September 2019); (c) auroral morphology during a compressed magnetosphere (ObsID 20001: 18 June 2017) and (d) an observation during Juno a apojove (ObsID 18678: 1 April 2018). Three out of the four cases show the majority of the concentrated, and most intense, X-ray emissions are located in the X-ray polar region, dominated by X-ray noon. These emissions are therefore likely to be co-located (and possibly linked) with the UV activity in the polar and swirl regions and possibly coincide with flaring UV emissions (e.g., Elsner et al. (2005); Dunn (2022)). Previous studies (e.g., Grodent et al. (2003); Grodent (2015); Greathouse et al. (2021) and references therein) have also identified the polar active region as the most dynamic of the UV polar emissions, producing flares and bright arc sub-structures of a few hundred kilo-Rayleigh (kR) lasting in the order of a few minutes. The examples shown in Figure 1 are discussed further in the remainder of Section 3.

The X-ray dawn region is found to coincide with a portion of the main emission and the Io footprint suggesting an association between dawn storms, injections of hot plasma from the middle magnetosphere (e.g., Gerard et al. (1994); Kimura et al. (2017)) and bright X-ray populations. Recent work by Wibisono et al. (2021) found the intensity of the HXRs to increase during the presence of a dawn storm with reduced activity from the more poleward SXRs, utilising the energy resolution of XMM-Newton. Regions of X-ray dawn at higher latitudes are likely to overlap with the UV dark polar region (DPR) which contains very little UV emissions and is observed to contract and expand as Jupiter rotates, mapping to the outer magnetosphere (e.g., Pallier and Prangé (2001); Grodent et al. (2003); Swithenbank-Harris et al. (2019)). The DPR has been found to be the likely location of empty flux tubes, emptied via Vasyliūnas-like reconnection in the tail which then rotate to the dayside magnetosphere (Vasyliūnas, 1983), resulting in very little UV emissions here. Recent work by D22 found that the DPR is also present within the X-ray northern auroral emissions. D22 deduced from Chandra and HST observations (and simulated data) that very few or no X-ray photons are to be located in the DPR. They confirm this conclusion from their Monte Carlo simulations which state that the likelihood of X-rays being emitted from the DPR is very small, including

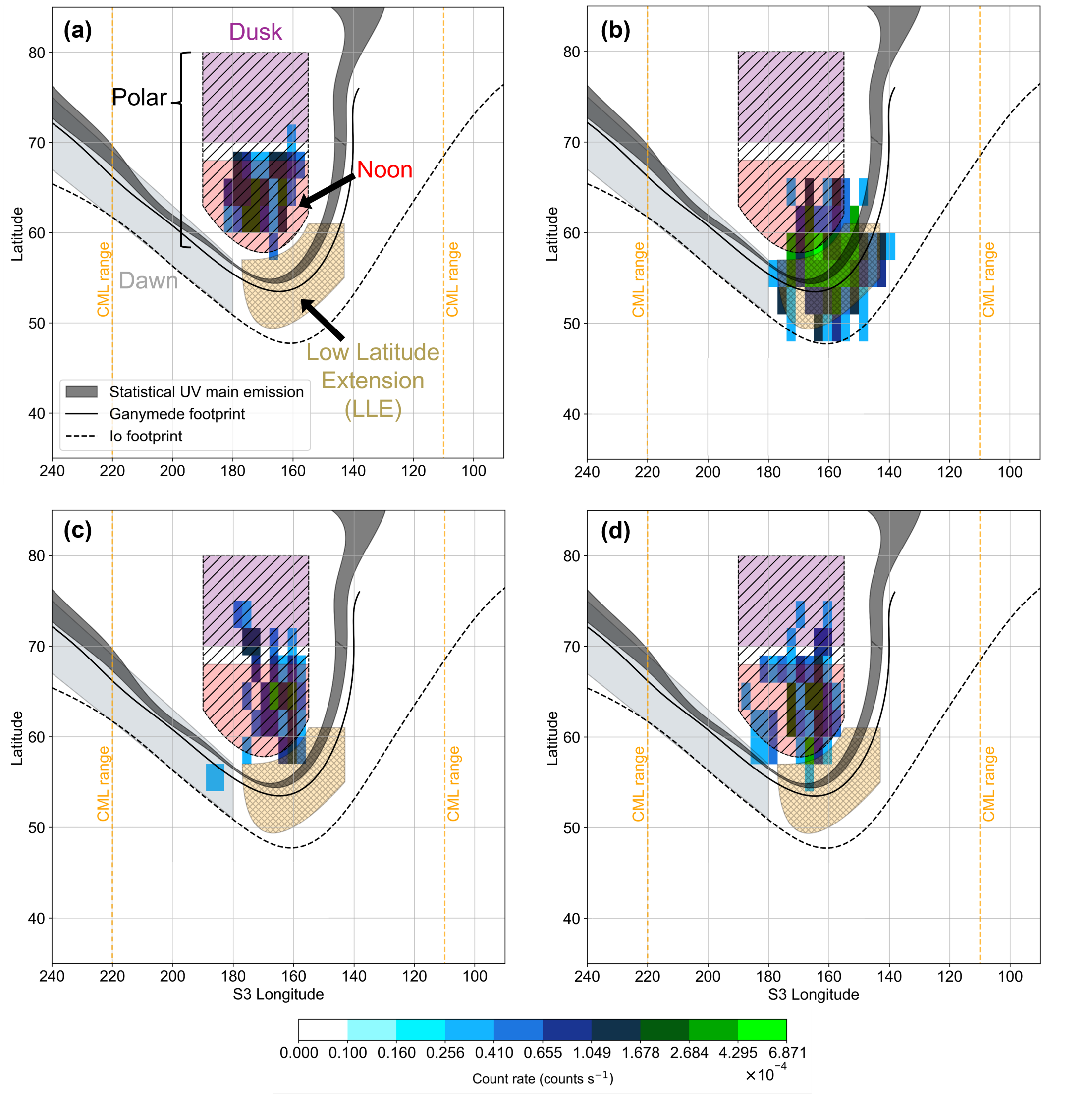

Figure 1. A Cartesian plot of the X-ray mapping for four example Chandra observations analysed in this research, each under different conditions: (a) ObsID 18301 (2 February 2017), where all auroral emissions are within the polar region; (b) ObsID 22151 (8 September 2019), where the auroral emissions are shifted equatorward; (c) ObsID 20001 (18 June 2017), auroral morphology during a compressed magnetosphere and (d) ObsID 18678 (1 April 2018), CXO observation during Juno apojove. Each case is expanded upon in the remainder of Section 3. The location of the X-ray auroral structures as described in the text (red: noon; purple: dusk; gray: dawn; gold: LLE; striped: polar) are shown in each panel and are labelled in (a). The count rates (counts s^{-1}) of the concentrated X-ray auroral emissions (2D histogram: binned by 3° SIII lon × 3° lat) are given by the colour bar. The statistical UV main emission accounting for compressed and expanded states (dark gray shading), and the footprints of Io (black-dashed line) and Ganymede (solid black line) are overplotted (Bonfond et al., 2017). The X-ray emissions mapped and analysed for this research are selected from a 9000 ± 1080 s interval, covering a central meridian longitude (CML) range of 110° - 220° (i.e. optimum visibility for each region as shown in Figure 2). This CML range is overplotted with orange dashed lines.

possible scattering of solar X-ray photons in the jovian upper atmosphere as an explanation for the sporadic and very dim X-ray emissions in the Dark region.

The regions likely to contain more extreme cases of auroral activity are the X-ray dusk (see Figures 1 (c) and (d)) and LLE regions (Figure 1 (b)) where the brightest emissions may span poleward or equatorward of the nominal position as found by Weigt, Jackman, et al. (2021), where it was observed that concentrated X-ray photons are occasionally (30 - 70% occurence) found at latitudes between 54° and 75°. Therefore these regions will likely contain rare auroral morphologies linked to more unusual or extreme magnetospheric dynamics. The LLE region covers an area of UV auroral emissions possibly associated with active particle injections from the middle magnetosphere driven by reconnection events and dipolarizations of the jovian magnetic field (e.g., Dumont et al. (2014, 2018); Yao et al. (2020)). Such injection events are found to occur alongside dawn storms, suggesting disturbances of the middle magnetosphere at a range of local times (e.g., Gray et al. (2016)). The 2-D histograms for all observations analysed and corresponding plots highlighting the filtering performed on the concentrated X-ray lightcurves photons using our CML criterion can be found in the SI (Figures S1 and S2).

3.2 Visibility and distribution of auroral photons across the X-ray auroral structures

The tilt of Jupiter, as viewed from the observer, can lead to issues of viewing geometry of the planet when using remote sensing data (e.g., Dunn et al. (2017); Dunn, Branduardi-Raymont, et al. (2020); Weigt, Jackman, et al. (2021)). As the magnetic field at the South pole is more dipolar, this tilt of the planet affects these emissions the most when viewed from Earth. However we cannot completely neglect such effects when viewing the northern emissions as the longitude of the observer (or CML) can change what parts of the emissions are observed. To resolve such issues, we utilise the higher spatial resolution of the HST-STIS instrument compared to Chandra to model the visibility of each X-ray auroral structure, using the area of the region defined in SIII lon and lat as they rotate into view of HST-STIS. We use the number of visible pixels of each X-ray region as it rotates into view as a proxy to gauge the visibility of our X-ray structures as viewed by an observer at Earth. In other words, we analyse how much of an effect the tilt of the planet has when observing fixed regions (in SIII lon and lat) on Jupiter from any Earth-based instrument. We define the visibility here as the number of visible STIS pixels associated with each X-ray region during one jovian rotation. We assume that the emissions across the area of the defined X-ray structures used in the model were uniform.

We adopt the method of Nichols et al. (2009) used to measure the visibility (as a function of normalized power) of different isolated components of UV auroral emissions during two HST campaigns in 2007, using the Advanced Camera for Surveys (ACS) Solar Blind Channel (SBC). Here we apply this algorithm to the X-ray structures, using the ionospheric position and size of each region as viewed by HST-STIS (with greater resolution than Chandra). Figure 2 shows the results of our visibility modelling over a full jovian rotation (e.g. full CML coverage) for the highest (orange: -3.39°) and lowest (black: = -1.52°) sub-Earth latitude during the Juno main mission for all X-ray auroral structures. The sub-Earth latitude relates to how tilted Jupiter is away from the observer, resulting in the peak for both cases being different. Here, we define the visibility as the number of pixels visible for each of the X-ray regions normalized to the maximum for the lowest planetary tilt case. The CML range (110° to 220°) used throughout this study is also overplotted in light-blue.

The location of peak visibility in all panels is associated with the optimum CML of which the full region is in view and is therefore related to the ionospheric position of the X-ray structure. The width of the peak gives an indication of the size of the region of interest. As shown in Figure 2, the location and width of the modelled peak visibil-

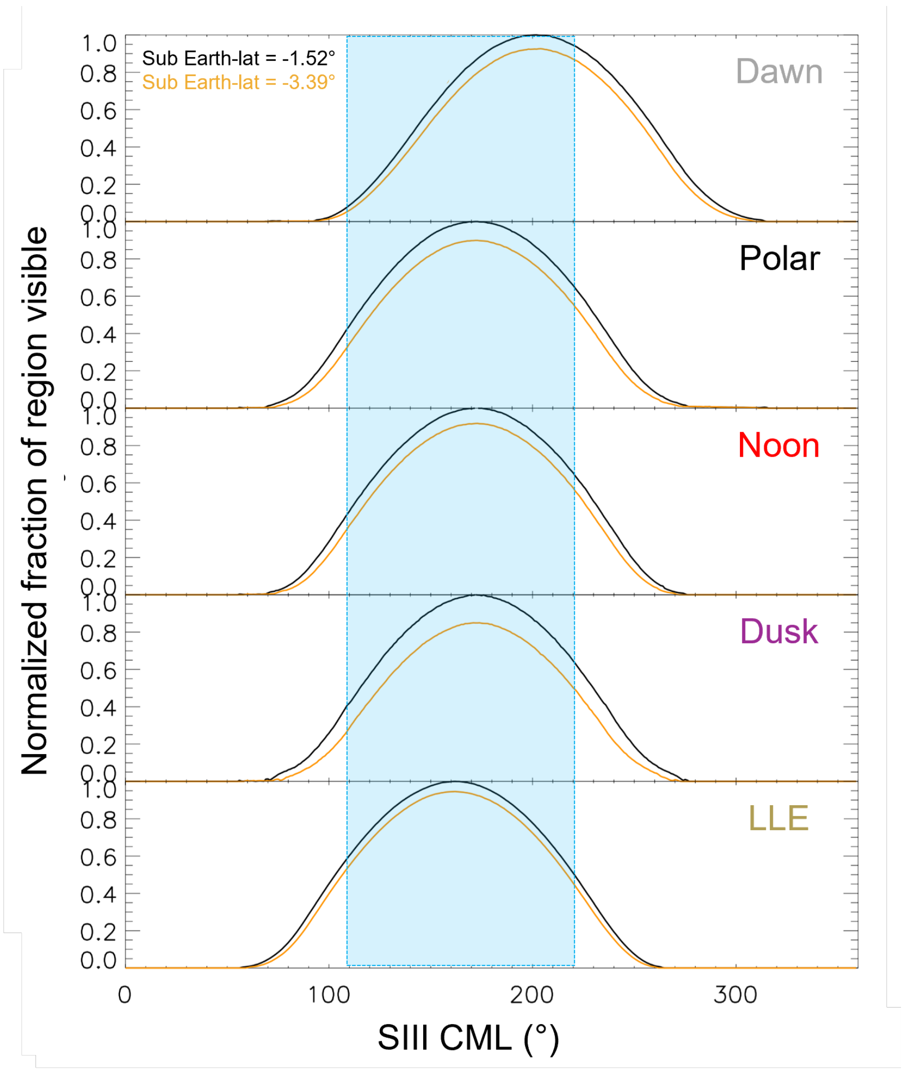

Figure 2. Plot showing the modelled normalized visibility for a full jovian rotation of each northern auroral region as observed from STIS on board HST. We model the visibility during the smallest (black: = -1.52°) and largest (orange: -3.39°) planetary tilt as viewed from Earth (sub-Earth latitude) during the Juno main science mission. The CML range used to analyse the concentrated X-ray emissions is overplotted with the light-blue shaded area. The number of pixels visible for each region is normalised to the maximum for the sub-Earth latitude = -1.52° case.

ity for the polar, noon and dusk regions (labelled with the same colours corresponding to the regions in Figure 1) are very similar as expected as all regions span the same SIII lon range. The main discrepancies are associated with the amplitude of the peak with the dusk region having the fewest number of visible pixels resulting from the region being more poleward and more difficult to view with HST-STIS [see Grodent (2015) for more details] and therefore more sensitive to sub-Earth latitude. The peak visibility of all the X-ray auroral structures lie within our CML range and therefore likely associated with the peak of the X-ray light curve of the northern emissions. We note X-ray noon is also affected by sub-Earth latitude to an extent, but the normalized fractional visibility still remains above 0.8 (i.e. $> 80\%$ of all pixels visible to noon) during the more restricted viewing geometry. Since the polar region is the accumulation of visible pixels from both X-ray noon and dusk, the modelled visibility curve is, as expected, a combination of both regions. The dawn region spans greater longitudes and surrounds the polar emissions, following a portion of the dawn main emission leading to the peak visibility shifting to higher CMLs. As the shape of X-ray dawn region is longer in size (i.e. spans a greater range of longitudes) the peak of the visibility curve is broader, as it is less sensitive to the tilt of the planet. This region is more equatorward than the X-ray polar region. This is similar for the LLE region, although this auroral structure spans the smallest range of longitudes out of the X-ray structures which is reflected by the width of the visibility curve. Although none of these results are particularly surprising, this is the first time the visibility of the X-ray auroral emissions has been modelled in this way.

The distributions of auroral X-ray photons within each of the auroral structures for each Chandra observation are shown as a stacked bar chart in Figure 3, with the ObsIDs in order of observation start date (as shown in Table 1) throughout the duration of Juno's main mission. Each region is represented by the same colours and labels used in Figure 1 with all four examples indicated by a black arrow. The mean number of total auroral photons populating the X-ray structures, μ, is given by a horizontal dashed line with a value 92.92%. In other words, $\sim 93\%$ of northern X-ray auroral emissions are likely to be located within the described X-ray regions. Observations where the sum of the components are $< 100\%$, as shown in Figure 3, indicate that concentrated emissions were also mapped to regions outside the X-ray auroral structures. The X-ray emissions used in the stacked bar chart, and mapped using the 2D histogram in Figure 1, span the same CML interval (110° - 220°) including the peak visibility of all regions. As many of the X-ray observations have different exposure times, this ensures we are removing any observation bias as the same portion of all northern auroral emissions is observed in each of the Chandra campaigns.

As shown by the highlighted example [introduced in Figure 1 (a): ObsID 18301] in Figure 3 and three other observations (ObsID 20002 (no HST intervals during this time), 18679 and 18680; details of the observations in Table 1), $\geq 95\%$ of concentrated northern auroral emissions are located within the X-ray polar region, and are dominated by X-ray noon photons. During these intervals there were no dawn or LLE region photons detected despite these regions being in view of Chandra at the time. However, many other observations have auroral photons located in this range within the same viewing and timing restraints. This therefore suggests that the potential drivers that cause emissions in these regions may be "switched off". Further evidence of this is shown by the observations that had a higher population of LLE photons ($> 10\%$ of total photons) with no X-ray dusk emissions (ObsID 18608, 18677, 22148, 22150 and 22151). This suggests that during these intervals, the concentrated X-ray emissions were located equatorward of the main emission and displaying more extreme morphological behaviour when compared to the averaged map of northern auroral emissions (Weigt, Jackman, et al., 2021). This is shown by the low occurrence rate of the X-ray emissions (using the same SIII lon/lat binning). The most extreme example, ObsID 22151 (8 September 2019: Figure 1b)), is a very rare case of the majority of the auroral emissions mapping to beyond the polar region. Examples where the auroral emissions span the LLE and X-ray dusk regions (e.g.,

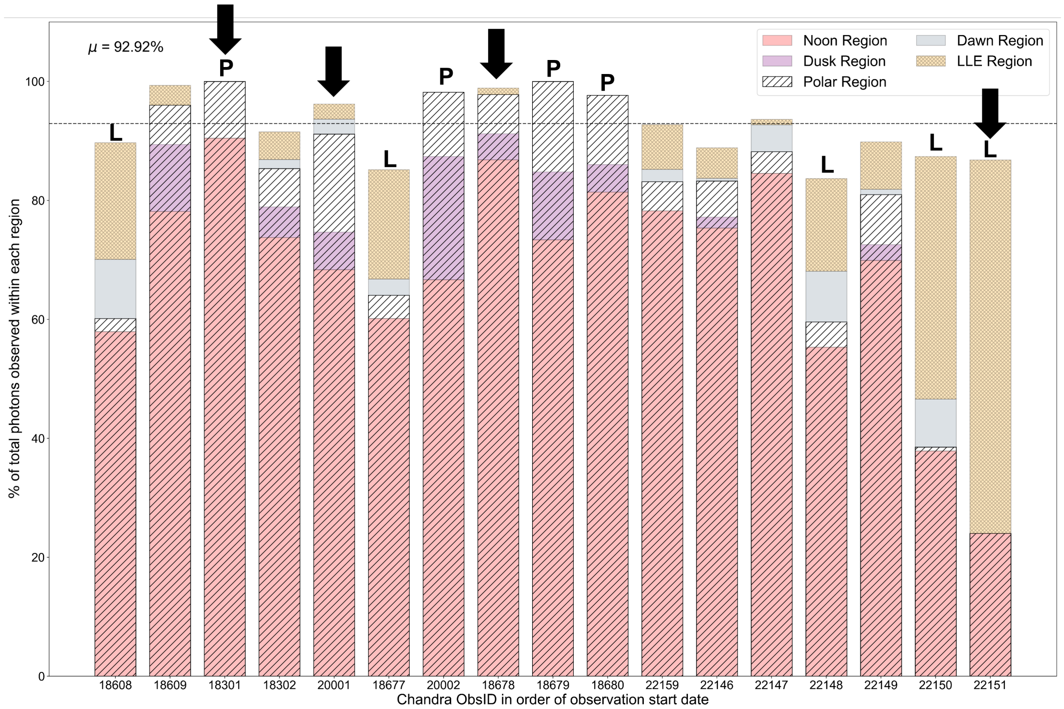

Figure 3. Stacked bar chart showing the distribution of all concentrated X-ray auroral emissions in each structure across the Juno-era Chandra observations (in order of date: Table 1), within the CML range. Each structure in both panels are labelled with identical colouring used in Figure 1. The mean, μ, is given and indicated by the horizontal line. The letters 'P' and 'L' above the bars indicate auroral morphologies that fall into either the 'fully polar emissions' or 'low latitude emissions' categories respectively, as defined in the text. The examples shown in Figure 1 are highlighted by black arrows.

18609, 18678, 22149) and an additional smaller population at X-ray dawn (20001, 18302, 22159) highlight possible elongation of the auroral emissions in both poleward and equatorward directions and/or possible X-ray emissions associated with UV injections.

From Figure 3, we can pick out two categories: (1) fully polar emissions (i.e. X-ray polar population $\geq 95\%$ of all auroral emissions) and (2) low latitude emissions (i.e. LLE photon population $> 10\%$). These observations are labelled with 'P' and 'L' for both categories respectively. The observations that exhibit intermediate behaviour between both categories (i.e. no 'P' or 'L' label) may imply a time-dependent relationship and therefore a link between the two. We do however need to compare the mapping of these morphologies with HST and Juno data to verify such a state. The key result we present here is the lack of uniformity across Figure 3 which shows that different regions can dominate when observing the northern concentrated X-ray auroral emissions. Adding a magnetospheric context this may suggest either that: (i) the switching on/off of potential magnetospheric drivers is likely to dominate or (ii) the regions where conditions are right for wave growth (i.e. standing Alfvén waves and/or EMIC waves on the magnetopause boundary) is changing. This is emphasized in Figure S3 (in SI) which shows scatter plots of photons observed in the polar region versus the LLE region and both regions plotted against inferred solar wind conditions from the Tao et al. (2005) model. As reflected in Figure 3, we observe an anticorrelation between photons population the polar and LLE regions. There is no clear link between solar wind dynamic pressure and these populations. This may indicate that either disturbances from the solar wind are observed in multiple regions and/or the LLE region 'switching on' is not directly linked to the compression and may lag ahead/behind the disturbance (i.e. similar to i/I-family). Further exploration into this is beyond the scope of this work although we hope our results will highlight key examples to use in future case studies.

3.3 Using *in situ* and remote sensing diagnostics to infer magnetospheric state

In order to understand the state of the jovian magnetosphere during the Chandra interval and constrain the driver(s) responsible for variable X-ray aurora, we combine predicted solar wind conditions from the 1D MHD propagation model by Tao et al. (2005) with data from the Juno fluxgate magnetometer (Juno MAG) and the radio and plasma wave instrument (Juno Waves). The purpose of the model is to infer how solar wind conditions can cause the jovian magnetosphere to contract and/or expand. We can therefore infer the state of the jovian magnetosphere, within an error of 2 days centred on the Chandra observation based on the alignment of the Sun, Earth and Jupiter. We also compare the predicted UV auroral families during the interval to the Juno data to verify the auroral behaviour and morphology. The aim here is to combine the UV and X-ray predicted morphologies with observed solar wind conditions as a possible proxy for magnetospheric conditions when there is no upstream *in situ* data.

Figure 4 shows the results of the Tao et al. (2005) 1D MHD solar wind propagation model combined with Juno MAG and Waves data, covering 4 days centred on the Chandra (CXO) observation (shaded in orange) taken on 16 June 2017 (ObsID 20001 - see Table 1 and Figure 1c)). The propagation model predicted many intervals where the solar wind dynamic pressure (P_{dyn}) was increased when acting on the jovian magnetosphere within model error, during a relatively reasonable Jupiter-Sun-Earth (JSE) alignment (panels (a) and (b)). We only consider JSE angles $< |60°|$ (highlighted in cyan) to ensure that the errors of the model are within the 2 day window, centered on the CXO interval. This conservative angle range allows us to explore of the Chandra catalogue, and compare how the model performs with real *in situ* data. The HST observation is shown by the gray interval. Both CXO and HST observations lie within the 2 day window accounting for errors in the Tao et al. (2005) model (gray dashed lines). This example was selected as this Chandra interval and Juno particle data were previously anal-

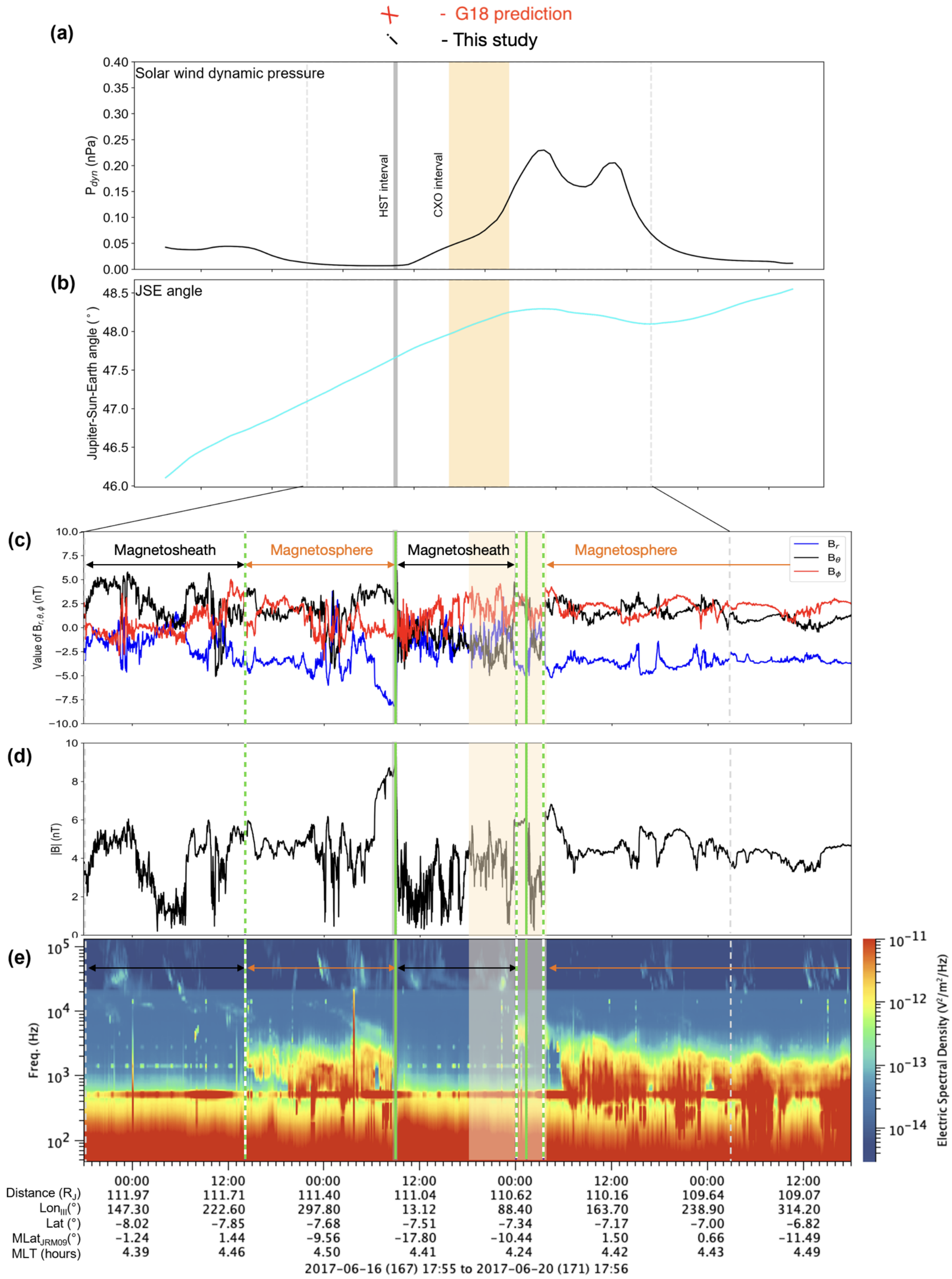

(Caption on next page)

Figure 4. Multi-panelled plot combining the results from the Tao et al. (2005) 1D MHD solar wind propagation model with Juno MAG and Waves, covering 4 days centring the Chandra observation (orange area) taken on 16 June 2017 (ObsID 20001 - see Table 1 for more details). Panels (a) and (b) show the predicted solar wind dynamic pressure (P_{dyn}) and associated JSE angle respectively, evolving over time with the Chandra (CXO) and HST observing intervals (gray area) shown in all panels. The angle represented in cyan shows periods of time when the value is $< |60°|$. Panels (c) and (d) show the Juno MAG in spherical components (B_r: blue, B_θ: black, B_ϕ: red) and the total field strength ($|B|$) measured by the Juno MAG data, in units of nanotesla (nT), within the Tao uncertainty window used in our analysis. (dashed gray vertical lines: shown in all panels). Panel (e) shows the concurrent Juno Waves data, measuring the electric spectral density of the radio and plasma wave emissions. The Juno ephemeris data during this interval is displayed at the bottom, showing its position in Jupiter's System III frame (in radial distance from Jupiter, R_{J}, and magnetic local time (MLT; hours)) and its position projected onto Jupiter's surface (SIII lon (Lon$_{III}$; degrees), SIII lat (Lat; degrees) and magnetic latitude found from the JRM09 field model (MLat$_{\mathrm{JRM09}}$; degrees)). The green-white dashed and solid green vertical lines represent Juno making inbound and outbound crossings of the magnetopause boundary respectively, as identified from Juno JADE data as described in Weigt et al. (2020). Juno's known position in the magnetosheath (black arrows) and magnetosphere (orange arrows) are also labelled. The identified UV auroral family using the Grodent et al. (2018) definitions from G18 (red) and this study (black), as shown in Table 1, are at the top of panel (a).

ysed by Weigt et al. (2020) to identify magnetopause crossings to infer a dynamic pressure from the Joy et al. (2002) model. When compared to the distributions of solar wind dynamic pressure (P_{dyn}) identified by Jackman and Arridge (2011) from upstream solar wind data at Jupiter spanning 1973 to 2004, both the Tao model and Juno data find the jovian magnetosphere to be compressed during this time ($P_{\mathrm{dyn}} = \sim 0.23$ - 0.39 nPa). These values lie at the upper tail of the distribution where the typical P_{dyn} observed from spacecraft data was 0.04 nPa.

The magnetopause crossings identified by Weigt et al. (2020) from Juno JADE data (green-white dashed and green solid vertical lines represent Juno making inbound and outbound respectively) are confirmed in the other Juno datasets (as shown in panels (c) - (e)) with a sharp change in the total magnetic field strength ($|B|$), in units of nanotesla (nT), and its spherical components (B_r: blue, B_θ: black, B_ϕ: red). The character of the magnetic field also changes during a crossing as it is noisier in the magnetosheath than in the magnetosphere. To locate the magnetopause boundary crossings (labelled with orange and black arrows), one can look at the Waves data (panel (e); colour bar showing the electric spectral density of the radio emissions), and in particular the appearance/disappearance of the non-thermal trapped continuum emissions (as conducted by Hospodarsky et al. (2017)). These emissions, observed between the electron plasma frequency and ~ 10 kHz, located in the jovian magnetospheric cavity where the emission frequency exceeds that of the surrounding plasma frequency (e.g., Gurnett and Scarf (1983)). When in the magnetosheath, the trapped continuum emissions are blocked by the denser sheath plasma. These emissions appear again when Juno enters the more rarefied magnetospheric plasma. These transitions in electric spectral density also align with the identified Juno crossings.

Finally, during the series of compressions Grodent et al. (2018) found that the UV auroral emissions exhibited features associated with the X-family (red label above panel (a)), suggesting that the magnetosphere was being affected by a solar wind compression

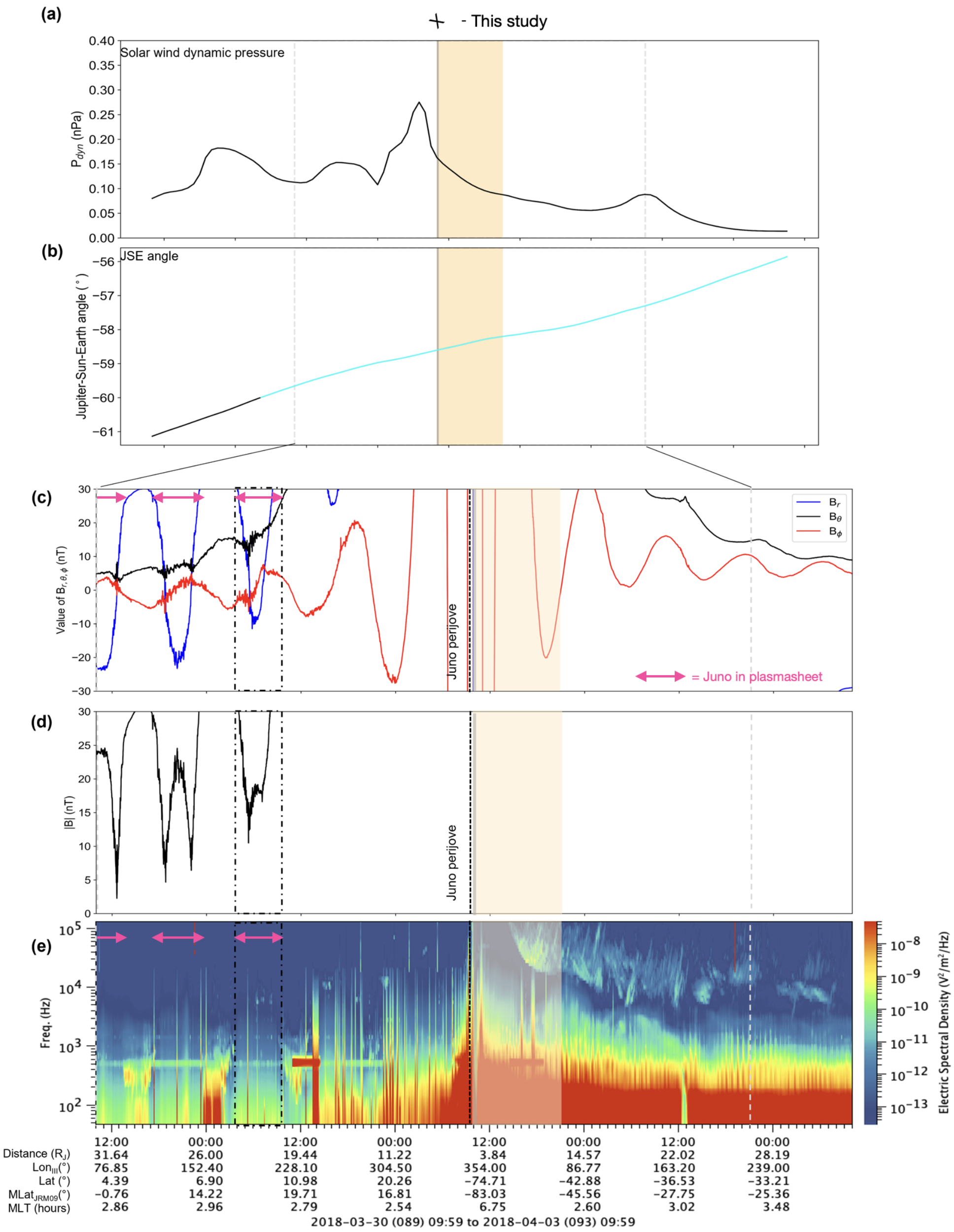

Figure 5. Multi-panelled plot for ObsID 18678 (1 April 2018) in identical format to Figure 4. The interval of the Juno perijove is shown by the black dashed line. Dotted black box highlights interval of potential dipolarization of the magnetic field (mainly in B_θ) associated with possible injection events in the UV aurora. The Grodent et al. (2018) UV family identified in this study is shown at the top of panel (a). Intervals when Juno is in the plasmasheet, identified from Juno Waves, prior to perijove are shown with pink arrows.

region. When comparing these results to Figure 3, the X-ray auroral emissions spans across multiple regions and are dominated by X-ray noon. We identify this morphology to likely be associated with the *i*-family (black label) or moderate injections which often occur after an external perturbation [see G18]. The X-ray morphology is observed to be between our defined categories and agree with Weigt et al. (2020) who observe the northern auroral emissions to be more extended and map to the dayside magnetopause boundary, along the noon-dusk sector using the Vogt et al. (2011, 2015) flux equivalence model. This may therefore suggest that, in this case, the auroral morphology reflects a magnetosphere disturbed in multiple regions and the the emissions likely remain poleward and more concentrated during intervals of compressions. This example was used as a "proof of concept" of compression identification as the location of Juno was near its apojove position. This allows analysis of the magnetospheric response to changing solar wind conditions in the *in situ* data.

Figure 5 shows an example when Juno is near perijove during the Chandra interval on 1 April 2018 (ObsID 18678 - see Table 1 and Figure 1d)), making it difficult to infer the state of the magnetosphere due to the very strong field strength as you approach Jupiter (panels (c) and (d)). Juno made several plasmasheet crossings prior to the CXO interval as shown by the sharp transition in electric spectral density, where the denser plasmasheet blocks the continuum emissions via refraction effects (analogous to the case of magnetopause crossings). Intervals when Juno is inside the plasmasheet are indicated by pink arrows. From this position we have limited ability from the *in situ* measurements to infer the upstream conditions, unlike at apojove when magnetopause boundary crossings can give us snapshots of magnetospheric size and inferred upstream dynamic pressure.

As shown in panels (a) and (b), the Tao et al. (2005) model suggests that there is a series of solar wind compressions during the Juno perijove interval, with maximum pressure of 0.275 nPa. In our analysis we identify that the UV auroral morphology was associated with the X-family, agreeing with the predicted model results, coinciding with the start of the CXO interval. As shown in panel (e), the spectrogram contains a variety of identifiable features including: periodic emissions (up to $\sim$ 1 - 100 kHz as bursts of high electric spectral density); broadband kilometric (bKOM) emissions in highest frequency channels, notably after perijove and the aforementioned continuum emissions, used as indicator of plasmasheet crossings. Therefore it is difficult to disentangle sources associated with the state of the jovian magnetosphere and verify the model results. We do however highlight a region of potential activity, as the dotted black box in Figure 5, in the magnetic field associated with a possible dipolarization of the field when Juno is inside the plasmasheet. A dipolarization occurs when the magnetic field line which Juno travels across changes from a stretched to a more dipolar configuration after a tail reconnection event, producing an anomalous feature in the B_θ component. Such dipolarizations of the field have been found to be associated with injection events found from HST UV observations and can be accompanied by bright dawn storm emissions (Yao et al., 2020). These bright dawn storm emissions have been found to be correlated with a brightening of HXR intensity in the jovian aurora (Wibisono et al., 2021), likely linked to similar regions of electron bremsstrahlung activity (e.g., Branduardi-Raymont et al. (2008). We do note that as the CXO interval was 2-3 jovian rotations after the potential injection event, it is unlikley that the X-ray morphology will reflect this behaviour. However, with the identified X-family (and its links to moderate injections) in the UV emissions the magnetosphere, across many sectors during this interval, is likely to be in a disturbed state.

When comparing Figure 5 to Figure 3, the auroral emissions found in ObsID 18678 exhibited morphology in between our defined categories. Like majority of emissions located in the X-ray polar region with a small portion of the emissions located in the LLE region ($<$ 10%). The small population of X-ray dusk photons indicate that the morphology extended polewards similar to ObsID 20001. Comparing Figures 1c) and (d), the auroral morphology is very similar with the exception of the dawn region. Therefore this distribution of X-ray auroral photons and UV auroral behaviour may be an indicator of a disturbed magnetosphere due to a potential compression event. Identifying such disturbances may be associated with a possible injection event which may precede or follow a compression event as observed by G18. We do note that further in depth analysis of the magnetic field and particle data is needed to confirm this, however the results provided here will likely highlight this observation (and many others associated with possible disturbances) as one of interest for further study.

4 Summary and Discussion

We present X-ray 'auroral structures' mapping to various regions in the magnetosphere linking X-ray auroral morphology to magnetospheric dynamics in the jovian system. Using CXO, HST and Juno data spanning the majority of Juno's main mission (24 May 2016 to 8 September 2019), we are able to compare observed magnetospheric dynamics to UV and X-ray remote sensing data. The results of our auroral distributions can be summarised as follows:

1. The X-ray auroral emissions show two clear categories of auroral morphological distributions: (1) fully polar aurora (2) low latitude emissions.
2. Non-uniformity of auroral distributions suggest there are likely numerous drivers responsible for the X-ray northern auroral emissions or conditions in the magnetosphere that permit the growth of drivers (i.e. EMIC waves) change.
3. Using UV and X-ray morphologies together may be a useful proxy for solar wind conditions (particularly during compressions) to identify magnetospheric disturbances.
4. Visibility (or planetary tilt) has very little effect when observing the auroral photon distributions.
5. X-ray auroral distributions may highlight potential magnetospheric phenomena (i.e., prior injection events) for future study.

We note that only CXO observations which had a HST observation $\pm$ 1 day from the Chandra window were considered for this study. For example, ObsID 20002 (6 August 2017; see full catalogue in Weigt, Jackman, et al. (2021)) does not appear in our study, however initial analysis of magnetopause crossings made by Juno suggest that the magnetosphere was compressed during this time using the Joy et al. (2002) model.

From the non-uniformity across the northern auroral distributions (Figure 3) and our visibility modelling of the regions, the lack of emissions we observe in a given region is more likely associated with the switching on/off of drivers. The X-ray noon population dominates the majority of observations suggesting that the likely driver from these emissions lies on the noon magnetopause boundary, as observed by Weigt, Jackman, et al. (2021). Here, X-ray noon coincides with the location of the UV polar and swirl region and therefore linked to a very dynamic region of the dayside magnetosphere. Dayside drivers such as magnetic reconnection would occur more frequently on the noon magnetosphere compared to other regions, especially during periods of high P_{dyn}. In these situations the solar wind is likely to reconnect with the jovian outer magnetosphere either at high latitudes in the cusps (Bunce et al., 2004) or compressions may induce reconnection inside the jovian system (i.e., at multiple smaller sites in the plasmasheet with more drizzle-like reconnection (Guo et al., 2018)). We note that previous analysis of three intervals during compression events (ObsID 20001, 20002, 18678) were found to exhibit very significant quasi-periodic oscillations (QPOs) within a region located in the center of X-ray noon (the averaged hot spot nucleus (AHSNuc)). These QPOs were observed to be between 2- and 4- minutes suggesting very dynamic activity on the noon boundary and timescales linked to magnetic reconnection on the boundary (Weigt, Jackman, et al., 2021). However, Weigt, Jackman, et al. (2021) observed that time QPOs were likely to be spatial dependent and therefore the period and statistical significance changes with where you observe in the aurora. They also stated that any activity may be initiated at the noon magnetopause boundary and be advected along the magnetopause boundary towards the flanks. This may explain the non-uniformity of auroral distributions we discuss here and how wave growth is promoted in other regions of the magnetosphere such as the strong correlations between X-ray emissions and EMIC waves found in the outer dawn and midnight magnetosphere (Yao et al., 2021). Therefore, assuming the auroral emissions are generated from wave activity, the changing auroral morphology may reveal the propensity for wave activity in different components in the jovian magnetosphere.

The peak visibility of each X-ray auroral structure was within our CML threshold throughout the Juno era during with changing sub-Earth latitudes mainly affecting those regions nearest to the pole (i.e., X-ray dusk). We do note however that the changing sub-Earth latitudes will have the greatest effect in the southern auroral region. Therefore future studies will need to develop a new set of X-ray auroral structures to combat this effect. The techniques discussed in this study can be extended to the southern auroral region and will allow detailed exploration and comparisons between both auroral regions (i.e., North-South asymmetry and non-conjugacy observed in the auroral X-ray emissions Branduardi-Raymont et al. (2004); Jackman et al. (2018); Weigt, Jackman, et al. (2021); Mori et al. (2022) and other wavelengths). This has already been shown by Mori et al. (2022) for HXRs, where non-thermal bremsstrahlung X-rays were $\sim$ twice as bright in the southern auroral region than the North, consistent with more persistent and stronger electron currents than those observed in the North (Kotsiaros et al., 2019).

In order to fully categorise the jovian X-ray auroral emissions and the extent of the solar wind influence at both poles, current X-ray technology needs to be expanded upon. Future potential missions such as Lynx (Falcone et al., 2019) and Line Emission Mapper (LEM; Kraft et al. (2022)) will allow us to explore in detail the various drivers generating X-ray emissions in the jovian magnetosphere. Utilising the enhanced spectral resolution i.e., 1-2 eV spectral resolution in the 0.2-2 keV range for LEM) and greater effective area at lower energies, we will be able to delve into the softer X-ray spectrum and evaluate the ion populations dominating various X-ray processes (e.g., charge exchange) and eventually inclduing the southern hemisphere. Coupling these remote sensing instruments with data from an *in situ* X-ray probe (Dunn et al., 2023) will be the key to fully understanding the magnetospheric drivers responsible for the jovian auroral X-ray emissions.

Data Availability Statement

This research has made use of data obtained from the *Chandra Data Archive* and *Chandra Source Catalogue* (`https://cda.harvard.edu/chaser/`); Juno Waves and MAG from the *the NASA Planetary Data System* and solar wind data obtained via AMDA (`http://amda.cdpp.eu/`). Waves survey data are at `https://doi.org/10.17189/1520498` . The catalogue of Chandra data required to reproduce the results shown in this study are stored in the Zenodo repository at `http://doi.org/10.5281/zenodo.4275744.`

Acknowledgments
DMW is supported by the Science and Technology Facilities Council (STFC) studentship ST/S505705/1 and long term attachment grant to work at the Dublin Institute for Advanced Studies (DIAS). DMW's work at DIAS is funded by European Union's Horizon 2020 research and innovation programme under grant agreement No. 952439 and project number AO 2-1927/22/NL/GLC/ov as part of the ESA OSIP Nanosats for Spaceweather Campaign. DMW's work at Trinity College Dublin is supported by Air Force Office of

Scientific Research award FA9550-19-1-7010. DMP is supported by a LUFST studentship. SVB is supported by STFC projects ST/M005534/1 and ST/V000748/1. CMJ, CKL and SCMcE work at DIAS is supported by the Science Foundation Ireland (SFI) Grant 18/FRL/6199. WRD was supported by Ernest Rutherford Fellowship: ST/W003449/1. CT acknowledges support by JSPS KAKENHI 20KK0074. The research at the University of Iowa is supported by NASA through Contract 699041X with Southwest Research Institute.

References

Badman, S. V., Branduardi-Raymont, G., Galand, M., Hess, S. L. G., Krupp, N., Lamy, L., … Tao, C. (2015). Auroral Processes at the Giant Planets: Energy Deposition, Emission Mechanisms, Morphology and Spectra. *Space Science Reviews*, *187*(1-4), 99–179. Retrieved from `http://dx.doi.org/10.1007/s11214-014-0042-xhttp://link.springer.com/10.1007/s11214-014-0042-x` doi: 10.1007/s11214-014-0042-x

Bolton, S. J., Lunine, J., Stevenson, D., Connerney, J. E. P., Levin, S., Owen, T. C., … Thorpe, R. (2017). The Juno Mission. *Space Science Reviews*, *213*(1-4), 5–37. Retrieved from `http://dx.doi.org/10.1007/s11214-017-0429-6http://link.springer.com/10.1007/s11214-017-0429-6` doi: 10.1007/s11214-017-0429-6

Bonfond, B., Saur, J., Grodent, D., Badman, S. V., Bisikalo, D., Shematovich, V., … Radioti, A. (2017). The tails of the satellite auroral footprints at Jupiter. *Journal of Geophysical Research (Space Physics)*, *122*(8), 7985-7996. doi: 10.1002/2017JA024370

Bonfond, B., Yao, Z. H., Gladstone, G. R., Grodent, D., Gérard, J., Matar, J., … Bolton, S. J. (2021). Are Dawn Storms Jupiter's Auroral Substorms? *AGU Advances*, *2*(1), 1–14. doi: 10.1029/2020av000275

Branduardi-Raymont, G., Elsner, R. F., Galand, M., Grodent, D., Cravens, T. E., Ford, P., … Waite, J. H. (2008). Spectral morphology of the X-ray emission from Jupiter's aurorae. *Journal of Geophysical Research: Space Physics*, *113*(2), 1–11. doi: 10.1029/2007JA012600

Branduardi-Raymont, G., Elsner, R. F., Gladstone, G. R., Ramsay, G., Rodriguez, P., Soria, R., & Waite, J. H. (2004). First observation of Jupiter by XMM-Newton. *Astronomy*, *337*(1149), 331–337. doi: 10.1051/0004-6361

Bunce, E. J., Cowley, S. W., & Yeoman, T. K. (2004). Jovian cusp processes: Implications for the polar aurora. *Journal of Geophysical Research: Space Physics*, *109*(A9), 1–26. doi: 10.1029/2003JA010280

Connerney, J. E. P., Benn, M., Bjarno, J. B., Denver, T., Espley, J., Jorgensen, J. L., … Smith, E. J. (2017). The Juno Magnetic Field Investigation. *Space Science Reviews*, *213*(1-4), 39–138. Retrieved from `http://dx.doi.org/10.1007/s11214-017-0334-z` doi: 10.1007/s11214-017-0334-z

Dumont, M., Grodent, D., Radioti, A., Bonfond, B., & Gérard, J. (2014). Jupiter's equatorward auroral features: Possible signatures of magnetospheric injections. *Journal of Geophysical Research: Space Physics*, *119*(12), A07000. Retrieved from `http://doi.wiley.com/10.1029/2006JA011892https://onlinelibrary.wiley.com/doi/abs/10.1002/2014JA020527` doi: 10.1002/2014JA020527

Dumont, M., Grodent, D., Radioti, A., Bonfond, B., Roussos, E., & Paranicas, C. (2018). Evolution of the Auroral Signatures of Jupiter's Magnetospheric Injections. *Journal of Geophysical Research: Space Physics*, *123*(2015), 1–13. Retrieved from `http://doi.wiley.com/10.1029/2018JA025708` doi: 10.1029/2018JA025708

Dunn, W., Berland, G., Roussos, E., Clark, G., Kollmann, P., Turner, D., … Kraft, R. P. (2023, March). Exploring Fundamental Particle Acceleration and Loss Processes in Heliophysics through an Orbiting X-ray Instrument in the Jovian

System. *arXiv e-prints*, arXiv:2303.02161. doi: 10.48550/arXiv.2303.02161

Dunn, W. R. (2022). X-Ray Emissions from the Jovian System. In *Handbook of x-ray and gamma-ray astrophysics. edited by cosimo bambi and andrea santangelo* (p. 110). doi: 10.1007/978-981-16-4544-0_73-1

Dunn, W. R., Branduardi-Raymont, G., Elsner, R. F., Vogt, M. F., Lamy, L., Ford, P. G., ... Jasinski, J. M. (2016). The impact of an ICME on the Jovian X-ray aurora. *Journal of Geophysical Research A: Space Physics*, *121*(3), 2274–2307. doi: 10.1002/2015JA021888

Dunn, W. R., Branduardi-Raymont, G., Ray, L. C., Jackman, C. M., Kraft, R. P., Elsner, R. F., ... Coates, A. J. (2017). The independent pulsations of Jupiter's northern and southern X-ray auroras. *Nature Astronomy*, *1*(11), 758–764. Retrieved from `http://dx.doi.org/10.1038/s41550-017-0262-6` doi: 10.1038/s41550-017-0262-6

Dunn, W. R., Branduardi-Raymont, G., Carter-Cortez, V., Campbell, A., Elsner, R., Ness, J.-U., ... Achilleos, N. (2020). Jupiter's X-ray Emission During the 2007 Solar Minimum. *Journal of Geophysical Research: Space Physics*, *125*(6), e2019JA027219. Retrieved from `https://onlinelibrary.wiley.com/doi/abs/10.1029/2019JA027219` doi: 10.1029/2019JA027219

Dunn, W. R., Gray, R., Wibisono, A. D., Lamy, L., Louis, C., Badman, S. V., ... Kraft, R. (2020). Comparisons Between Jupiter's X-ray, UV and Radio Emissions and In-Situ Solar Wind Measurements During 2007. *Journal of Geophysical Research: Space Physics*, *125*(6), e2019JA027222. Retrieved from `https://onlinelibrary.wiley.com/doi/abs/10.1029/2019JA027222` doi: 10.1029/2019JA027222

Dunn, W. R., Weigt, D. M., Grodent, D., Yao, Z. H., May, D., Feigelman, K., ... Ray, L. C. (2022). Jupiter's X-ray and UV Dark Polar Region. *Geophysical Research Letters*, *4*. Retrieved from `https://onlinelibrary.wiley.com/doi/10.1029/2021GL097390` doi: 10.1029/2021GL097390

Elsner, R. F., Lugaz, N., Waite, J. H., Cravens, T. E., Gladstone, G. R., Ford, P., ... Majeed, T. (2005). Simultaneous Chandra X ray Hubble Space Telescope ultraviolet, and Ulysses radio observations of Jupiter's aurora. *Journal of Geophysical Research: Space Physics*, *110*(A1), 1–16. doi: 10.1029/2004JA010717

Falcone, A. D., Kraft, R. P., Bautz, M. W., Gaskin, J. A., Mulqueen, J. A., & Swartz, D. A. (2019). Overview of the high-definition x-ray imager instrument on the Lynx x-ray surveyor. *Journal of Astronomical Telescopes, Instruments, and Systems*, *5*(2). doi: 10.1117/1.JATIS.5.2.021019

Gerard, J. C., Grodent, D., Prange, R., Waite, J. H., Gladstone, G. R., Dols, V., ... Franke, K. A. (1994). A Remarkable Auroral Event on Jupiter Observed in the Ultraviolet with the Hubble Space Telescope. *Science*, *266*(5191), 1675-1678. doi: 10.1126/science.266.5191.1675

Gray, R. L., Badman, S. V., Bonfond, B., Kimura, T., Misawa, H., Nichols, J. D., ... Ray, L. C. (2016). Auroral evidence of radial transport at Jupiter during January 2014. *Journal of Geophysical Research: Space Physics*, *121*(10), 9972–9984. Retrieved from `https://onlinelibrary.wiley.com/doi/abs/10.1002/2016JA023007` doi: 10.1002/2016JA023007

Greathouse, T., Gladstone, R., Versteeg, M., Hue, V., Kammer, J., Giles, R., ... Vogt, M. F. (2021). Local Time Dependence of Jupiter's Polar Auroral Emissions Observed by Juno UVS. *Journal of Geophysical Research: Planets*, *126*(12), 1–13. doi: 10.1029/2021JE006954

Grodent, D. (2015). A Brief Review of Ultraviolet Auroral Emissions on Giant Planets. *Space Science Reviews*, *187*(1-4), 23–50. Retrieved from `http://dx.doi.org/10.1007/s11214-014-0052-8` doi: 10.1007/s11214-014-0052-8

Grodent, D., Bonfond, B., Yao, Z., Gérard, J. C., Radioti, A., Dumont, M., ... Valek, P. (2018). Jupiter's Aurora Observed With HST During Juno Orbits 3 to 7. *Journal of Geophysical Research: Space Physics*, *123*(5), 3299–3319. doi:

10.1002/2017JA025046

Grodent, D., Clarke, J. T., Kim, J., Waite, J. H., & Cowley, S. W. H. (2003). Jupiter's main auroral oval observed with HST-STIS. *Journal of Geophysical Research (Space Physics)*, *108*(A11), 1389. doi: 10.1029/2003JA009921

Grodent, D., Clarke, J. T., Waite, J. H., Cowley, S. W., Gérard, J. C., & Kim, J. (2003). Jupiter's polar auroral emissions. *Journal of Geophysical Research: Space Physics*, *108*(A10), 1–9. doi: 10.1029/2003JA010017

Guo, R. L., Yao, Z. H., Sergis, N., Wei, Y., Mitchell, D., Roussos, E., ... Wan, W. X. (2018). Reconnection Acceleration in Saturn's Dayside Magnetodisk: A Multicase Study with Cassini . *The Astrophysical Journal*, *868*(2), L23. Retrieved from `http://dx.doi.org/10.3847/2041-8213/aaedab` doi: 10.3847/2041-8213/aaedab

Gurnett, D. A., & Scarf, F. L. (1983). Plasma waves in the jovian magnetosphere. In A. J. Dessler (Ed.), *Physics of the jovian magnetosphere* (p. 285–316). Cambridge University Press. doi: 10.1017/CBO9780511564574.010

Hospodarsky, G. B., Kurth, W. S., Bolton, S. J., Allegrini, F., Clark, G. B., Connerney, J. E., ... Valek, P. W. (2017). Jovian bow shock and magnetopause encounters by the Juno spacecraft. *Geophysical Research Letters*, *44*(10), 4506–4512. doi: 10.1002/2017GL073177

Houston, S. J., Cravens, T. E., Schultz, D. R., Gharibnejad, H., Dunn, W. R., Haggerty, D. K., ... Ozak, N. (2020). Jovian Auroral Ion Precipitation: X-Ray Production From Oxygen and Sulfur Precipitation. *Journal of Geophysical Research: Space Physics*, *125*(2), 2019JA027007. Retrieved from `https://onlinelibrary.wiley.com/doi/10.1029/2019JA027007` doi: 10.1029/2019JA027007

Jackman, C. M., & Arridge, C. S. (2011). Solar Cycle Effects on the Dynamics of Jupiter's and Saturn's Magnetospheres. *Solar Physics*, *274*(1-2), 481–502. doi: 10.1007/s11207-011-9748-z

Jackman, C. M., Knigge, C., Altamirano, D., Gladstone, R., Dunn, W., Elsner, R., ... Ford, P. (2018). Assessing Quasi-Periodicities in Jovian X-Ray Emissions: Techniques and Heritage Survey. *Journal of Geophysical Research: Space Physics*, *123*(11), 9204–9221. doi: 10.1029/2018JA025490

Joy, S. P., Kivelson, M. G., Walker, R. J., Khurana, K. K., Russell, C. T., & Ogino, T. (2002). Probabilistic models of the Jovian magnetopause and bow shock locations. *Journal of Geophysical Research: Space Physics*, *107*(A10), 1–17. doi: 10.1029/2001JA009146

Kimura, T., Nichols, J. D., Gray, R. L., Tao, C., Murakami, G., Yamazaki, A., ... Fujimoto, M. (2017). Transient brightening of Jupiter's aurora observed by the Hisaki satellite and Hubble Space Telescope during approach phase of the Juno spacecraft. *Geophysical Research Letters*, *44*(10), 4523–4531. doi: 10.1002/2017GL072912

Kotsiaros, S., Connerney, J. E., Clark, G., Allegrini, F., Gladstone, G. R., Kurth, W. S., ... Levin, S. M. (2019). Birkeland currents in Jupiter's magnetosphere observed by the polar-orbiting Juno spacecraft. *Nature Astronomy*, *3*(10), 904–909. Retrieved from `http://dx.doi.org/10.1038/s41550-019-0819-7` doi: 10.1038/s41550-019-0819-7

Kraft, R., Markevitch, M., Kilbourne, C., Adams, J. S., Akamatsu, H., Ayromlou, M., ... ZuHone, J. (2022, November). Line Emission Mapper (LEM): Probing the physics of cosmic ecosystems. *arXiv e-prints*, arXiv:2211.09827. doi: 10.48550/arXiv.2211.09827

Kurth, W. S., Hospodarsky, G. B., Kirchner, D. L., Mokrzycki, B. T., Averkamp, T. F., Robison, W. T., ... Zarka, P. (2017). The Juno Waves Investigation. *Space Science Reviews*, *213*(1-4), 347–392. Retrieved from `http://dx.doi.org/10.1007/s11214-017-0396-y` doi: 10.1007/s11214-017-0396-y

Louarn, P., Paranicas, C. P., & Kurth, W. S. (2014). Global magnetodisk disturbances and energetic particle injections at Jupiter. *Journal of Geophysical Research: Space Physics*, *119*(6), 4495-4511. doi: 10.1002/2014JA019846

McComas, D. J., Szalay, J. R., Allegrini, F., Bagenal, F., Connerney, J., Ebert, R. W., ... Bolton, S. (2017). Plasma environment at the dawn flank of Jupiter's magnetosphere: Juno arrives at Jupiter. *Geophysical Research Letters*, *44*(10), 4432–4438. doi: 10.1002/2017GL072831

McEntee, S. C., Jackman, C. M., Weigt, D. M., Dunn, W. R., Kashyap, V., Kraft, R., ... Gallagher, P. T. (2022). Comparing jupiter's equatorial x-ray emissions with solar x-ray flux over 19 years of the chandra mission. *Journal of Geophysical Research: Space Physics*, *127*. Retrieved from `https://onlinelibrary.wiley.com/doi/10.1029/2022JA030971` doi: 10.1029/2022JA030971

Mori, K., Hailey, C., Bridges, G., Mandel, S., Garvin, A., Grefenstette, B., ... Ray, L. (2022). Observation and origin of non-thermal hard X-rays from Jupiter. *Nature Astronomy*. Retrieved from `https://www.nature.com/articles/s41550-021-01594-8` doi: 10.1038/s41550-021-01594-8

Nichols, J. D., Badman, S. V., Bagenal, F., Bolton, S. J., Bonfond, B., Bunce, E. J., ... Yoshikawa, I. (2017). Response of Jupiter's auroras to conditions in the interplanetary medium as measured by the Hubble Space Telescope and Juno. *Geophysical Research Letters*, *44*(15), 7643–7652. Retrieved from `http://doi.wiley.com/10.1002/2017GL073029` doi: 10.1002/2017GL073029

Nichols, J. D., Clarke, J. T., Gérard, J. C., Grodent, D., & Hansen, K. C. (2009). Variation of different components of jupiter's auroral emission. *Journal of Geophysical Research: Space Physics*, *114*(6), 1–18. doi: 10.1029/2009JA014051

Pallier, L., & Prangé, R. (2001). More about the structure of the high latitude Jovian aurorae. *Planetary and Space Science*, *49*(10-11), 1159-1173. doi: 10.1016/S0032-0633(01)00023-X

Swithenbank-Harris, B. G., Nichols, J. D., & Bunce, E. J. (2019). Jupiter's Dark Polar Region as Observed by the Hubble Space Telescope During the Juno Approach Phase. *Journal of Geophysical Research: Space Physics*, *124*(11), 9094–9105. doi: 10.1029/2019JA027306

Tao, C., Kataoka, R., Fukunishi, H., Takahashi, Y., & Yokoyama, T. (2005). Magnetic field variations in the Jovian magnetotail induced by solar wind dynamic pressure enhancements. *Journal of Geophysical Research: Space Physics*, *110*(A11), 1–9. doi: 10.1029/2004JA010959

Vasyliūnas, V. M. (1983). Plasma distribution and flow. In A. J. Dessler (Ed.), *Physics of the jovian magnetosphere* (pp. 395–453). Cambridge: Cambridge University Press. Retrieved from `https://www.cambridge.org/core/product/identifier/CBO9780511564574A082/type/book{\_}part` doi: 10.1017/CBO9780511564574.013

Vogt, M. F., Bunce, E. J., Kivelson, M. G., Khurana, K. K., Walker, R. J., Radioti, A., ... Grodent, D. (2015). Magnetosphere-ionosphere mapping at Jupiter: Quantifying the effects of using different internal field models. *Journal of Geophysical Research: Space Physics*, *120*(4), 2584–2599. doi: 10.1002/2014JA020729

Vogt, M. F., Kivelson, M. G., Khurana, K. K., Walker, R. J., Bonfond, B., Grodent, D., & Radioti, A. (2011). Improved mapping of Jupiter's auroral features to magnetospheric sources. *Journal of Geophysical Research: Space Physics*, *116*(3). doi: 10.1029/2010JA016148

Weigt, D. M., Dunn, W. R., Jackman, C. M., Kraft, R., Branduardi-Raymont, G., Nichols, J. D., ... Gladstone, G. R. (2021). Searching for Saturn's X-rays during a rare Jupiter Magnetotail crossing using Chandra. *Monthly Notices of the Royal Astronomical Society*, *506*(1), 298–305. Retrieved from `https://academic.oup.com/mnras/article/506/1/298/6298248` doi:

10.1093/mnras/stab1680
Weigt, D. M., Gladstone, G. R., McEntee, S. C., Dunn, W. R., Kashyap, V. L., Jackman, C. M., ... Branduardi-Raymont, G. (2022). *Chandra_x-ray_data_processing_pipeline version 1.0.2 (v1.0.2) [computer software].* Zenodo. doi: 10.5281/ZENODO.7380282

Weigt, D. M., Jackman, C. M., Dunn, W. R., Gladstone, G. R., Vogt, M. F., Wibisono, A. D., ... Kraft, R. P. (2020). Chandra Observations of Jupiter's X-ray Auroral Emission During Juno Apojove 2017. *Journal of Geophysical Research: Planets*, *125*(4), e2019JE006262. Retrieved from `https://onlinelibrary.wiley.com/doi/abs/10.1029/2019JE006262` doi: 10.1029/2019JE006262

Weigt, D. M., Jackman, C. M., Vogt, M. F., Manners, H., Dunn, W. R., Gladstone, G. R., ... McEntee, S. C. (2021). Characteristics of Jupiter's X-Ray Auroral Hot Spot Emissions Using Chandra. *Journal of Geophysical Research: Space Physics*, *126*(9). Retrieved from `https://onlinelibrary.wiley.com/doi/10.1029/2021JA029243` doi: 10.1029/2021JA029243

Weisskopf, M. C., Tananbaum, H. D., Van Speybroeck, L. P., & O'Dell, S. L. (2000). Chandra X-ray Observatory (CXO): overview. *X-Ray Optics, Instruments, and Missions III*, *4012*(July 2000), 2–16. doi: 10.1117/12.391545

Wibisono, A. D., Branduardi-Raymont, G., Dunn, W. R., Kimura, T., Coates, A. J., Grodent, D., ... Haythornthwaite, R. P. (2021). Jupiter's X-ray aurora during UV dawn storms and injections as observed by XMM-Newton, Hubble, and Hisaki. *Monthly Notices of the Royal Astronomical Society*, *507*(1), 1216-1228. doi: 10.1093/mnras/stab2218

Yao, Z., Bonfond, B., Clark, G., Grodent, D., Dunn, W., Vogt, M., ... Bolton, S. (2020). Reconnection- and Dipolarization-Driven Auroral Dawn Storms and Injections. *Journal of Geophysical Research: Space Physics*, *125*(8). doi: 10.1029/2019JA027663

Yao, Z., Dunn, W., Woodfield, E., Clark, G., Mauk, B., Ebert, R., ... Bolton, S. (2021). Revealing the source of jupiter's x-ray auroral flares. *Science Advances*, *7*(28), eabf0851. Retrieved from `https://www.science.org/doi/abs/10.1126/sciadv.abf0851` doi: 10.1126/sciadv.abf0851

Yoshioka, K., Murakami, G., Yamazaki, A., Tsuchiya, F., Kagitani, M., Sakanoi, T., ... Yoshikawa, I. (2013). The extreme ultraviolet spectroscope for planetary science, EXCEED. *Planetary and Space Science*, *85*, 250-260. doi: 10.1016/j.pss.2013.06.021

Journal of Geophysical Research: Space Physics

Supporting Information for

Identifying the variety of jovian X-ray auroral structures: tying the morphology of X-ray emissions to associated magnetospheric dynamics

D. M. Weigt[1,2,3], C. M. Jackman[2], D. Moral-Pombo[4], S. V. Badman[4], C. K. Louis[2], W. R. Dunn[5], S. C. McEntee[2,3], G. Branduardi-Raymont[6], D. Grodent[7], M. F. Vogt[8], C. Tao[9], G. R. Gladstone[10], R. P. Kraft[11], W. S. Kurth[12] and J. E. P. Connerney[13,14]

[1]School of Physics and Astronomy, University of Southampton, Southampton, UK
[2] Astronomy and Astrophysics Section, Dublin Institute for Advanced Studies, Dublin, Ireland
[3] School of Physics, Trinity College Dublin, Dublin, Ireland
[4] Department of Physics, Lancaster University, Lancaster, UK
[5] Department of Physics and Astronomy, University College London, UK
[6] Mullard Space Science Laboratory, Department of Space and Climate Physics, University College London, Dorking, UK
[7] Laboratory for Planetary and Atmospheric Physics, Space Science, Technologies, and Astrophysical, Research Institute, University of Liège, Liège, Belgium
[8]Center for Space Physics, Boston University, Boston, MA, USA
[9] National Institute of Information and Communications Technology, Tokyo, Japan
[10]Southwest Research Institute, San Antonio, TX, USA
[11]Harvard-Smithsonian Center for Astrophysics, Smithsonian Astrophysical Observatory, Cambridge, MA, USA
[12]Department of Physics and Astronomy, University of Iowa, Iowa City, IA, USA
[13]Space Research Corporation, Annapolis, MD, 21403, USA
[14]NASA Goddard Space Flight Center, Greenbelt, MD, 20771, USA

Contents of this file

Data Set S1
Figures S1 and S2 (caption only)
Figure S3

Additional Supporting Information (Files uploaded separately)

Data Set S1 given in .zip file
Figures S1 and S2 given in uploaded PDFs

Introduction

The datasets and figures presented here are not crucial to understand this paper but used to emphasize and aid in recreating the main results. We present the following:

- Coordinates (in SIII lon, lat) of the vertices used to define the X-ray auroral structures described in Figure 1 (separate file; **Date Set S1**).
- List of figures showcasing our CML spatial selection (i.e., motivation behind our selected CML range) from the X-ray light curves and the spatial distribution of the selected photons (separate file; **Figure S1**).
- List of figures showing **all** 2D histograms used in our analysis in the style of Figure 1 and the various morphologies as highlighted in Figure 3 (separate file; **Figure S2**).
- Scatter plots showing the correlation between %LLE and %polar photons with each other and solar wind dynamic pressure inferred from the Tao et al., (2005) model (shown here; **Figure S3**).

The files are designed to allow the reader to gain extra information and context about the main results of the paper, and to potentially identify case studies for further research.

Data Set S1. Zip file containing text files for location each X-ray structure boundary. Coordinates are in System III system (SII lon, lat). Zip file name: **dataset_S1.**zip. **NOTE:** each text file provides the vertices of each polygon. Each has file name of format: <X-ray_region>_boundary_v1.txt

Figure S1. 2D histograms of all auroral observations analyzed in this research in the same format as Figure 1. The Observation ID (ObsID) of each Chandra observation is sh own at the top of each figure. More information of each ObsID (e.g., date, concurrent HST observation etc.) can be found in Table 1 in text. **See FigureS1.pdf**

Figure S2. Multipaneled plot showing which portion of the light curve was selected for analysis using our CML thresholding, for all Chandra observations. The full X-ray light curve and down selected region (shown by dashed red box) are displayed in panels (a) and (b). Panels (c) and (d) show comparisons of the CML distributions of each photon with the SIII longitude and latitude. The purpose of this figure is to show that we always select the peak of the X-ray curve when the full auroral region is view, and disregard any emergences of the envelope that can appear at the beginning/end of the observation window. **See FigureS2.pdf**

Figure S3. Scatter plots showing the correlation between (a) % of photons observed in the polar region vs LLE region; (b) % of photons in polar region vs. solar wind dynamic pressure (in log scale) found from Tao model during each interval and (c) similarly for LLE photons. Different colors represent each single Chandra observation. Figure on next page.

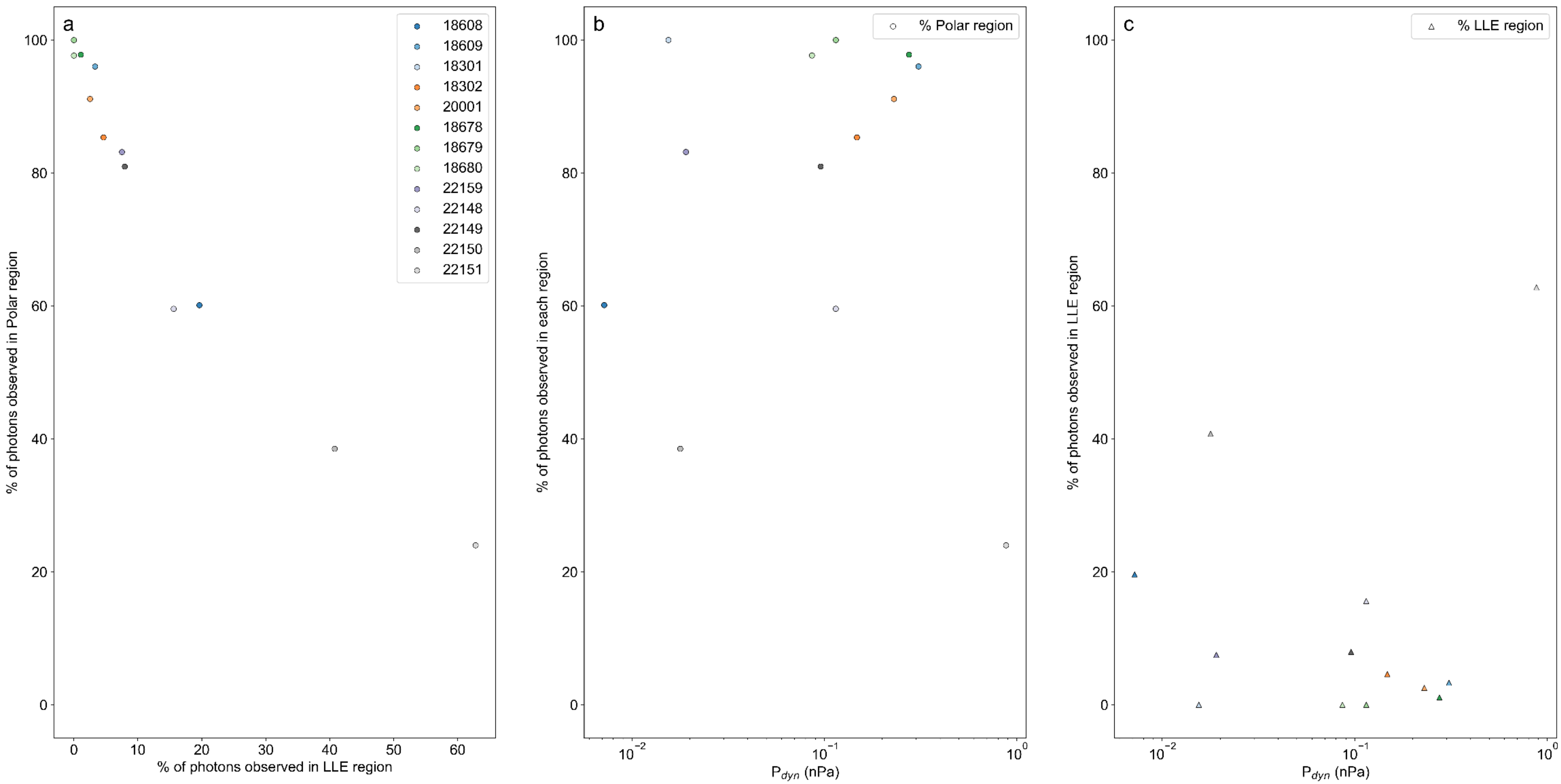
a
b
c
18608
18609
18301
18302
20001
18678
18679
18680
22159
22148
22149
22150
22151
% Polar region
% LLE region
% of photons observed in Polar region
% of photons observed in LLE region
% of photons observed in each region
% of photons observed in LLE region
P$_{dyn}$ (nPa)
P$_{dyn}$ (nPa)

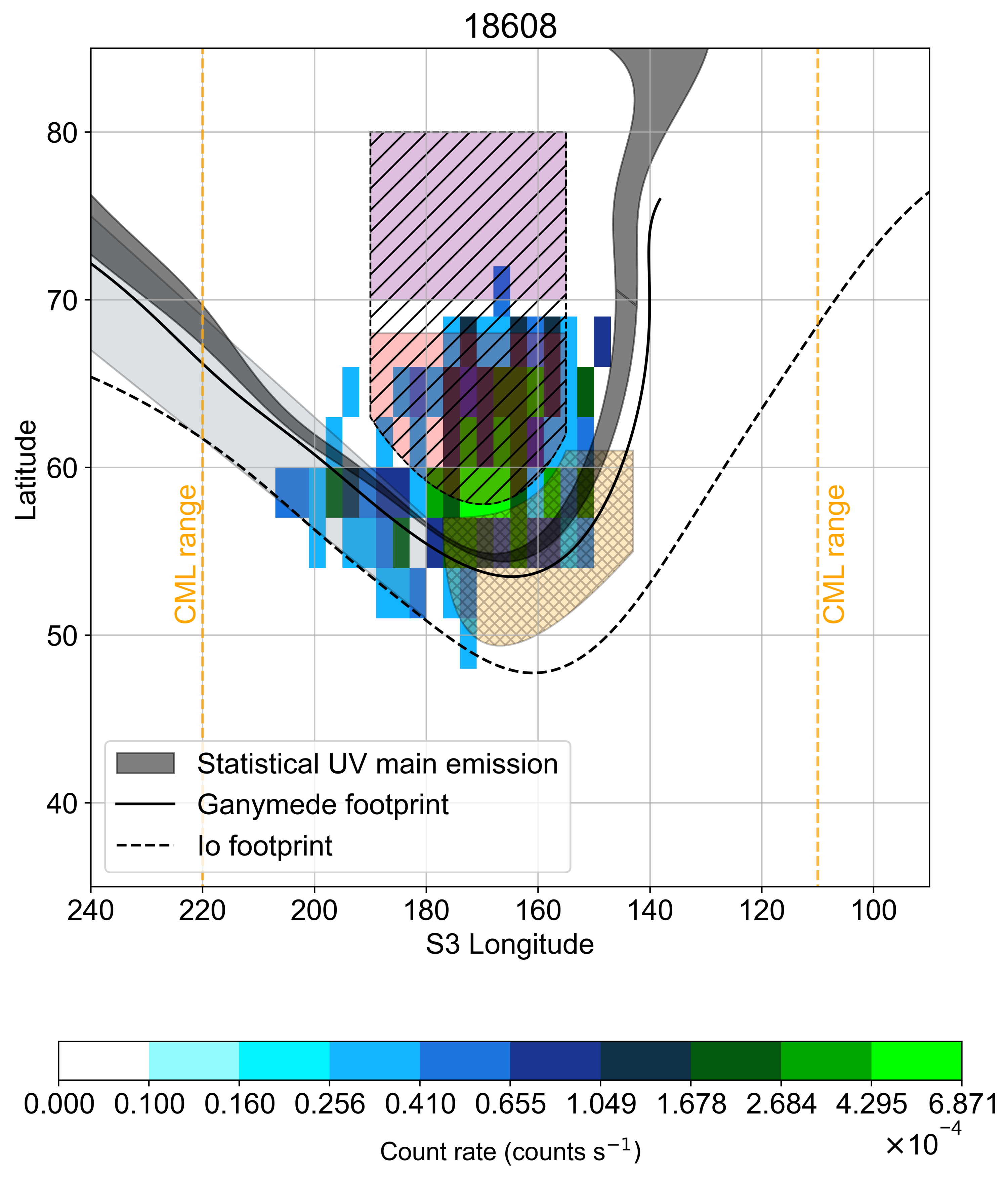

18608
Latitude
80
70
60
50
40
CML range
CML range
240
220
200
180
160
140
120
100
S3 Longitude
Statistical UV main emission
Ganymede footprint
Io footprint
0.000
0.100
0.160
0.256
0.410
0.655
1.049
1.678
2.684
4.295
6.871
Count rate (counts s^{-1})
$\times 10^{-4}$

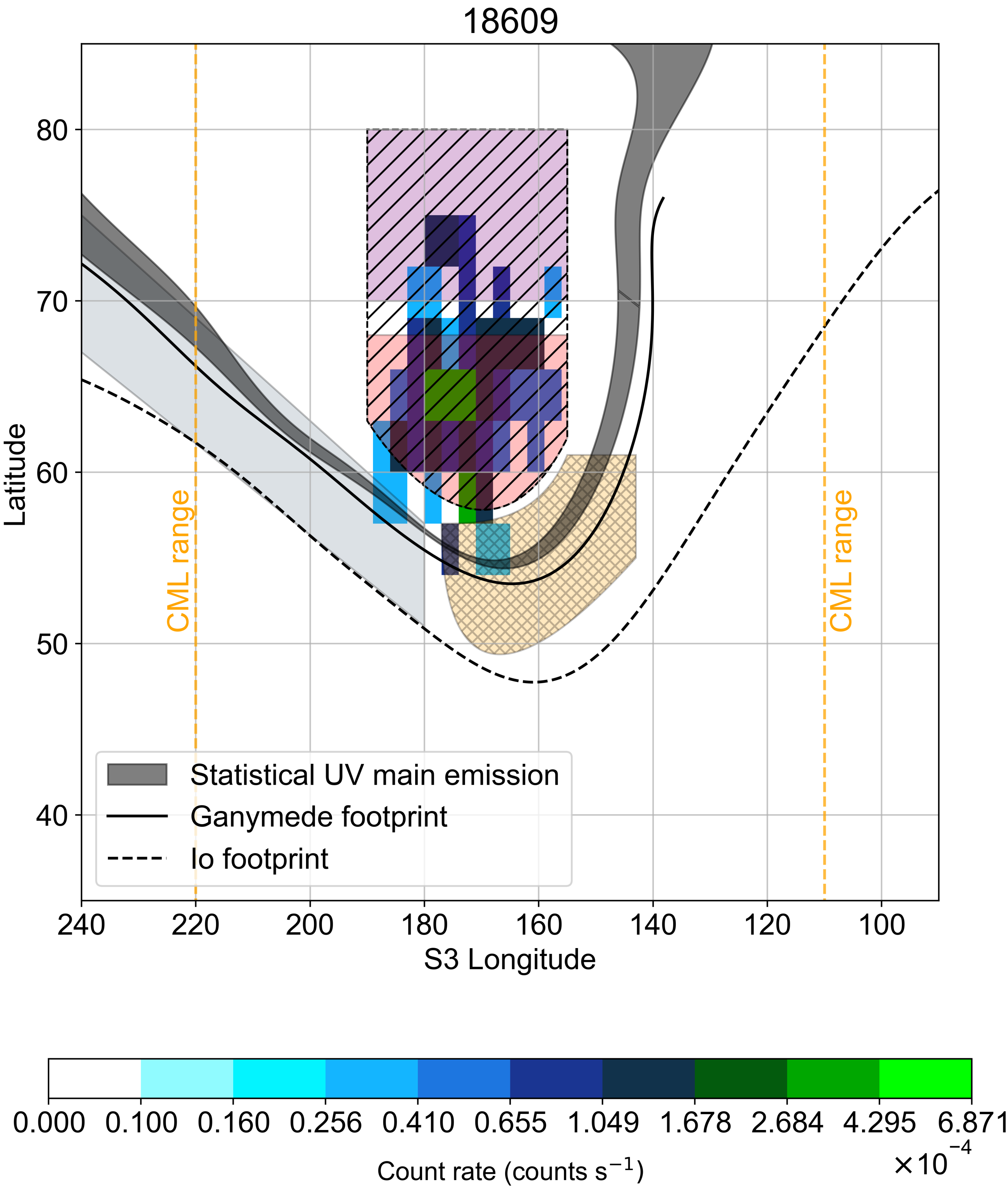
18609
Latitude
S3 Longitude
CML range
CML range
Statistical UV main emission
Ganymede footprint
Io footprint
80
70
60
50
40
240
220
200
180
160
140
120
100
0.000
0.100
0.160
0.256
0.410
0.655
1.049
1.678
2.684
4.295
6.871
$\times 10^{-4}$
Count rate (counts s^{-1})

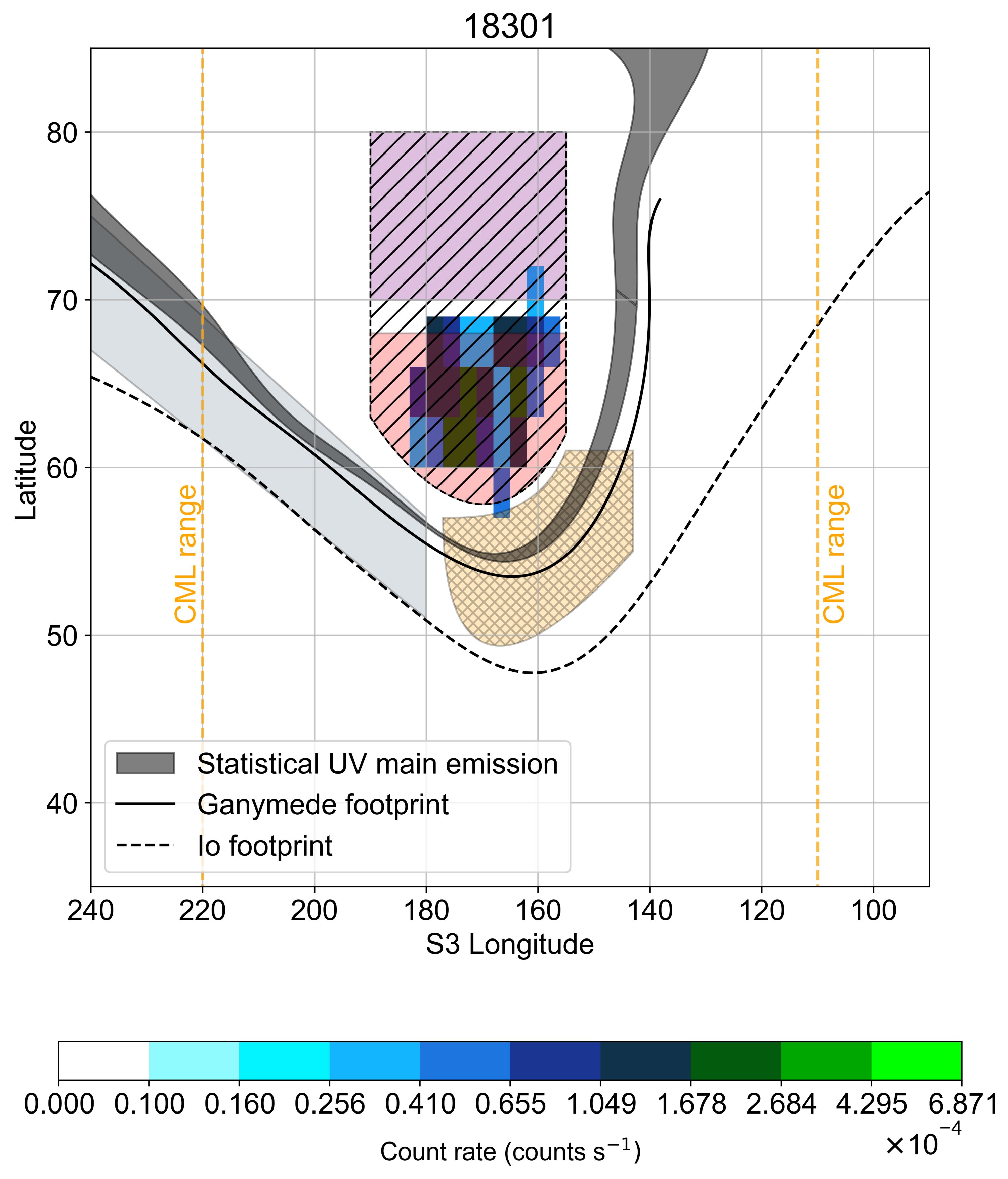
18301
Statistical UV main emission
Ganymede footprint
Io footprint
CML range
CML range
Latitude
S3 Longitude
80
70
60
50
40
240
220
200
180
160
140
120
100
0.000
0.100
0.160
0.256
0.410
0.655
1.049
1.678
2.684
4.295
6.871
×10^-4
Count rate (counts s^-1)

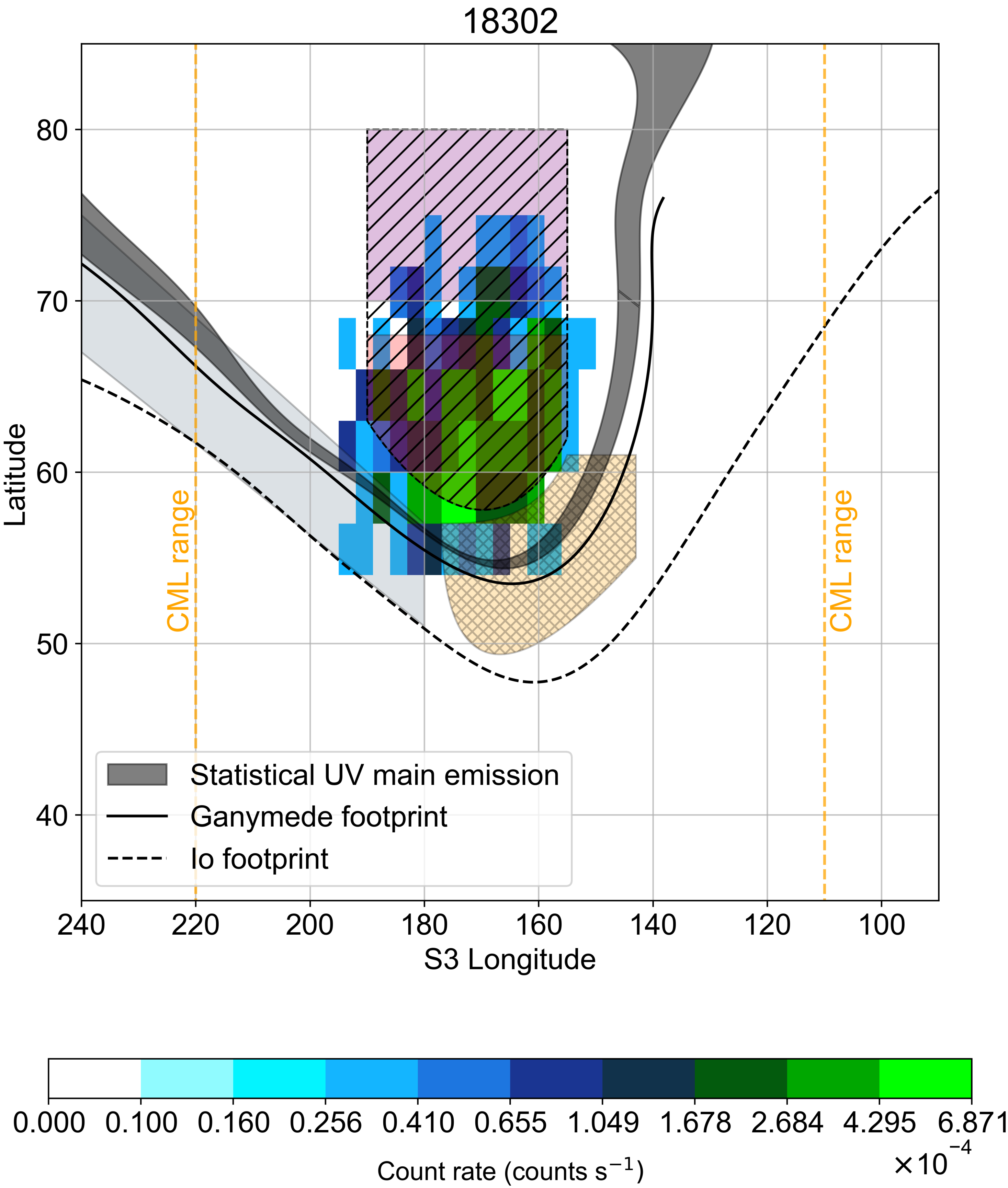
18302
Statistical UV main emission
Ganymede footprint
Io footprint
CML range
CML range
Latitude
S3 Longitude
80
70
60
50
40
240
220
200
180
160
140
120
100
0.000
0.100
0.160
0.256
0.410
0.655
1.049
1.678
2.684
4.295
6.871
$\times 10^{-4}$
Count rate (counts s^{-1})

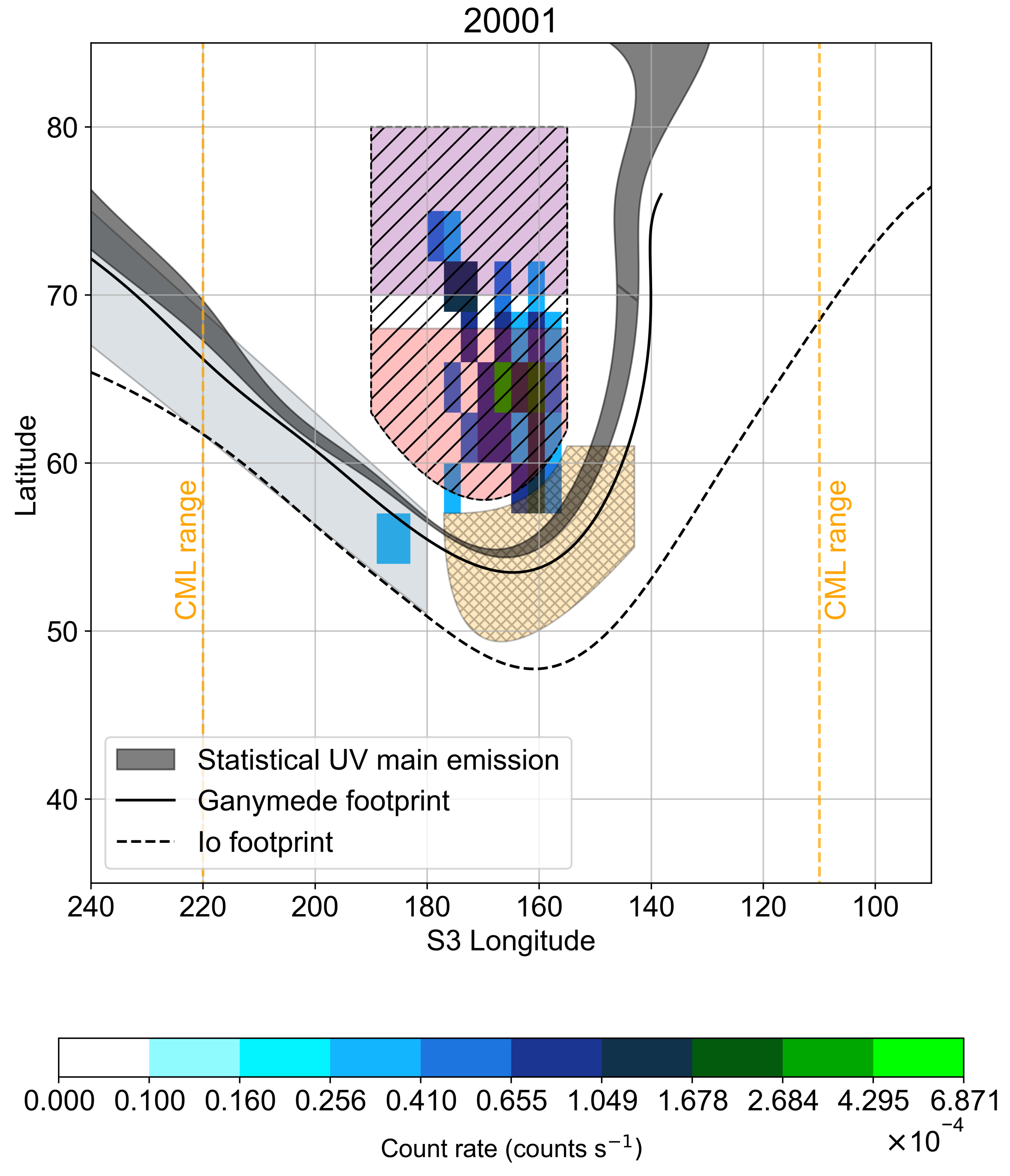

20001
Latitude
80
70
60
50
40
240
220
200
180
160
140
120
100
S3 Longitude
CML range
CML range
Statistical UV main emission
Ganymede footprint
Io footprint
0.000
0.100
0.160
0.256
0.410
0.655
1.049
1.678
2.684
4.295
6.871
×10^−4
Count rate (counts s^−1)

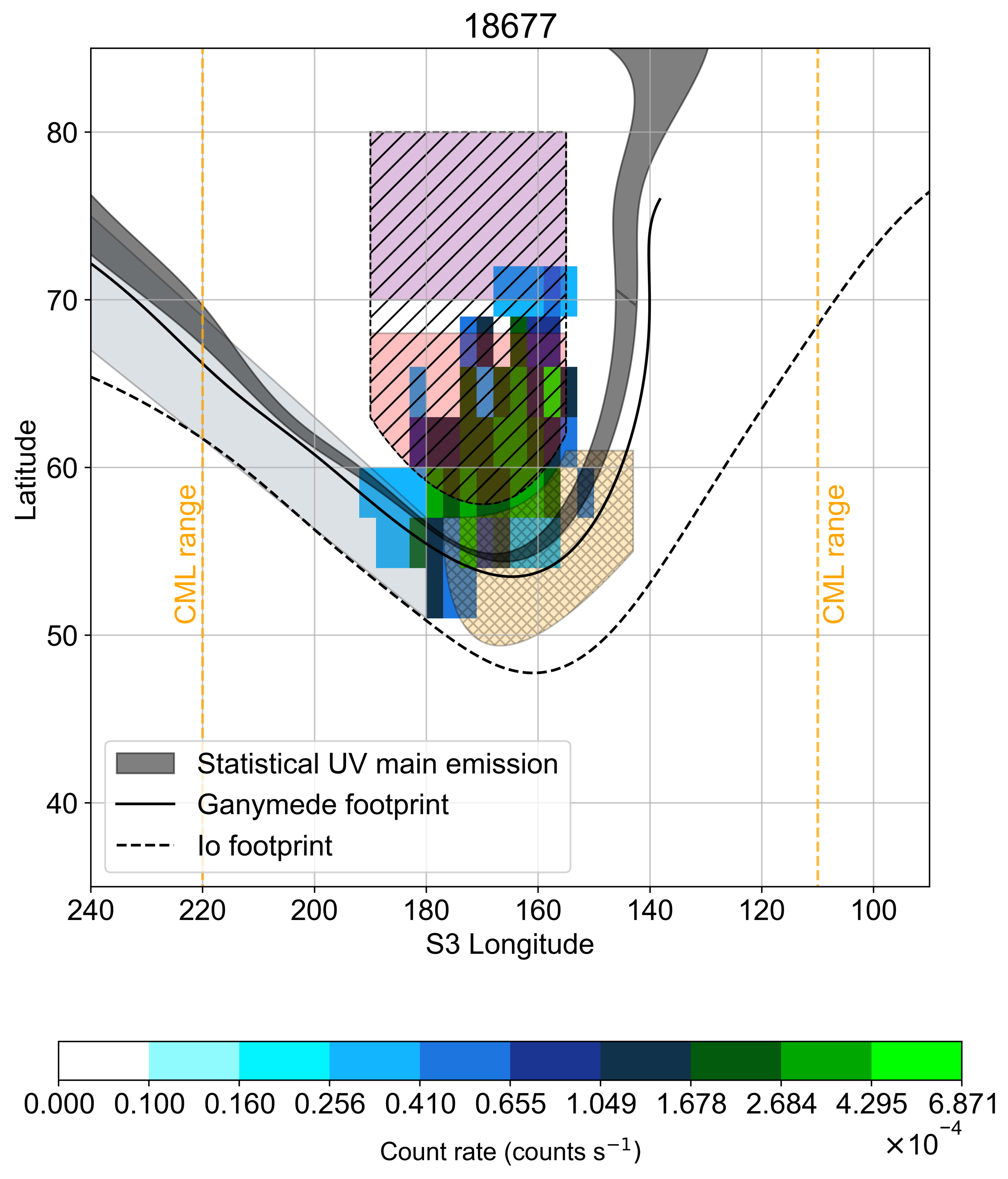
18677
Latitude
S3 Longitude
CML range
CML range
Statistical UV main emission
Ganymede footprint
Io footprint
80
70
60
50
40
240
220
200
180
160
140
120
100
0.000
0.100
0.160
0.256
0.410
0.655
1.049
1.678
2.684
4.295
6.871
$\times 10^{-4}$
Count rate (counts s^{-1})

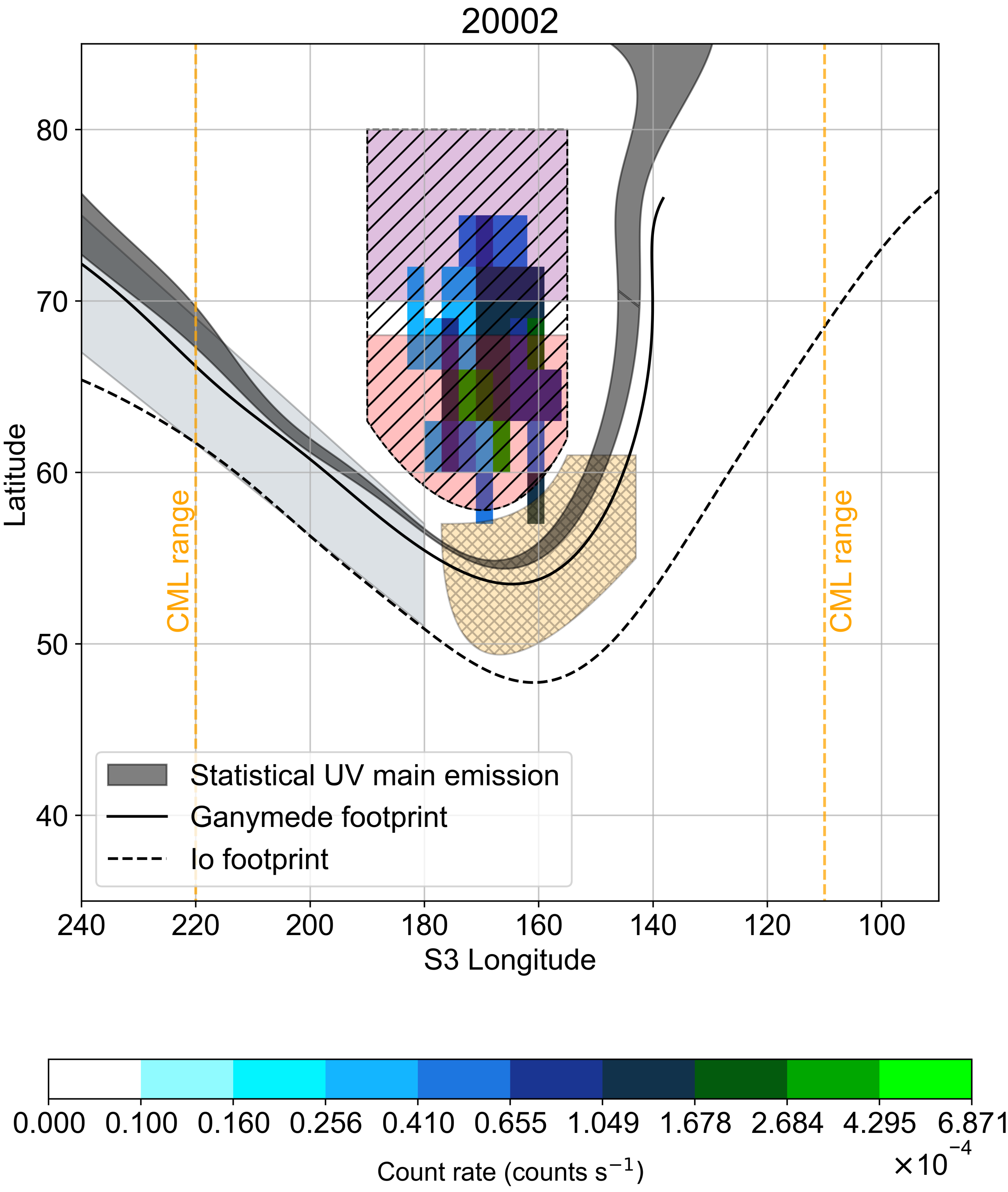

20002
Statistical UV main emission
Ganymede footprint
Io footprint
CML range
CML range
Latitude
S3 Longitude
80
70
60
50
40
240
220
200
180
160
140
120
100
0.000
0.100
0.160
0.256
0.410
0.655
1.049
1.678
2.684
4.295
6.871
×10^−4
Count rate (counts s^−1)

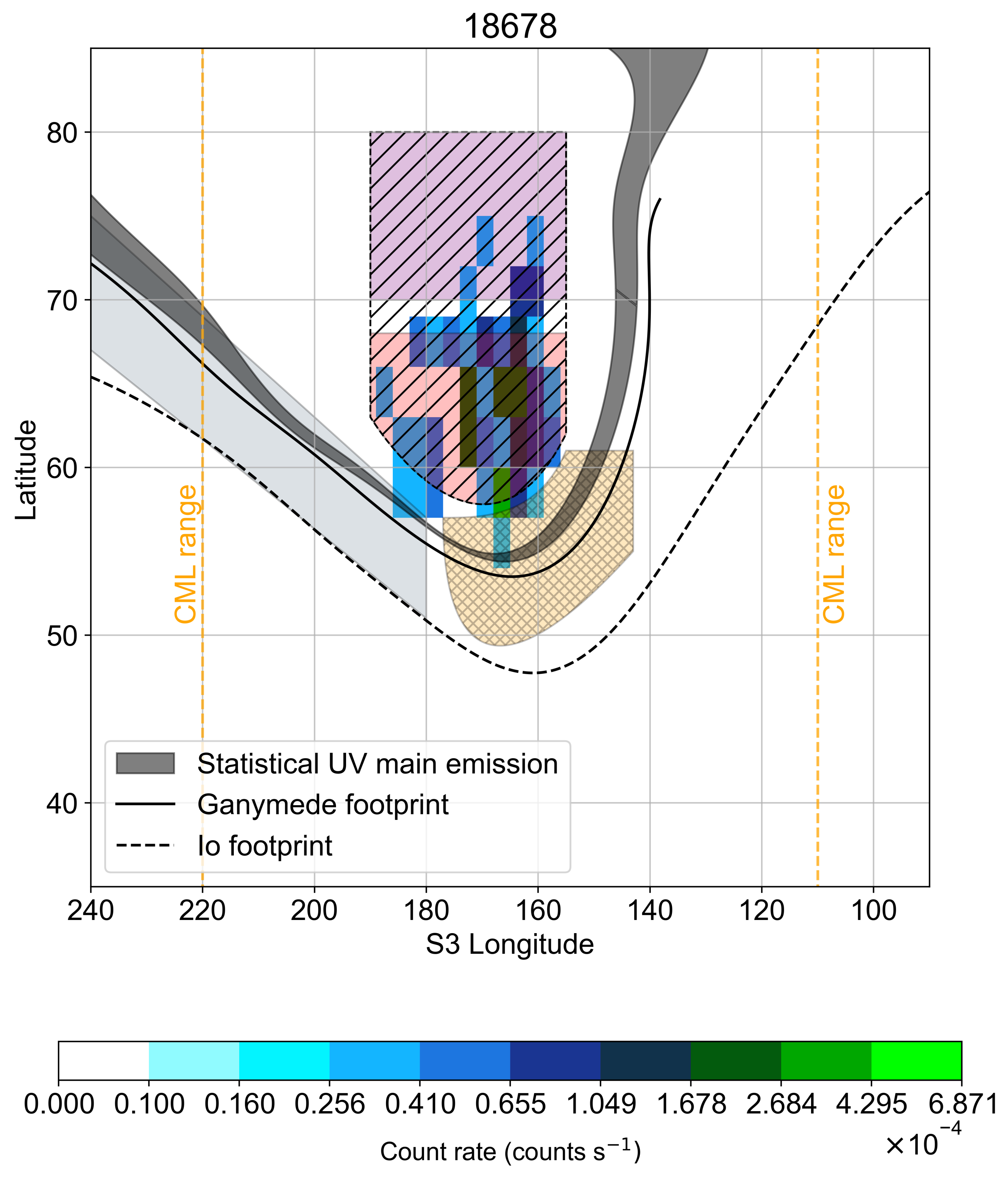

18678
Latitude
S3 Longitude
CML range
CML range
Statistical UV main emission
Ganymede footprint
Io footprint
80
70
60
50
40
240
220
200
180
160
140
120
100
0.000
0.100
0.160
0.256
0.410
0.655
1.049
1.678
2.684
4.295
6.871
×10^−4
Count rate (counts s^−1)

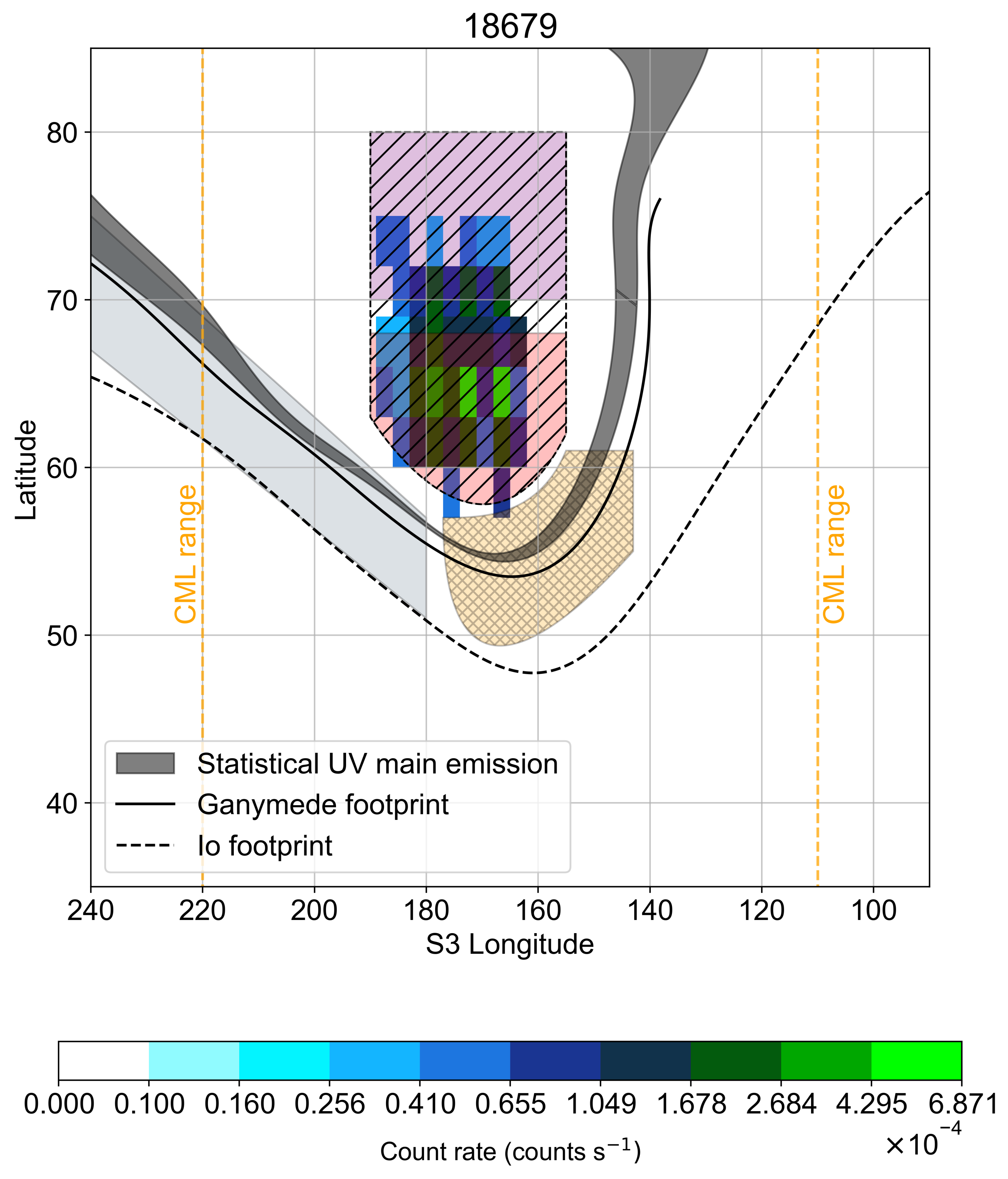
18679
Statistical UV main emission
Ganymede footprint
Io footprint
CML range
CML range
Latitude
S3 Longitude
80
70
60
50
40
240
220
200
180
160
140
120
100
0.000
0.100
0.160
0.256
0.410
0.655
1.049
1.678
2.684
4.295
6.871
×10^−4
Count rate (counts s^−1)

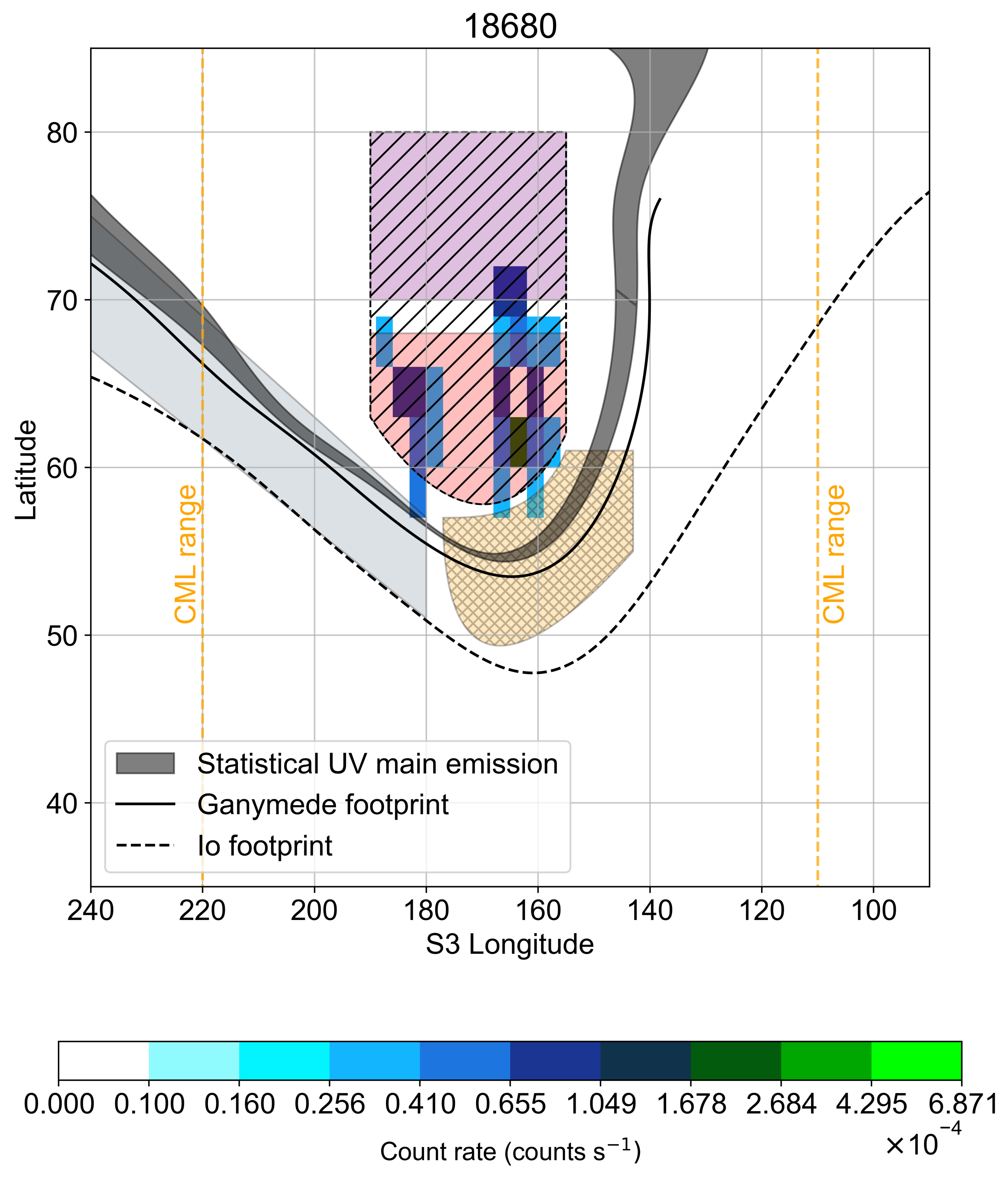
18680
Latitude
S3 Longitude
CML range
CML range
Statistical UV main emission
Ganymede footprint
Io footprint
80
70
60
50
40
240
220
200
180
160
140
120
100
0.000
0.100
0.160
0.256
0.410
0.655
1.049
1.678
2.684
4.295
6.871
×10^-4
Count rate (counts s^-1)

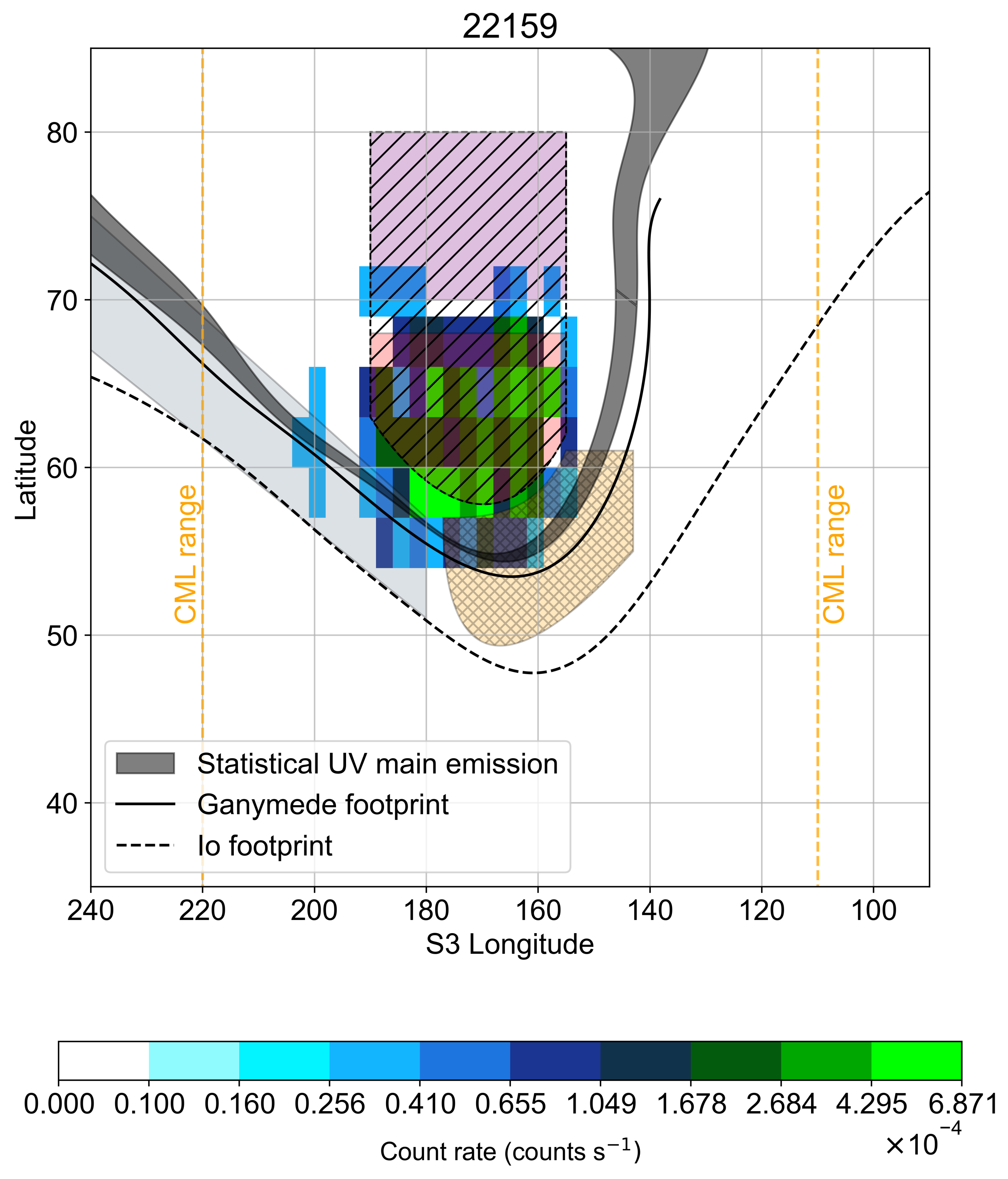
22159
Latitude
S3 Longitude
CML range
CML range
Statistical UV main emission
Ganymede footprint
Io footprint
80
70
60
50
40
240
220
200
180
160
140
120
100
0.000
0.100
0.160
0.256
0.410
0.655
1.049
1.678
2.684
4.295
6.871
$\times 10^{-4}$
Count rate (counts s^{-1})

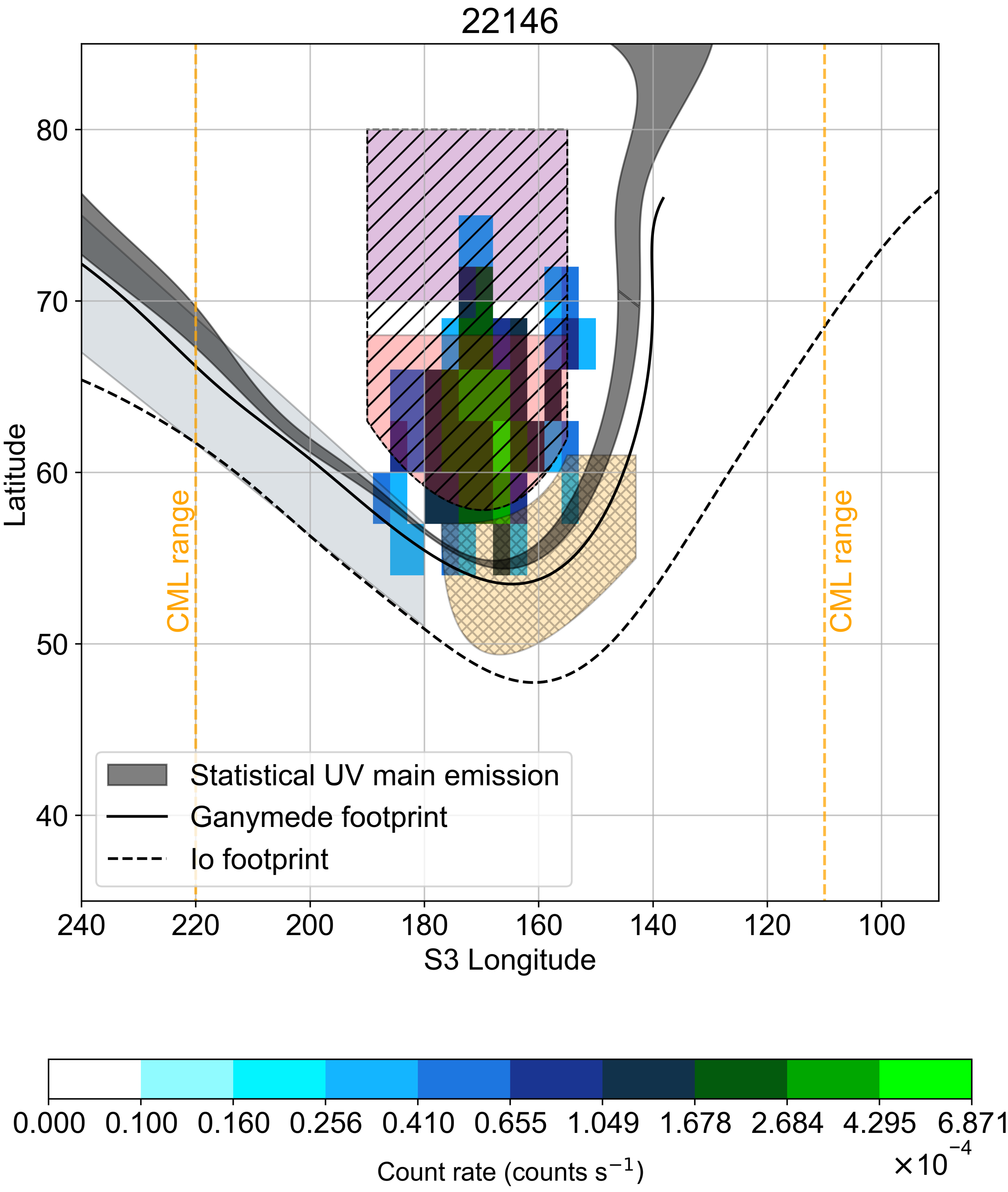

22146
80
70
60
50
40
Latitude
CML range
CML range
Statistical UV main emission
Ganymede footprint
Io footprint
240
220
200
180
160
140
120
100
S3 Longitude
0.000
0.100
0.160
0.256
0.410
0.655
1.049
1.678
2.684
4.295
6.871
$\times 10^{-4}$
Count rate (counts s^{-1})

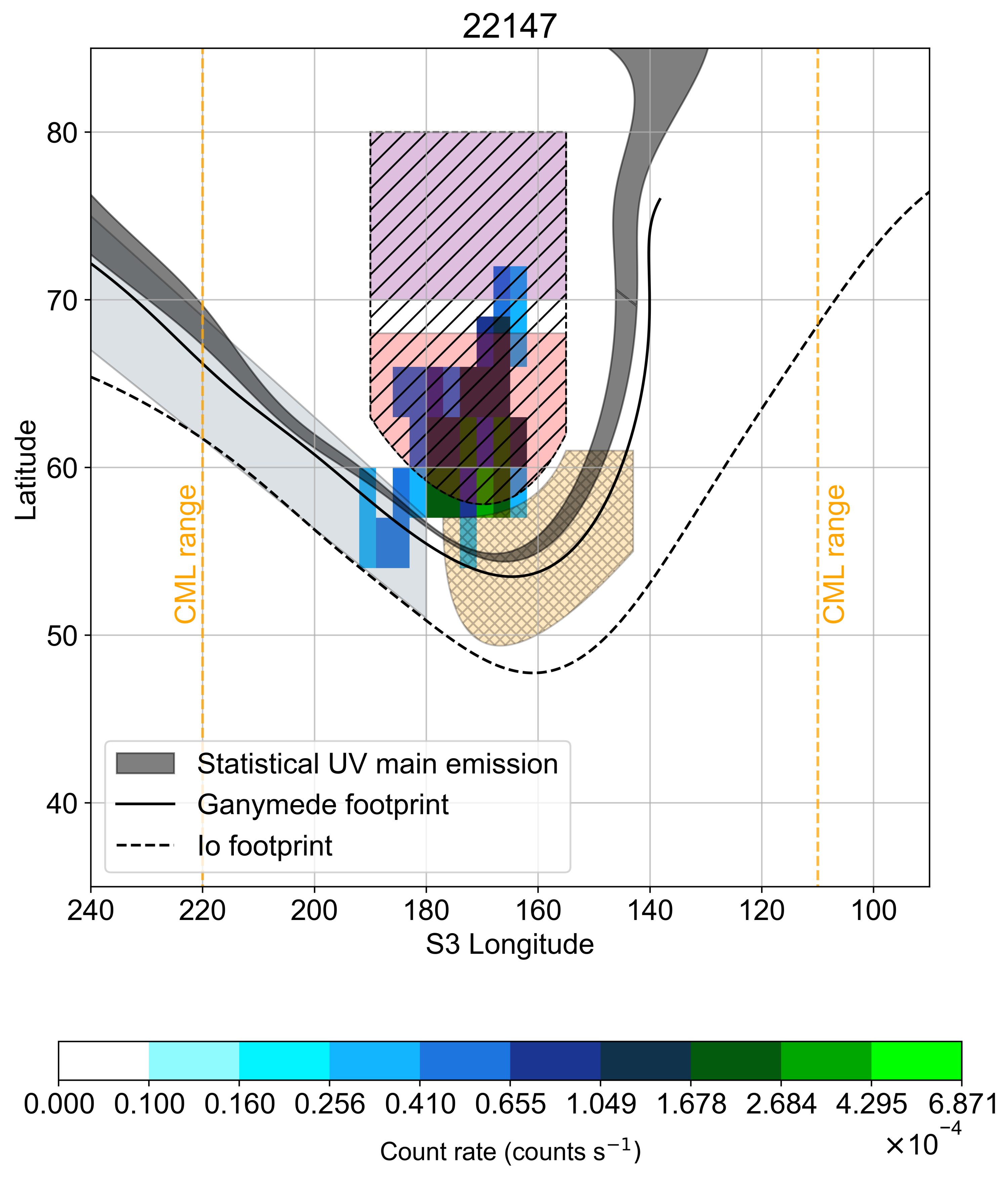

22147
80
70
60
50
40
Latitude
CML range
CML range
Statistical UV main emission
Ganymede footprint
Io footprint
240
220
200
180
160
140
120
100
S3 Longitude
0.000
0.100
0.160
0.256
0.410
0.655
1.049
1.678
2.684
4.295
6.871
$\times 10^{-4}$
Count rate (counts s^{-1})

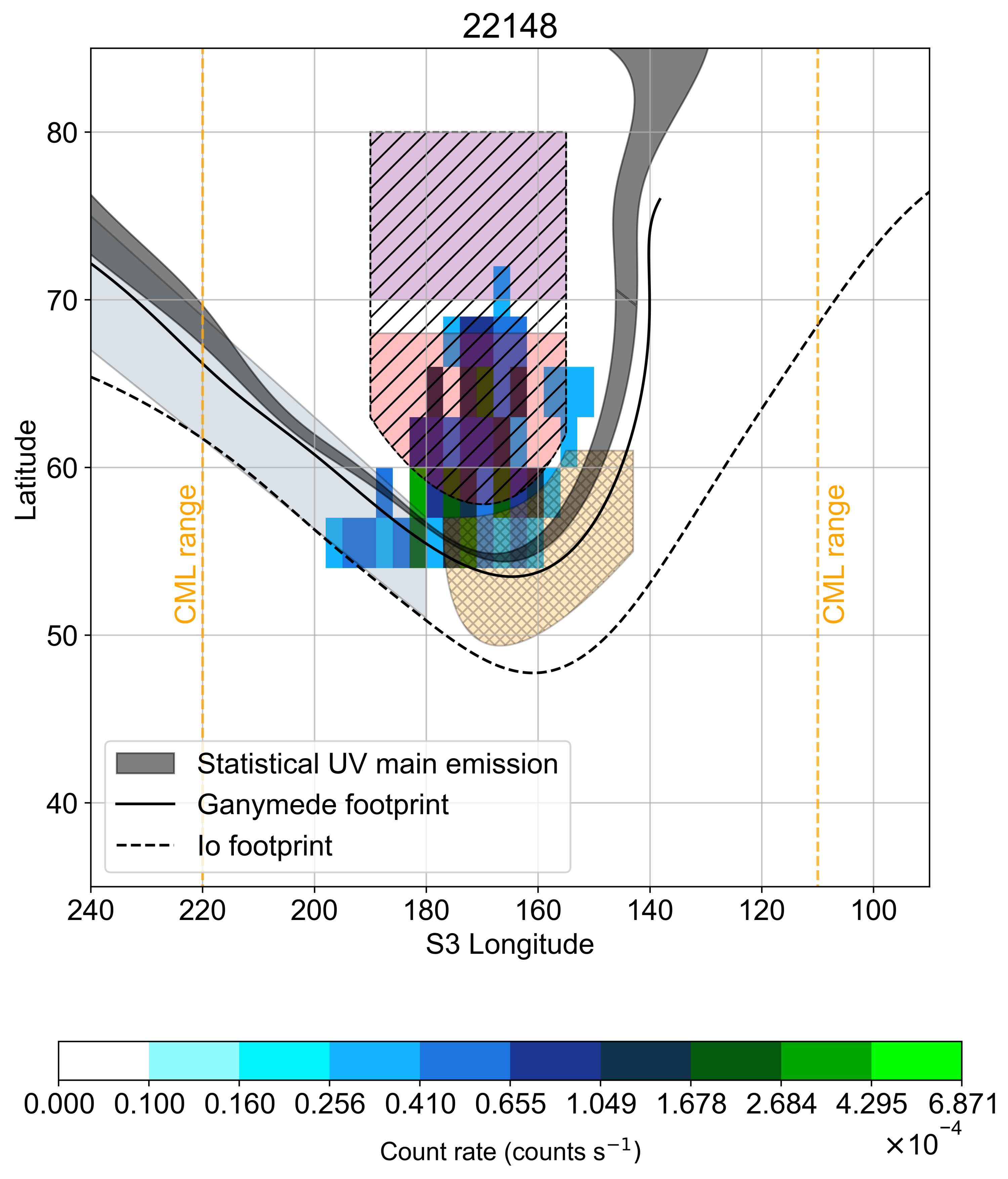

22148
Latitude
S3 Longitude
CML range
CML range
Statistical UV main emission
Ganymede footprint
Io footprint
80
70
60
50
40
240
220
200
180
160
140
120
100
0.000
0.100
0.160
0.256
0.410
0.655
1.049
1.678
2.684
4.295
6.871
$\times 10^{-4}$
Count rate (counts s^{-1})

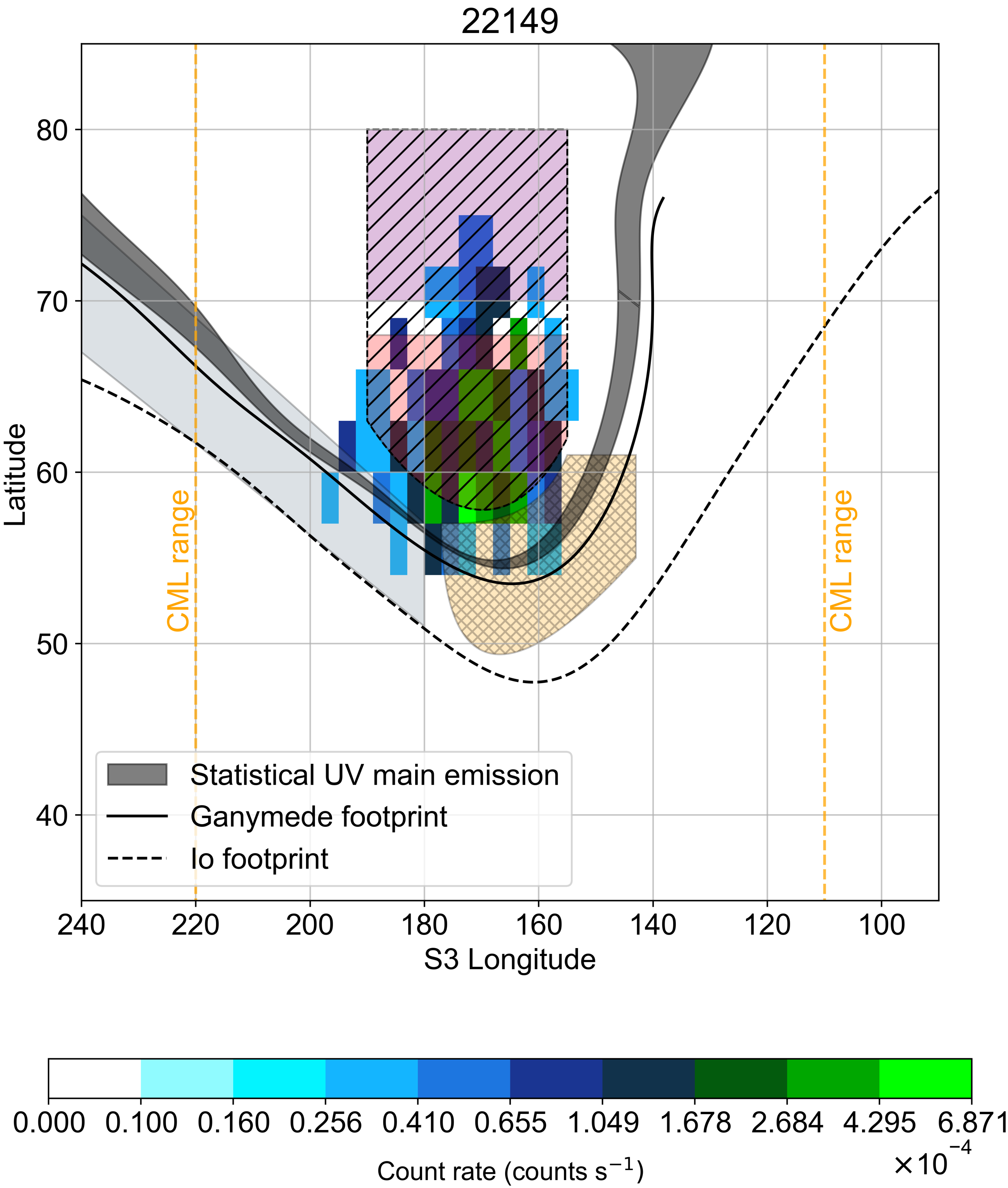

22149
80
70
60
50
40
Latitude
CML range
CML range
Statistical UV main emission
Ganymede footprint
Io footprint
240
220
200
180
160
140
120
100
S3 Longitude
0.000
0.100
0.160
0.256
0.410
0.655
1.049
1.678
2.684
4.295
6.871
×10^−4
Count rate (counts s^−1)

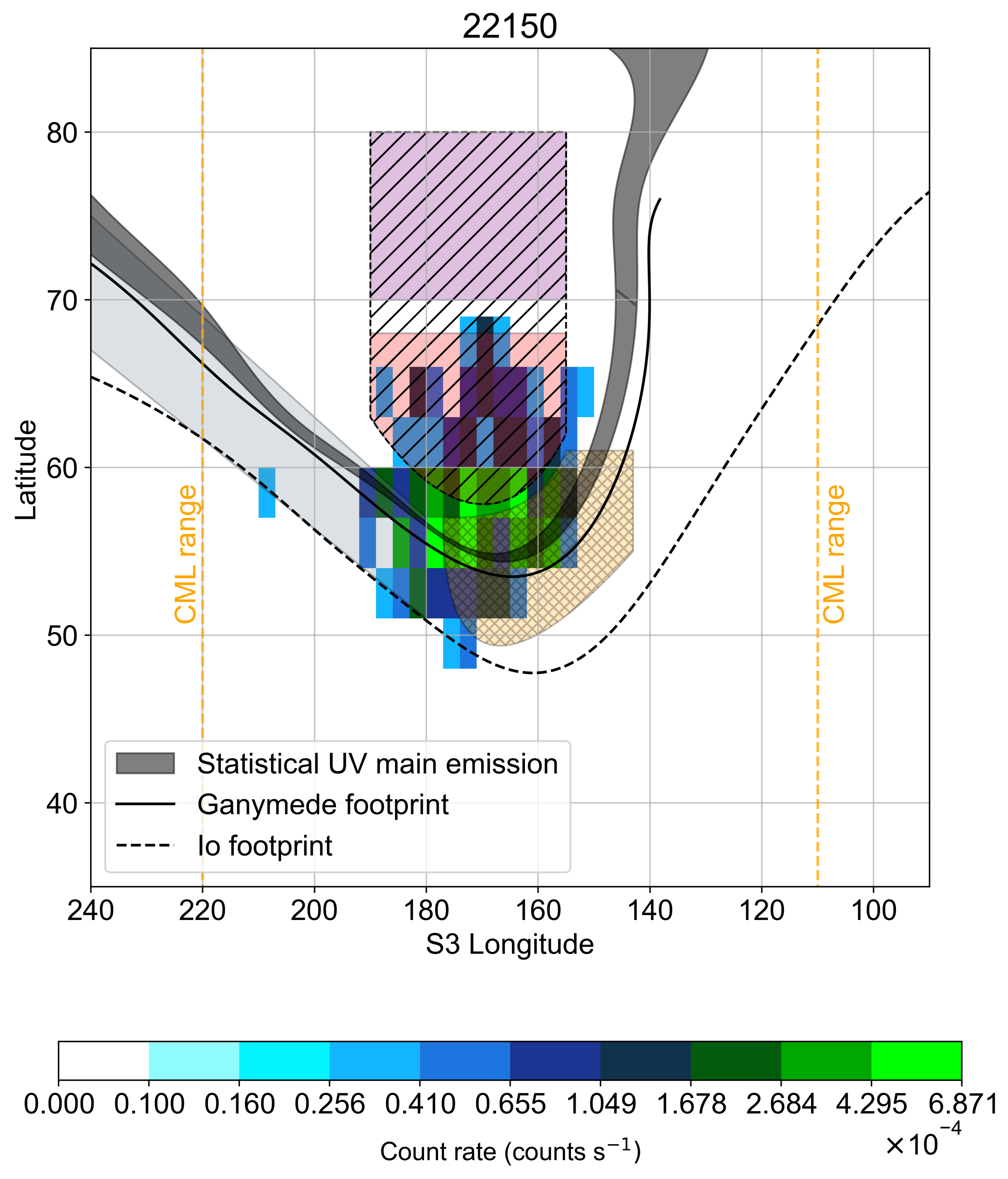
22150
Latitude
S3 Longitude
CML range
CML range
Statistical UV main emission
Ganymede footprint
Io footprint
80
70
60
50
40
240
220
200
180
160
140
120
100
0.000
0.100
0.160
0.256
0.410
0.655
1.049
1.678
2.684
4.295
6.871
$\times 10^{-4}$
Count rate (counts s^{-1})

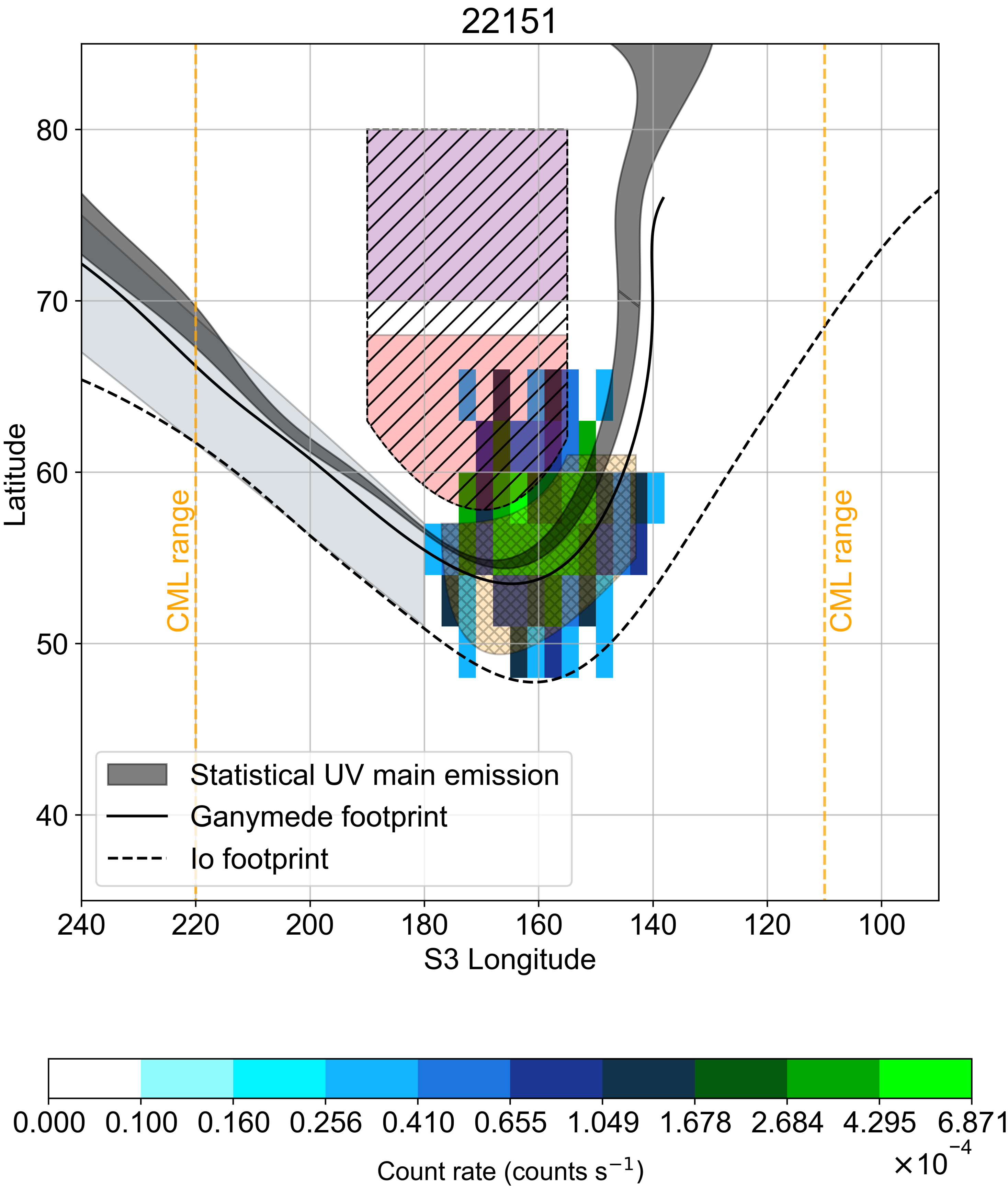

22151
Latitude
S3 Longitude
CML range
CML range
Statistical UV main emission
Ganymede footprint
Io footprint
80
70
60
50
40
240
220
200
180
160
140
120
100
0.000
0.100
0.160
0.256
0.410
0.655
1.049
1.678
2.684
4.295
6.871
$\times 10^{-4}$
Count rate (counts s^{-1})

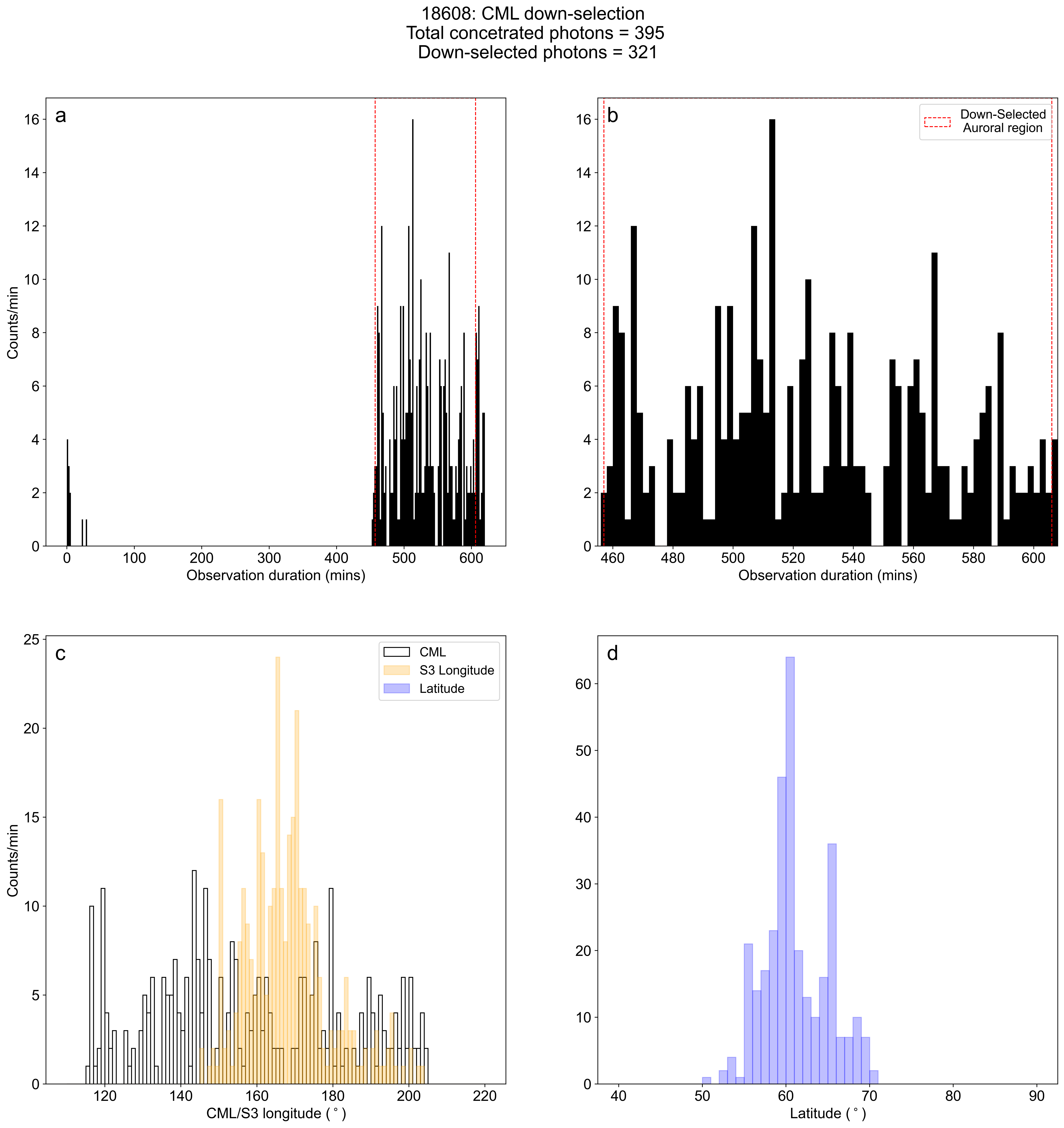

18608: CML down-selection
Total concetrated photons = 395
Down-selected photons = 321
a
b
Down-Selected
Auroral region
Counts/min
Observation duration (mins)
c
d
CML
S3 Longitude
Latitude
CML/S3 longitude ($^\circ$)
Latitude ($^\circ$)

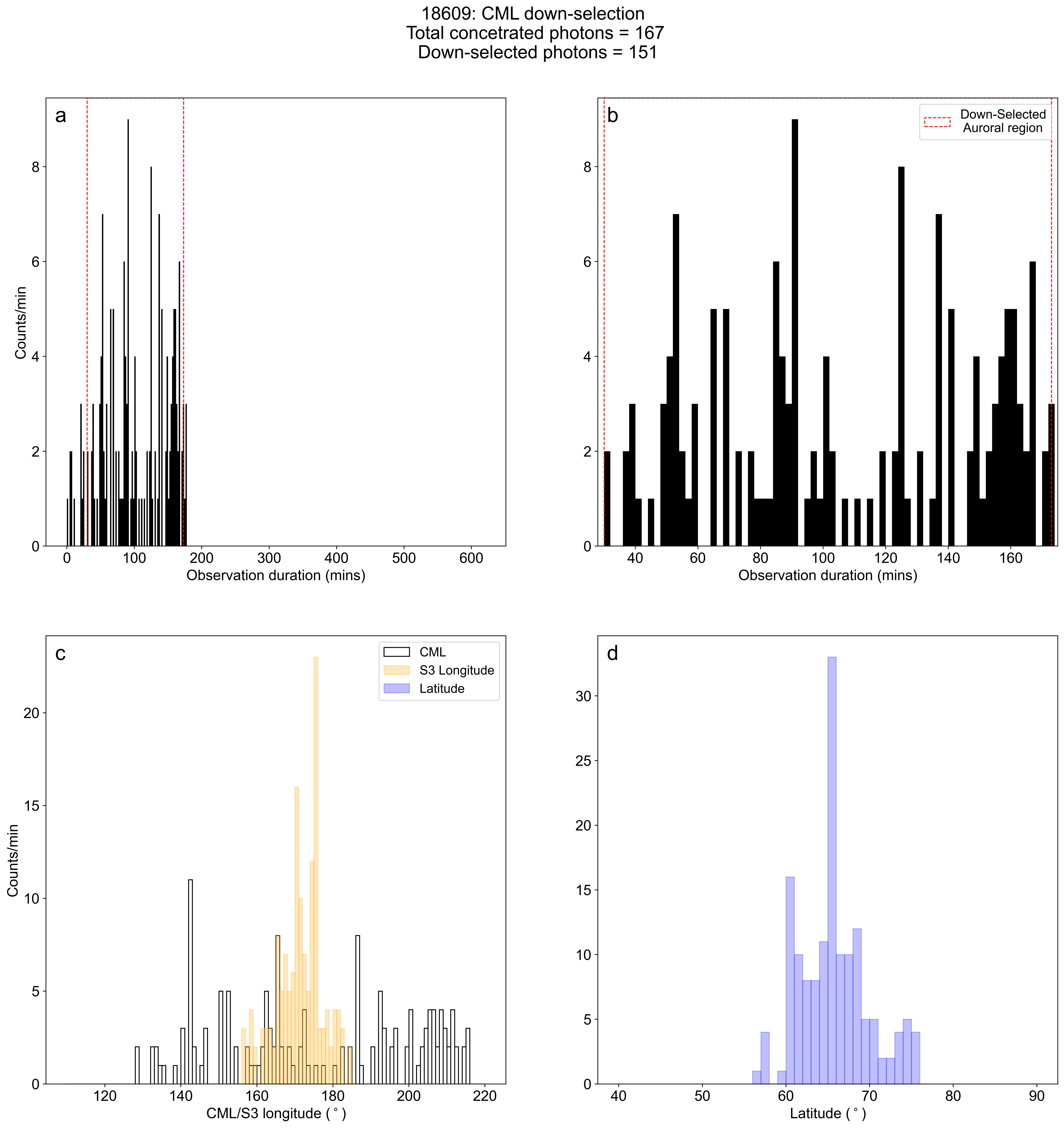

18609: CML down-selection
Total concetrated photons = 167
Down-selected photons = 151
a
b
Down-Selected
Auroral region
Counts/min
Observation duration (mins)
c
d
CML
S3 Longitude
Latitude
CML/S3 longitude ($^\circ$)
Latitude ($^\circ$)

18301: CML down-selection
Total concetrated photons = 86
Down-selected photons = 84

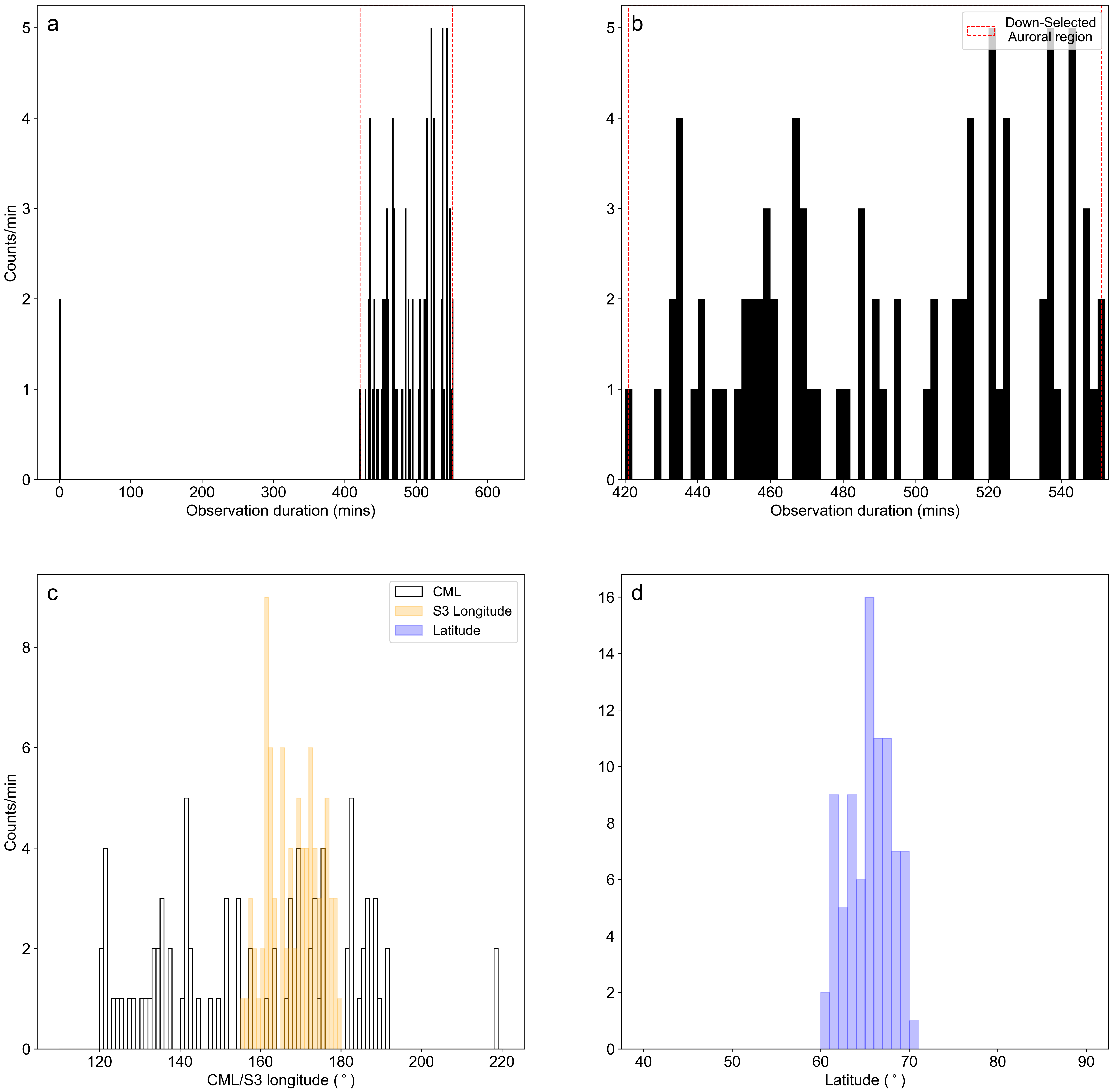

18302: CML down-selection
Total concetrated photons = 438
Down-selected photons = 389

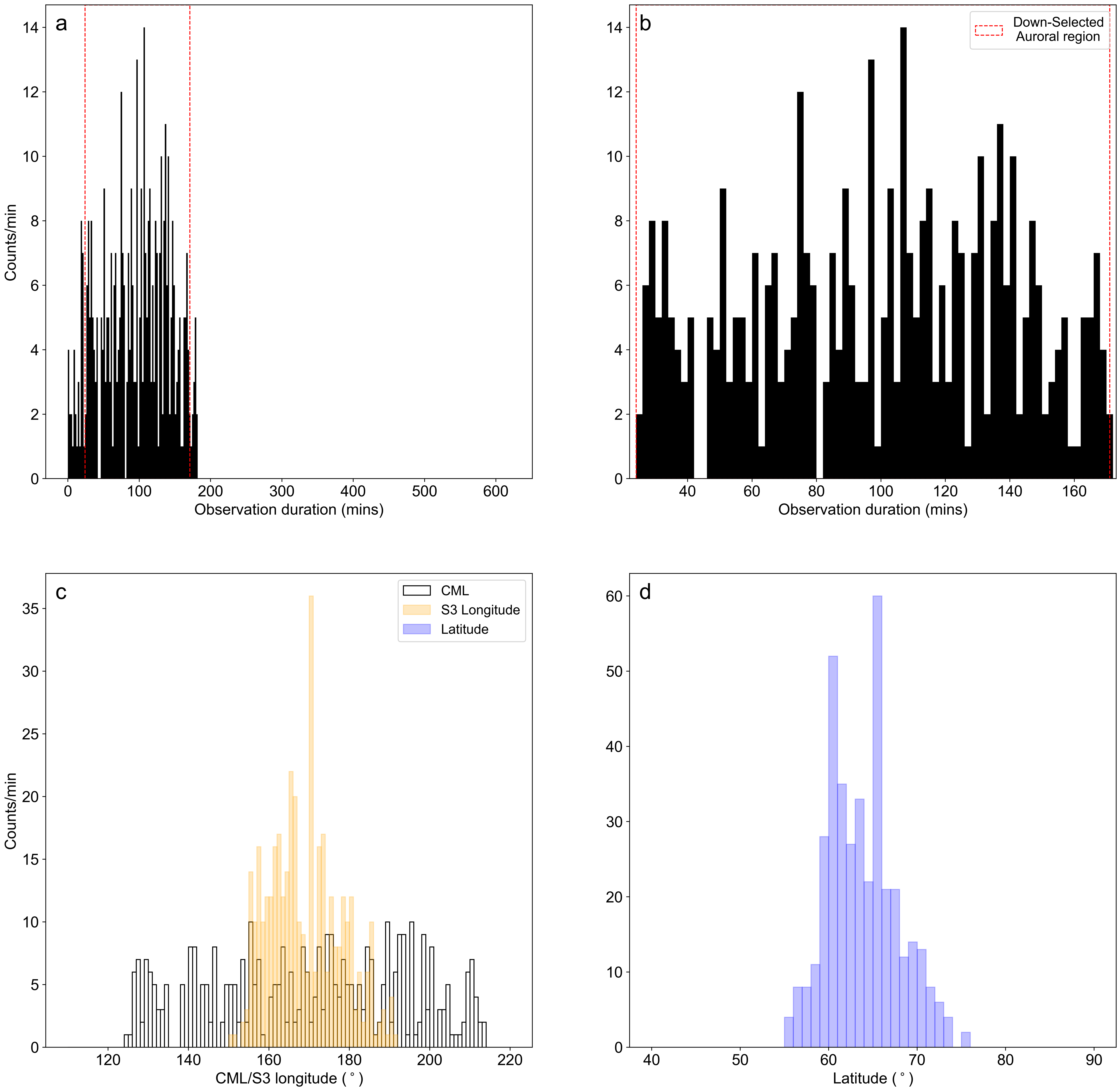

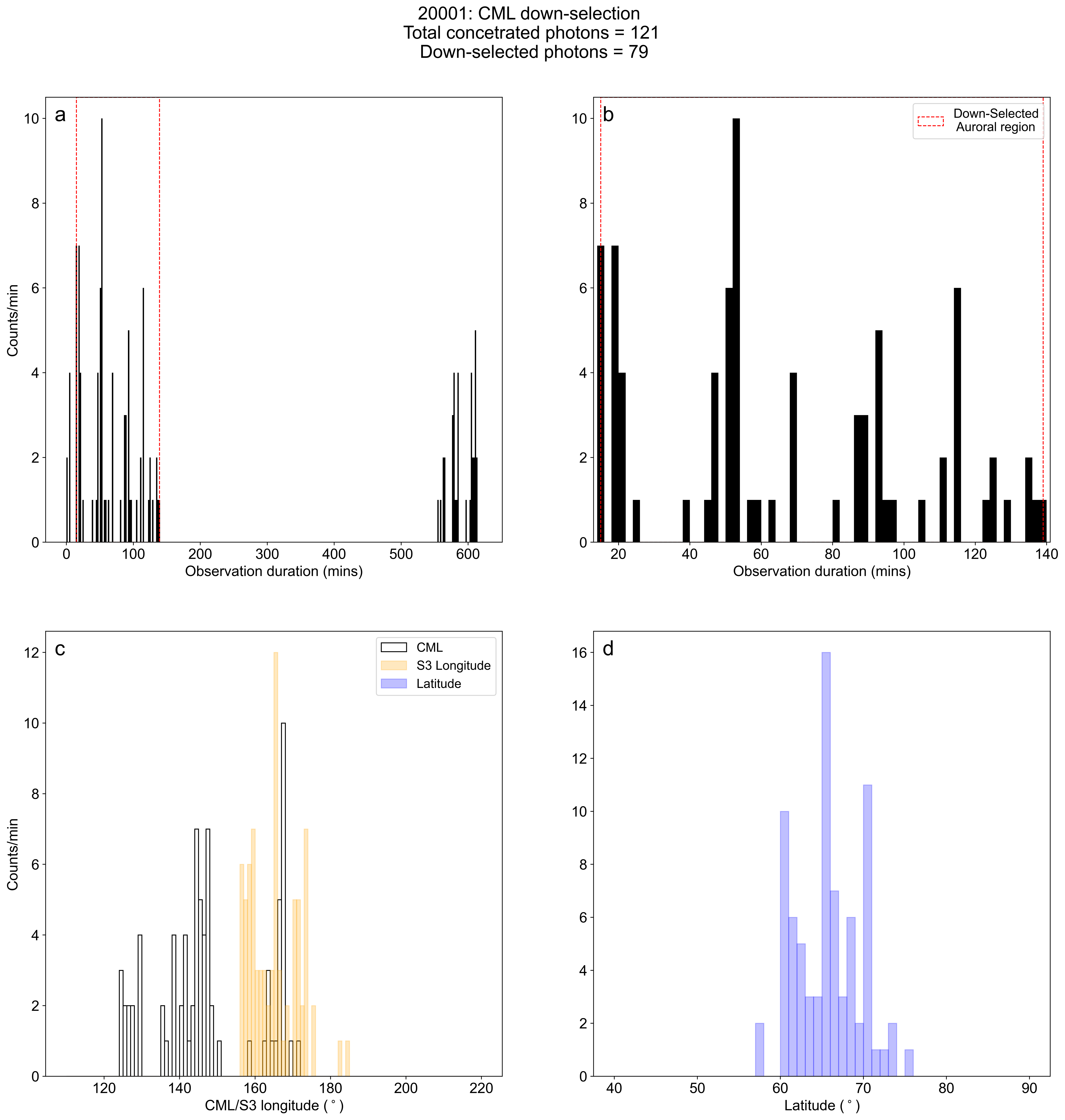

20001: CML down-selection
Total concetrated photons = 121
Down-selected photons = 79
a
b
c
d
Counts/min
Observation duration (mins)
Down-Selected Auroral region
CML
S3 Longitude
Latitude
CML/S3 longitude (°)
Latitude (°)

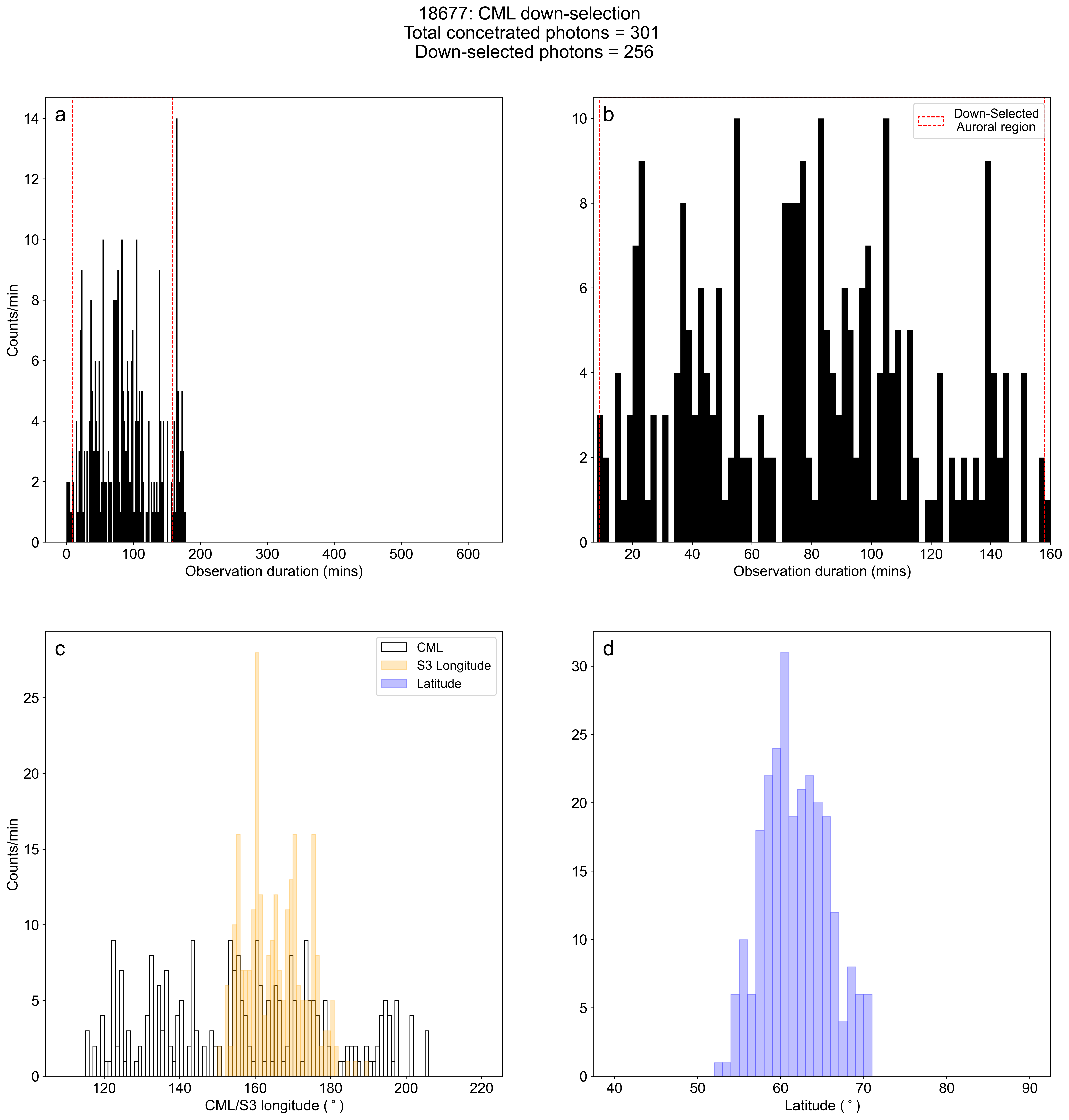
18677: CML down-selection
Total concetrated photons = 301
Down-selected photons = 256
a
Counts/min
Observation duration (mins)
b
Down-Selected
Auroral region
Observation duration (mins)
c
CML
S3 Longitude
Latitude
Counts/min
CML/S3 longitude (°)
d
Latitude (°)

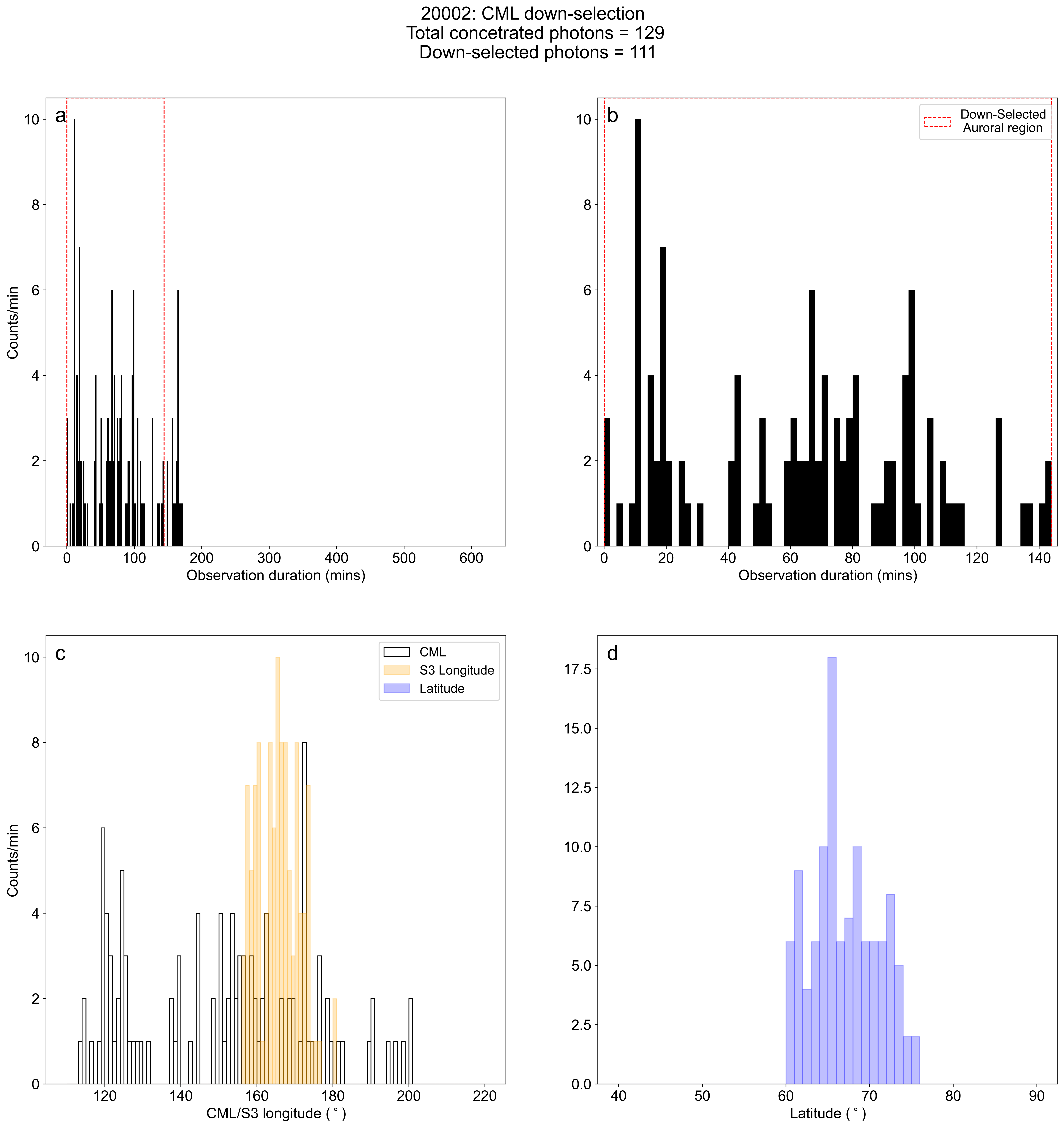
20002: CML down-selection
Total concetrated photons = 129
Down-selected photons = 111
a
b
c
d
Counts/min
Observation duration (mins)
Down-Selected
Auroral region
CML
S3 Longitude
Latitude
CML/S3 longitude (°)
Latitude (°)

18678: CML down-selection
Total concetrated photons = 198
Down-selected photons = 91

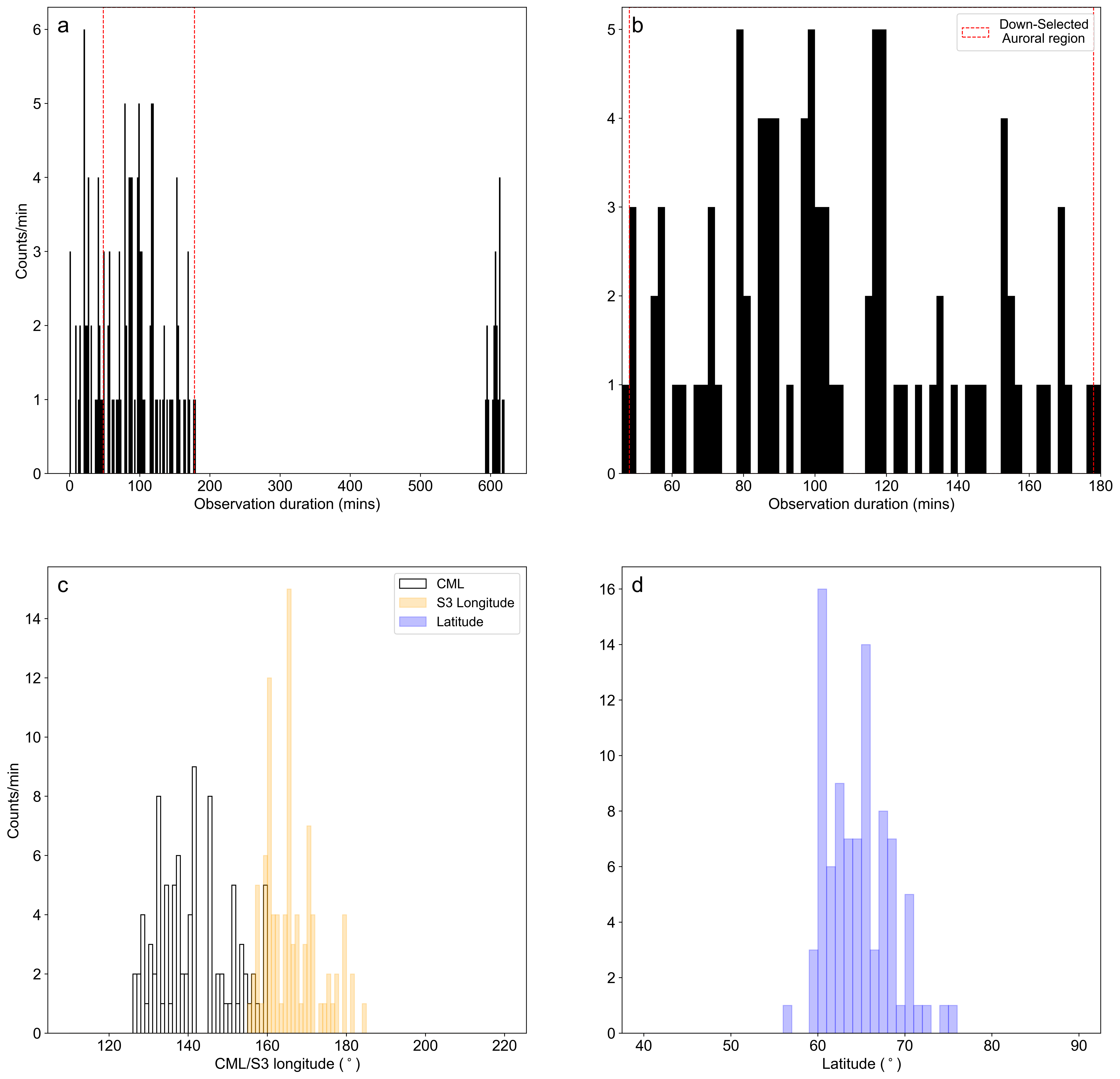

18679: CML down-selection
Total concetrated photons = 197
Down-selected photons = 184

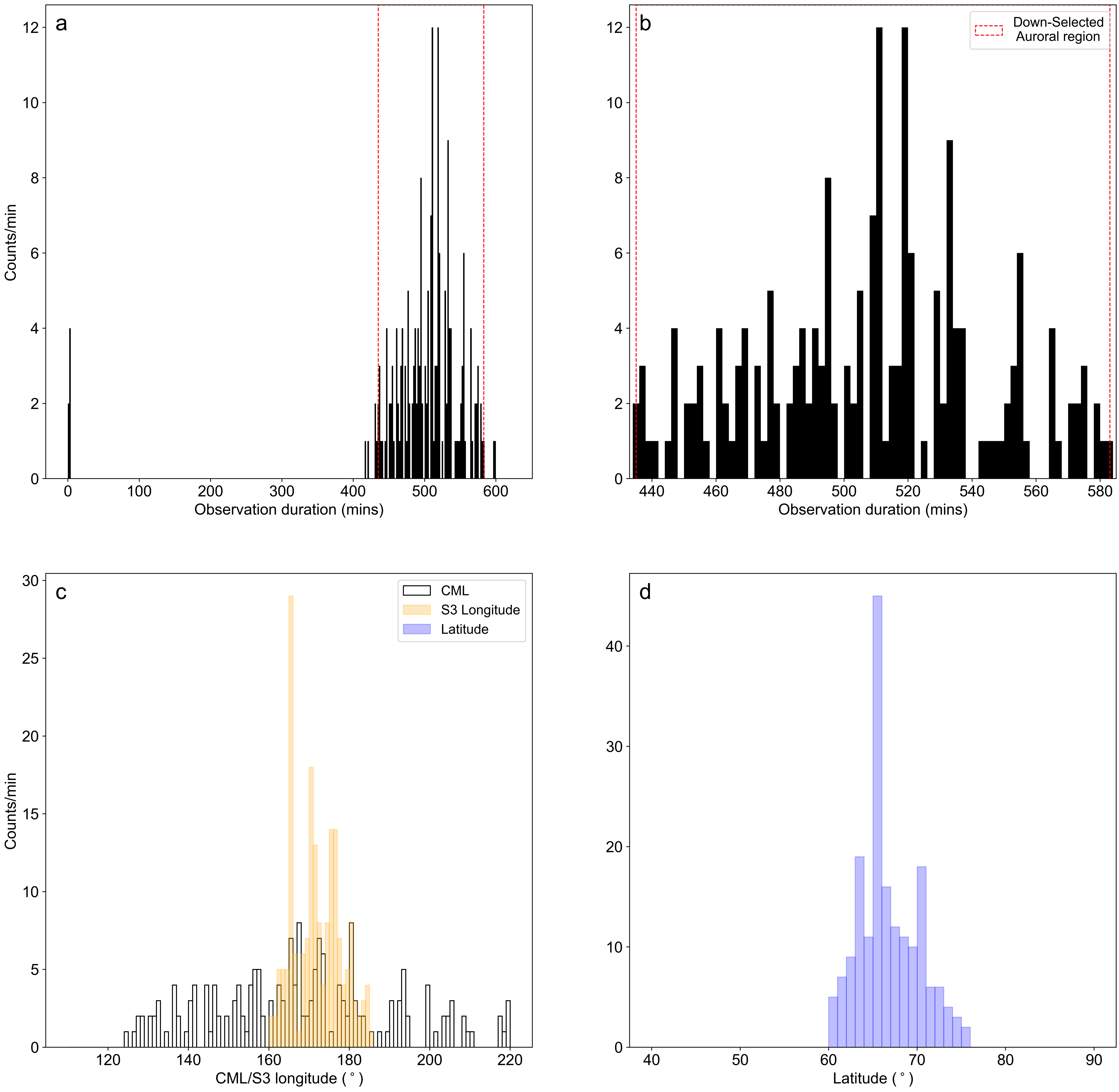

18680: CML down-selection
Total concetrated photons = 61
Down-selected photons = 43

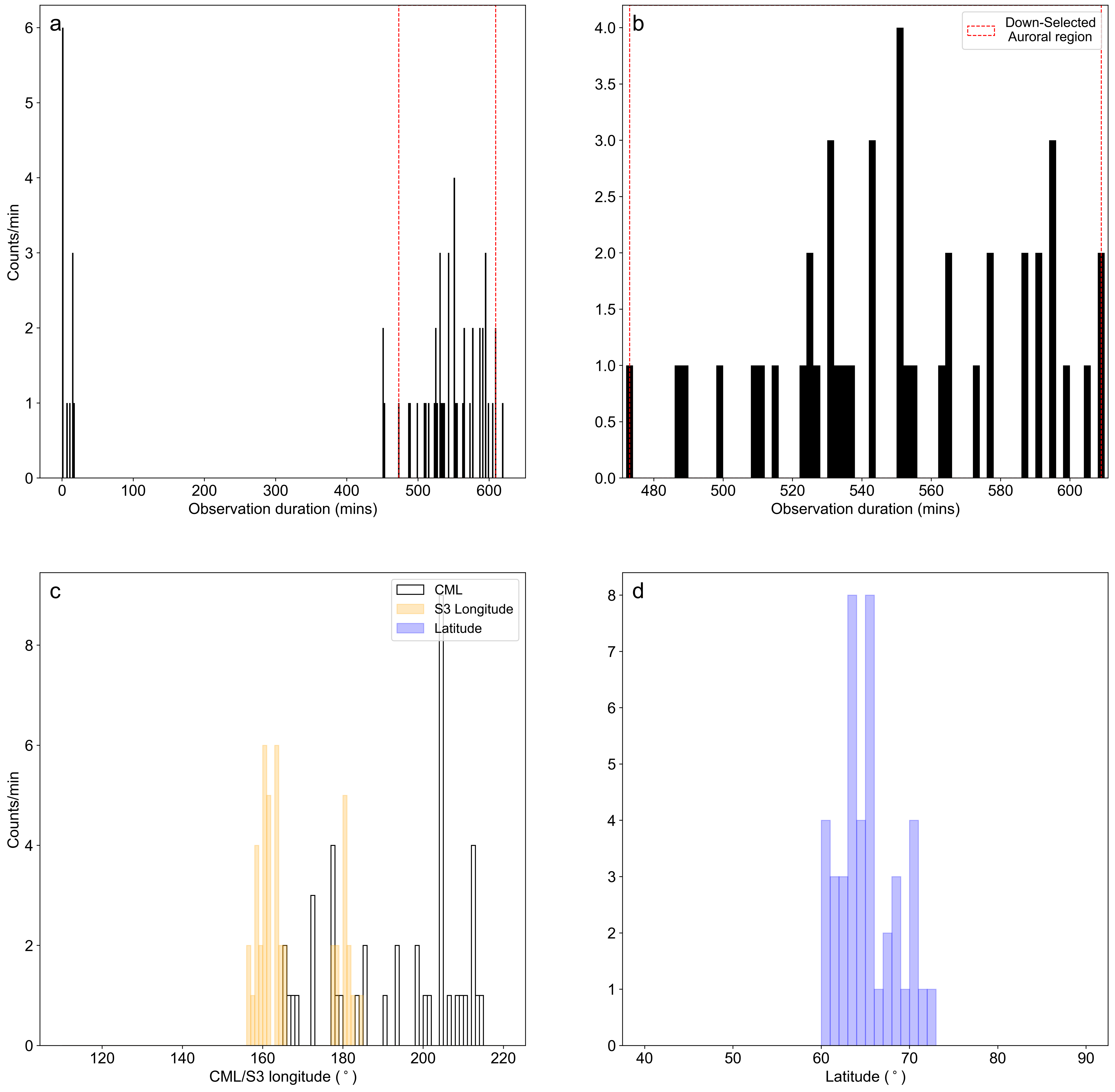

22159: CML down-selection
Total concetrated photons = 433
Down-selected photons = 386

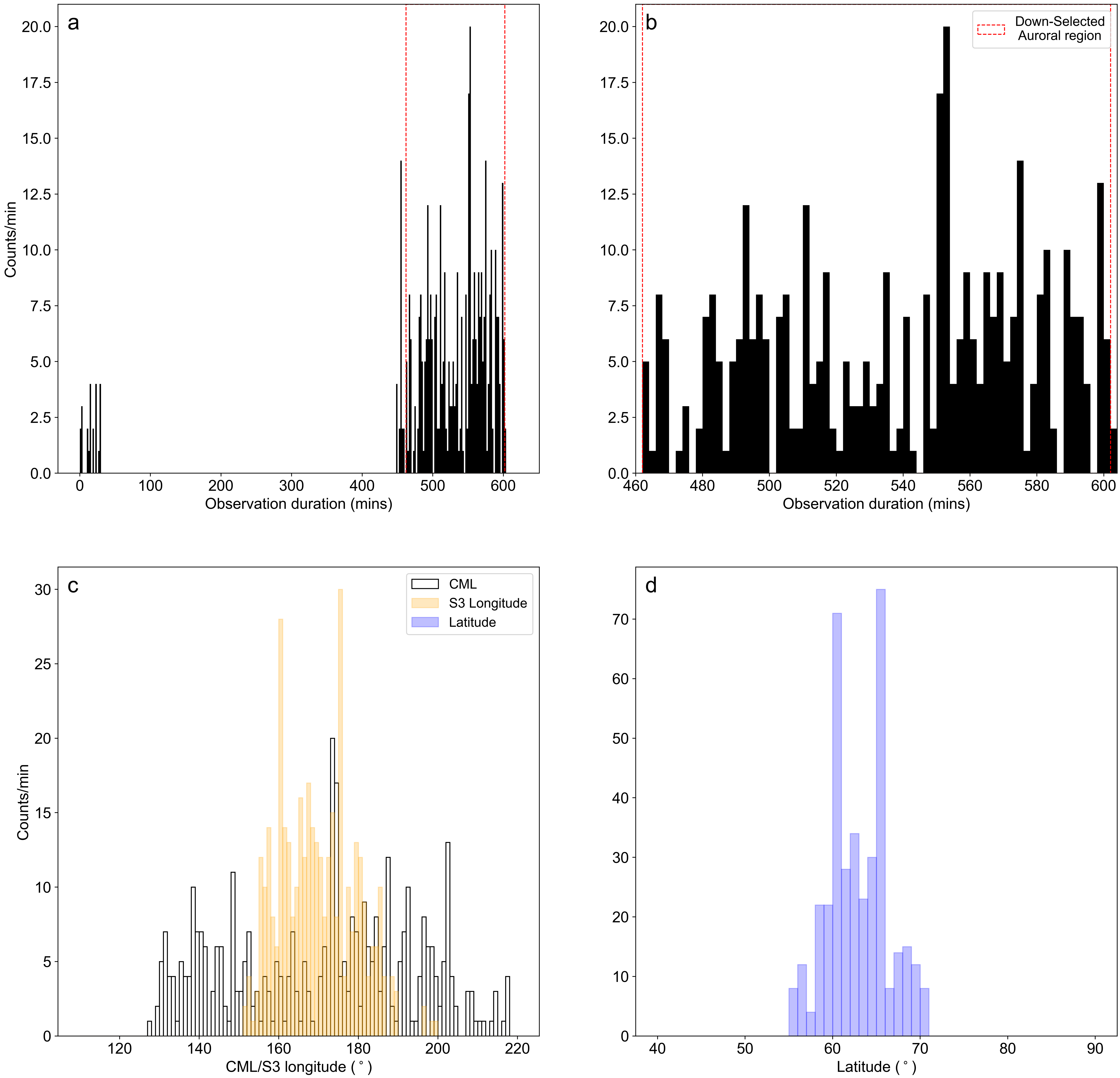

22146: CML down-selection
Total concetrated photons = 239
Down-selected photons = 215

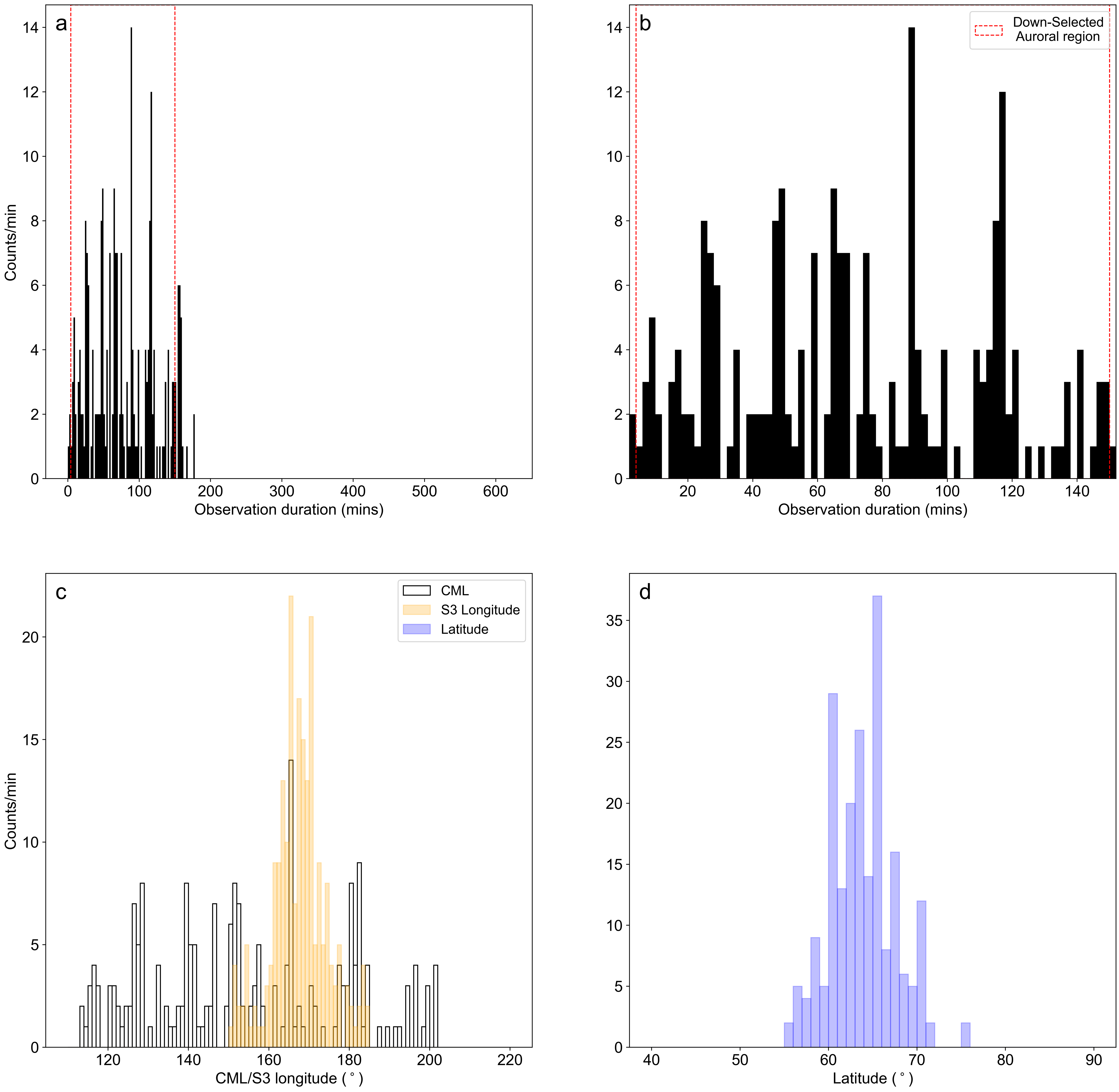

22147: CML down-selection
Total concetrated photons = 131
Down-selected photons = 110

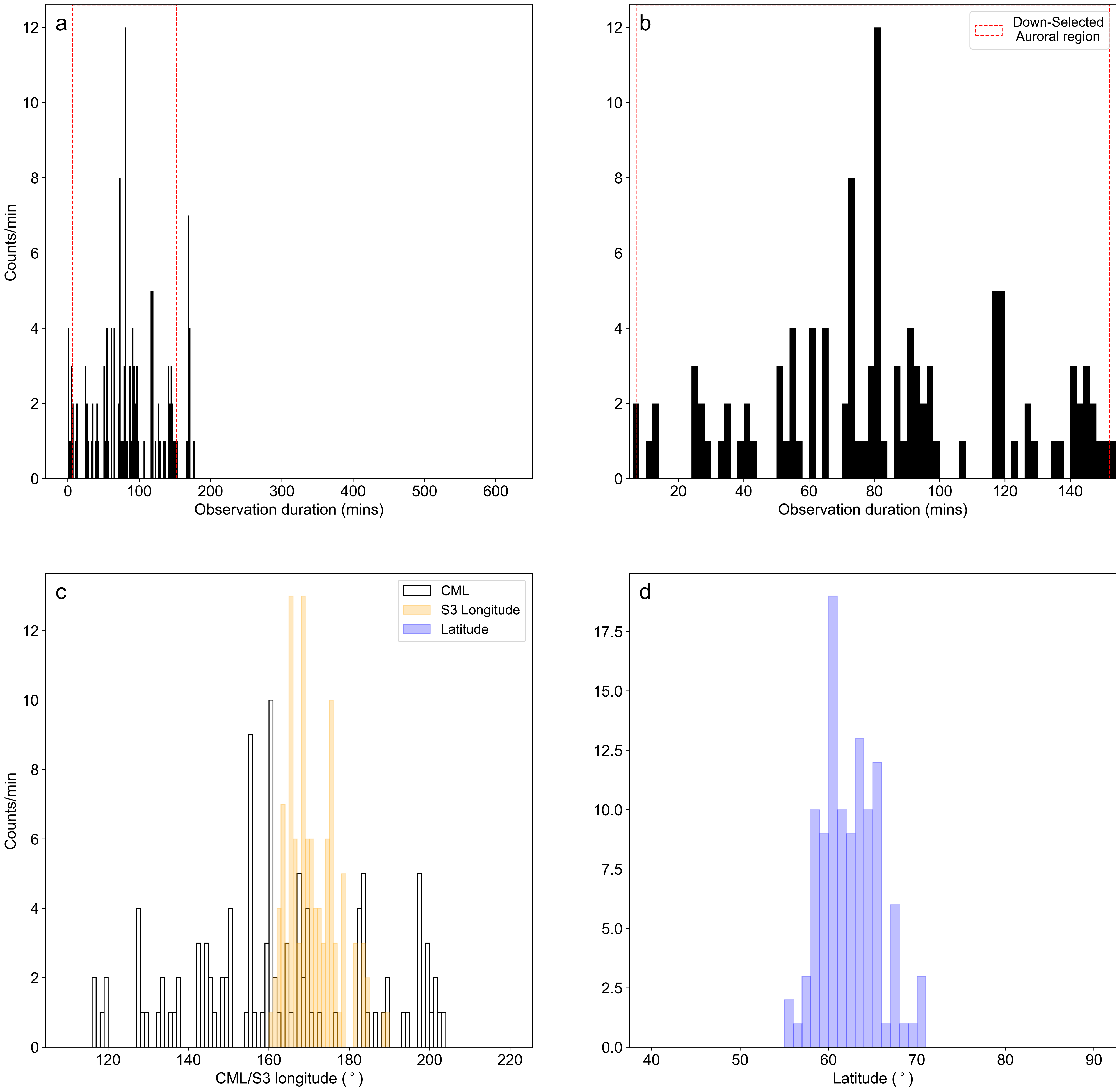

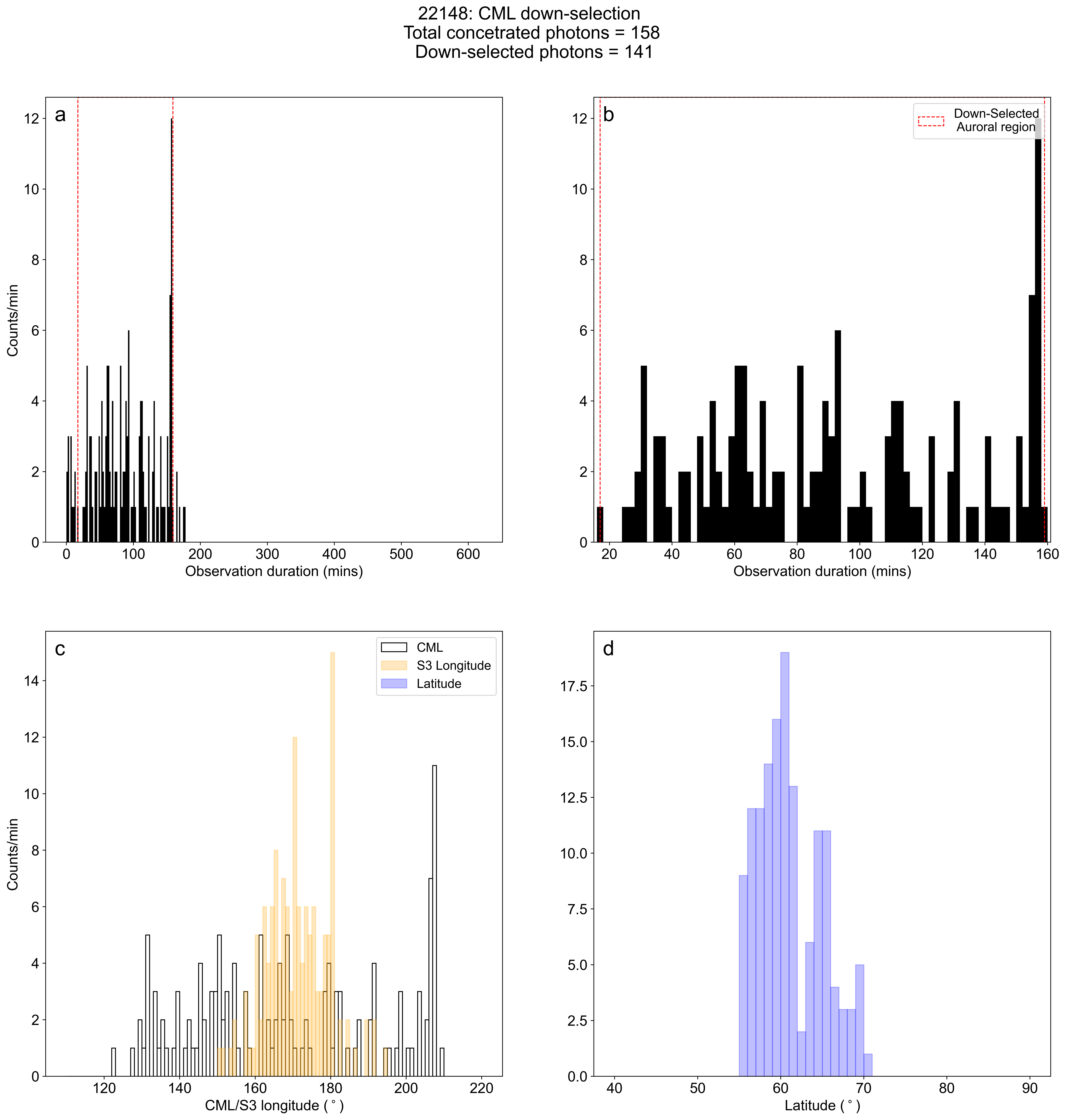
22148: CML down-selection
Total concetrated photons = 158
Down-selected photons = 141
a
Counts/min
Observation duration (mins)
b
Down-Selected
Auroral region
Observation duration (mins)
c
CML
S3 Longitude
Latitude
Counts/min
CML/S3 longitude (°)
d
Latitude (°)

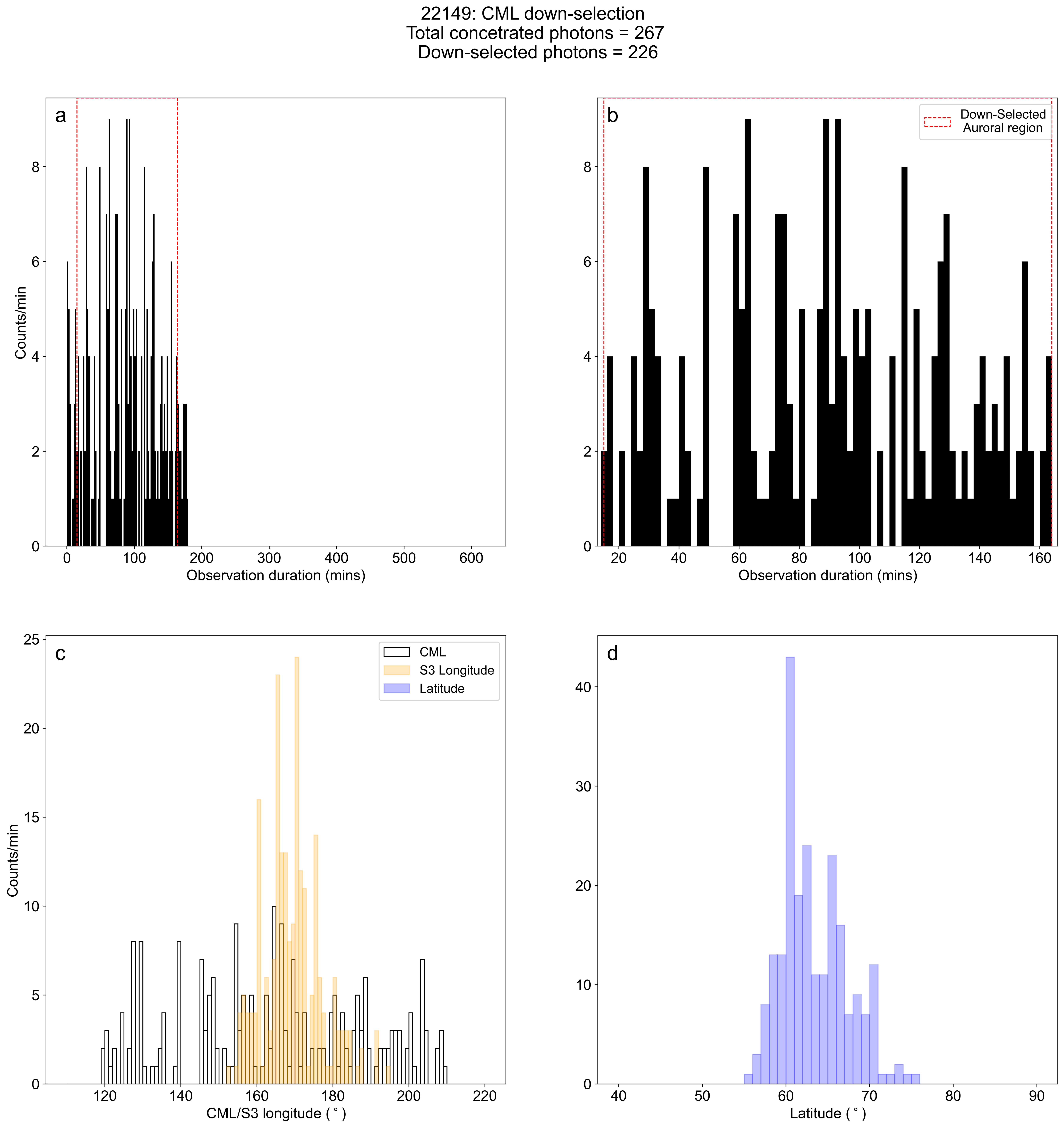
22149: CML down-selection
Total concetrated photons = 267
Down-selected photons = 226
a
b
Down-Selected
Auroral region
Counts/min
Observation duration (mins)
c
d
CML
S3 Longitude
Latitude
CML/S3 longitude ($^\circ$)
Latitude ($^\circ$)

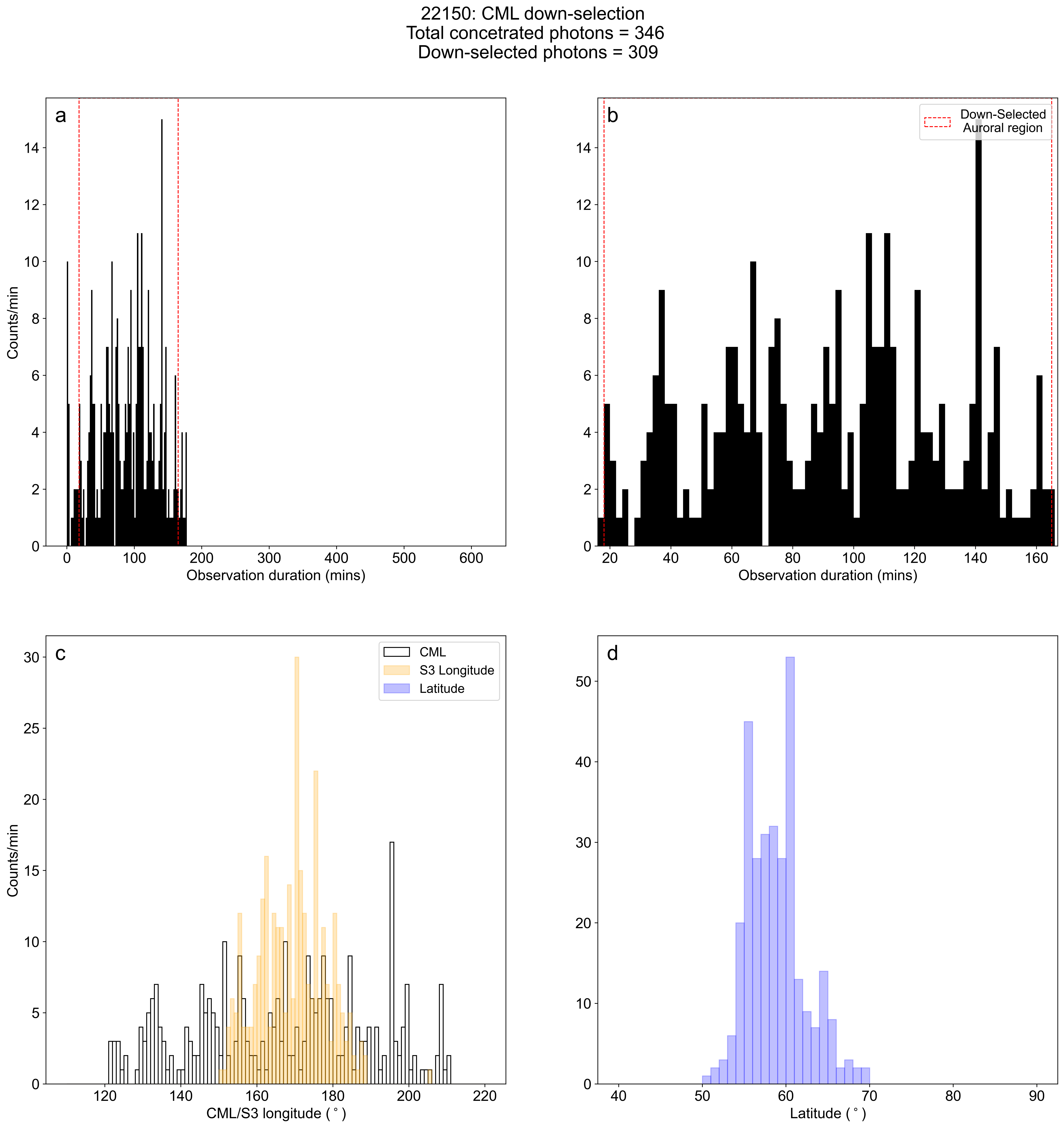
22150: CML down-selection
Total concetrated photons = 346
Down-selected photons = 309
a
b
c
d
Down-Selected
Auroral region
Counts/min
Observation duration (mins)
CML
S3 Longitude
Latitude
CML/S3 longitude ($^\circ$)
Latitude ($^\circ$)

22151: CML down-selection
Total concetrated photons = 262
Down-selected photons = 250